UNIVERSITY OF CALIFORNIA, SAN DIEGO

Computational modeling of Metal-Organic Frameworks

A thesis submitted in partial satisfaction of the
requirements for the degree of Master of Science

in

Chemistry

by

Jeffrey Chuen-Fai Sung

Committee in charge:

Professor Francesco Paesani, Chair
Professor Katja Lindenberg
Professor Seth M. Cohen

2012

The Thesis of Jeffrey Chuen-Fai Sung is approved and it is acceptable in quality and form for publication on microfilm and electronically:

_____

_____

_____

Chair

University of California, San Diego

2012

Dedication

For my family – my mom Sharon, dad Shiu Chung, and sister Lily

Epigraph

"Given for one instant an intelligence which could comprehend all the forces by which nature is animated and the respective situation of the beings who compose it – an intelligence sufficiently vast to submit these data to analysis – it would embrace in the same formula the movements of the greatest bodies of the universe and those of the lightest atom; for it, nothing would be uncertain and the future, as the past, would be present to its eyes."

Pierre-Simon, Marquis de Laplace

A Philosophical Essay on Probabilities

Translated by F. W. Truscott and F. L. Emory

Table of Contents

List of Abbreviations

AASBU: Automated Assembly of Secondary Building Units

AB: Azobenzene

ACF: Adiabatic Connection Formula

AFM: Atomic Force Microscopy

AMBER: Assisted Model Building with Energy Refinement

AZT-TP: Azidothymidine triphosphate

BDC: 1,4–benzenedicarboxylic acid

BEN: Benzene

BET: Brunauer, Emmett, and Teller

Bu: Busulfan

CC: Coupled Cluster

CDC: Colloidal Drug Carrier

CDV: Cidofovir

CHELP: CHarges from Electrostatic Potentials

CHELPG: CHarges from Electrostatic Potentials with Grid

CI: Configuration Interaction

CMD: Centroid Molecular Dynamics

CNT: Carbon nanotube

CP: Coordination Polymer

CSD: Cambridge Structural Database

CVD: Chemical Vapor Deposition

DABCO: 1,4–diazabicyclo[2.2.2]octane

DFT: Density Functional Theory

DMF: Dimethylformamide

DMOF+BEN: DMOF-1 + benzene

DUT: Dresden University of Technology

DZ: Double Zeta

ECM: Electron Correlation Method

ECP: Effective Core Potential

ESP: Electrostatic Potential

EXAFS: Extended X-ray Absorption Fine Structure

FF: Force Field

GAFF: General AMBER Force Field

GCMC/MD: Grand Canonical Monte Carlo/Molecular Dynamics

GGA: Generalized-Gradient Approximation

GTO: Gaussian Type Orbital

HF: Hartree-Fock

HKUST: Hong Kong University of Science and Technology

HOMO: Highest Occupied Molecular Orbital

Ibu: Ibuprofen

IPA: Isopropyl alcohol

IUPAC: International Union of Pure and Applied Chemists

LCAO: Linear Combination of Atomic Orbitals

LDA: Local Density Approximation

LP: Large Pore

LSDA: Local Spin Density Approximation

LUMO: Lowest Unoccupied Molecular Orbital

MD: Molecular Dynamics

MIL: Materials Institute Lavoisier

MO: Molecular Orbital

MOF: Metal–Organic Framework

MP: Møller–Plesset

MS–EVB: Multi state-empirical valence bond

NVE: Constant N, V, E

NVT: Constant N, V, T

NP: Narrow Pore

NPT: Constant N, P, T

NσT: Constant N, σ (stress), T

NTE: Negative Thermal Expansion

OCN: Organic Coordination Network

OPLS: Optimized Potentials for Liquid Simulations

PBS: Phosphate Buffered Saline

PCP: Porous Coordination Polymer

PCN: Porous Coordination Network

PDB: Protein Databank

PEM: Polymer Electrolyte Membrane

PES: Potential Energy Surface

PEMFC: Polymer Electrolyte Membrane Fuel Cell

PIMD: Path Integral Molecular Dynamics

PME: Particle Mesh Ewald

PP: Pseudopotential

PSM: Post-synthetic Modification

QZ: Quadruple Zeta

RCSD: Reticular Chemistry Structure Database

RDF: Radial Distribution Function

SBU: Secondary Building Unit

STO: Slater Type Orbital

TTM: Thole-Type Model

TZ: Triple Zeta

VDW: van der Waals

ZIF: Zeolitic-imidazole Framework

List of Figures

List of Tables

List of Files

Acknowledgements

I would like to acknowledge Professor Francesco Paesani for his support as the chair of my committee and my mentor and guide for these past two years. I certainly have my share of idiosyncrasies and I am grateful for Francesco for his willingness to put up with them. Thank you, Francesco, for your patience and the wisdom and advice that you passed on to me.

I would also like to acknowledge my fellow lab mates, past and present – Jordi Cirera, Volodymyr Babin, Wei Lin, Kyoyeon Park, Nico Sawaya, Greg Medders, Porter Howland, Kevin Bao, Jason Grosch, Duo Song, and Pilar Montellano, for the useful scientific discussions, advice, and good times. It has been a pleasure to have had you as friends and co-workers.

I would also like to acknowledge my friends outside of the lab – especially Kevin Wu and Alan Nam – but also everyone else, for their support, and their willingness to tolerate my endless complaints about convergence failures.

Most of all, I would like to acknowledge my family, for their endless support of me and the endeavors I have undertaken. Thank you.

Chapter 3, in full, is currently being prepared for submission for publication of the material. Cirera, J.; Sung, J. C.; Howland, P. B.; Paesani, F. The dissertation author was a contributor and co-author of this material.

ABSTRACT OF THE THESIS

Computational modeling of Metal-Organic Frameworks

by

Jeffrey Chuen-Fai Sung

Master of Science in Chemistry

University of California, San Diego, 2012

Professor Francesco Paesani, Chair

In this work, the metal-organic frameworks MIL-53(Cr), DMOF-2,3-NH_2Cl, DMOF-2,5-NH_2Cl, and HKUST-1 were modeled using molecular mechanics and electronic structure. The effect of electronic polarization on the adsorption of water in MIL-53(Cr) was studied using molecular dynamics simulations of water-loaded MIL-53 systems with both polarizable and non-polarizable force fields. Molecular dynamics simulations of the full systems and DFT calculations on representative framework clusters were utilized to study the difference in nitrogen adsorption between DMOF-2,3-NH_2Cl and DMOF-2,5-NH_2Cl. Finally, the control of proton conduction in HKUST-1 by complexation of molecules to the Cu open metal site was investigated using the MS-EVB methodology.

1. Introduction

1.1.Porous Materials

1.1.1. What are Porous Materials?

As the name suggests, porous materials are a class of materials that contain pores or other types of void spaces. The International Union of Pure and Applied Chemistry (IUPAC) classifies nanoporous materials according to internal pore width, where width is defined as the diameter of a cylindrical pore or the distance between opposite walls in a slit pore. Porous materials are classified in three groups as a function of their pore sizes: micropores, with internal widths of less than 2 nm, mesopores, with internal widths of 2 to 50 nm, and macropores, with internal width of 50 nm or greater.[1]

1.1.2. Gas Adsorption in Porous Materials

While a number of experimental techniques exist for determining the surface area of a porous material, such as mercury porosimetry, the most commonly-utilized method is gas adsorption measurements. Adsorption is a process in which atoms adhere to a surface, forming a gas/solid or liquid/solid interface. The solid material is termed the adsorbent while the gas molecules the adsorptive. The molecules in the adsorbed state are termed the adsorbate.[2]

The structure of the different pore types lead to different type of gas adsorption behavior. While macropores are usually large enough that pore walls are essentially individual flat surfaces, the walls of mesopores are closer together, leading to some pore-

guest molecule interaction effects as well as guest-guest effects, while the walls of micropores are so close that the dominant effect is in pore-guest interactions.[2]

There are two types of adsorption processes, physisorption and chemisorption. Chemisorption is the irreversible adsorption of guest molecules through the formation of bonds between guest molecule and host system. This typically only allows for a single layer of adsorption to occur. Physisorption, in contrast, is a more general process in which the adsorption of guest molecules occurs through weaker interactions such as van der Waals forces.[2]

The adsorption of gas molecules by porous materials is represented by isotherms of adsorption. In these isotherms, the amount of gas adsorbed is plotted versus the relative pressure. There are six types of isotherms (types I through VI[1]) which correspond to different types of adsorption behavior. In type I isotherms, the curve is concave to the pressure axis, and reaches a limiting value. Most physisorption processes have type I isotherms. Type II isotherms typically occur with a nonporous or macroporous adsorbent – the adsorption does not reach any limiting value. Type II isotherms have an inflection point, which corresponds to the point when the adsorbent is fully covered with a monolayer of adsorbate. Type III isotherms are similar to type II, but lack a point of inflection. Typically this occurs in systems where the adsorbate-adsorbate interactions dominate. Type IV isotherms begin concave to the relative pressure axis, before reaching a limiting value. However, a hysteresis is observed upon desorption. The hysteresis is usually associated with pore condensation, a process by which the guest molecules condense from the vapor phase, typically at different conditions than required for condensation in the bulk phase. The initial concave region

of the type IV isotherm corresponds typically to initial monolayer formation on the adsorbent during the early stages of the adsorption prior to the start of multilayer adsorption. This process is known as "wetting." Typically type IV isotherms are observed in mesoporous materials. Type V isotherms are similar to type IV, but are non-wetting; they lack the initial concave adsorption, though they also display hysteresis. This usually indicates weak guest-host interactions. Type VI isotherms represent stepwise multilayer adsorption, usually on uniform and non-porous surfaces. Each step corresponds to adsorption on a layer.[2] The different types of adsorption isotherms can be seen in Figure 1.1.

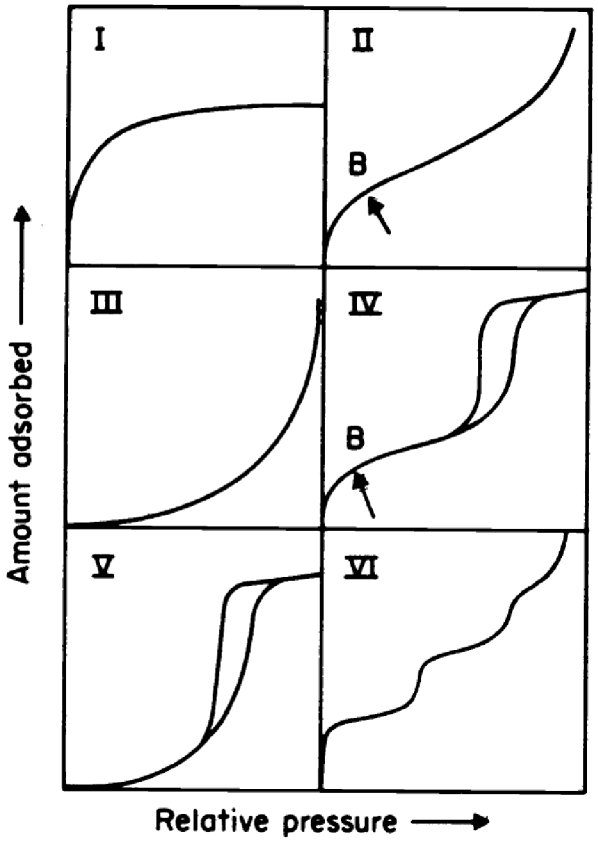

Figure 1.1 – Isotherms of adsorption. Taken from Ref. 1.

1.1.3. Langmuir and BET Isotherms

Typically, the surface area of a porous material is characterized through gas adsorption isotherms. Type 1 isotherms can be described by Langmuir isotherms, which were originally derived using a kinetic approach in 1916 by Langmuir.[3] From these isotherms, the Langmuir surface area can be computed. Unfortunately, the Langmuir equation does not adequately treat physical adsorption, because it only applies to single-layer adsorption; molecules are assumed to either be a part of the adsorbed layer or in the vapor state. Chemisorption, however, can be modeled correctly with a Langmuir isotherm, due to the requirement of active chemical sites.

A better description of physical adsorption would need to take into account multiple layers of adsorption. Such a model was derived by Brunauer, Emmett, and Teller in 1938.[4] This theory is commonly referred to as BET theory, after the names of the authors. In BET theory, the uppermost in an adsorbed layer of guest molecules is assumed to be in dynamic equilibrium with the vapor. This correctly accounts for multi-layer adsorption of guest molecules. Because of this, the BET surface area is a more accurate measure of the adsorption capacity of a porous material than the Langmuir surface area for physisorption.[2]

1.1.4. Types of Nanoporous Materials

Several types of porous materials have been studied and described in the literature in the past years. Amongst them, zeolites, carbon nanotubes, and metal-organic frameworks are subjects of great focus due to their inherent technological applications.[5-7]

Zeolites are microporous materials originally discovered in mineral form in the 18th century. Typically consisting of hydrated aluminosilicates of alkali and alkaline earth cations in a porous 3D structure, zeolites have found commercial use due to their ability to act as molecular sieves after dehydration. Zeolites are also able to selectively adsorb polar molecules with high selectivity due to their cationic nature. Due to their high natural abundance and the ease of synthesis of non-naturally-occurring variants, zeolites are used commercially in the removal of ammonium ions from wastewater, and have shown potential for use in the removal of Pb^{2+} ions from drinking water.[5] Furthermore, zeolites are used as molecular sieves in the purification of hydrocarbons and the preparation of catalysts for the refining of petroleum. The ability for zeolites to exchange internal cations with the surrounding environment has also been utilized in the cleanup of radioactive nuclear waste.[5]

Carbon nanotubes (CNTs) are a class of material consisting of graphitic carbon rolled up into nanometer-scale cylindrical shapes. They can be synthesized by a variety of methods, such as laser ablation in the presence of metal catalysts, passing a high current through graphite electrodes (known as arc methods), or chemical vapor deposition (CVD). Similar to their parent material graphite, CNTs have high tensile strength, due to their high Young's modulus. Furthermore, CNTs have the ability to conduct electricity efficiently. Significant research has also gone into developing methods of functionalizing CNTs with chemically interesting moieties. Work in the storage of H_2 gas in carbon nanotubes has also been carried out, though there is disagreement on the amount of a gas that can be successfully stored in the CNT. CNTs have also been found to be able to store larger gases, though the type of gas molecule that can be stored in a specific CNT is

limited by the diameter of that nanotube.[6] Due to their narrow dimensions, CNTs are able to exert confinement effects on water molecules inside the channel, leading to water transport with flow rates several orders of magnitude faster than would be expected through a channel from conventional nonslip hydrodynamic flow. Consequently CNTs also have potential water transport applications where the minimization costs is of utmost importance, such as in seawater desalination or polluted water filtration.[8]

While zeolites and CNTs are materials with many interesting properties and applications, this thesis focuses on the properties and applications of metal-organic frameworks. Metal-organic frameworks (MOFs) have not only similar properties as zeolites and CNTs, but also number of advantages. Unlike zeolites, MOFs generally have larger pore diameters, which make MOFs more applicable to separations and capture of larger molecules. Furthermore, some MOFs have an intrinsic flexibility, while zeolites are rigid structures. Unlike CNTs, MOFs have polar functional groups in their pores, allowing MOFs to more easily interact with molecules in the pores. These interesting properties and advantages that MOFs have over other porous materials merit consideration. The remainder of this chapter will introduce the background, properties, and applications of metal-organic frameworks.

1.2.Introduction to Metal-Organic Frameworks

1.2.1. History of Metal-Organic Frameworks

In 1897, Hofmann and Küspert synthesized a crystal with chemical formula $Ni(CN)_2(NH_3)_2 \bullet C_6H_6$ by slow layer diffusion of C_6H_6 into an NH_3 solution of $Ni(CN)_2$[9]. Though the structure of the Hofmann complex was initially proposed to be a Nickel

monomer coordinated with a η^6 benzene molecule, in 1954 Powell and co-workers determined the structure to be a tetragonal crystal with cell parameters $a = b = 7.242$ Å and $c = 8.277$ Å[10]. The crystal was found to consist of two dimensional arrays of Nickel atoms connected by CN linkers; in the third dimension, pillaring linkers of the NH_3 molecules held together the arrays. The benzene molecules were found inside the void space of the crystal lattice. The structure can be seen in Figure 1.2.

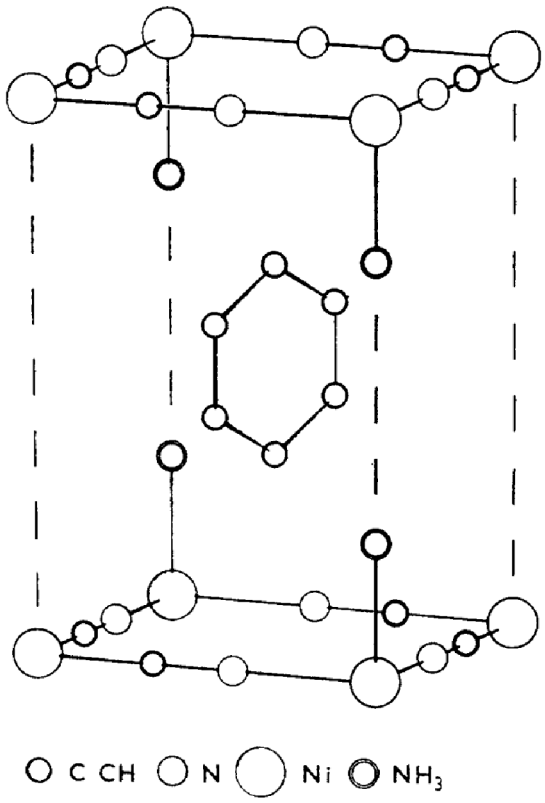

Figure 1.2 – Structure of the Hofmann complex. This figure is a modified figure from Ref. 10.

Subsequently, work began in the replacement of the cyanide linkers with other, large organic molecules, which led to the synthesis of the first organic coordination network (OCN) by Robson in 1989.[11] Consisting of tetrahedral $Cu^{I}C(C_6H_6CN)_4^{+}$ centers

linked together by rod-like 4,4',4",4-tetracyanotetraphenylmethane units, the framework contained large cavities with a volume of approximately 700 $Å^3$ filled with nitrobenzene and BF_4^- ions. The synthetic method developed by Robson established the feasibility of constructing porous frameworks through the use of rod-like linkers.

An important leap forward in the field occurred in the mid-1990s, when Yaghi and coworkers developed a number of general strategies for the synthesis of modular solids – frameworks whose properties such as void volume could be tuned by the use of linkers of different sizes and properties.[12] However, many of these modular solids synthesized were cationic in nature, and attempts to exchange guests within the pores led to framework collapse. Further work by Yaghi and co-workers led to the discovery that multidentate linkers such as carboxylates would allow for the formation of more rigid frameworks. The linkers were found to complex with metal ions to form clusters of the form M-O-C, which were termed secondary building units (SBUs)[13]. Due to the increased rigidity and neutral nature of SBUs compared to the charged tetrahedral centers of earlier materials, SBUs could be assembled to form frameworks more stable to solvent evacuation[13]. Though M-O-C clusters are the most commonly-utilized SBUs, the term more generally refers to the geometrical shapes of linking points of extension between different parts of the framework.[13-14] Continuing work led to the development of the method of reticular synthesis,[14] focusing on utilizing the correct materials and *in situ* conditions leading to the synthesis of building blocks that would self-assemble into viable frameworks.

1.2.2. Nomenclature

The terms porous coordination polymer (PCP), porous coordination network (PCN), and metal-organic framework (MOF) are often used in the literature interchangeably. Due to the high number of publications in the field, in 2009 IUPAC initiated a project to define nomenclature guidelines to distinguish between coordination polymers (CPs) and metal-organic frameworks (MOFs). While the project is still underway, a preliminary report[15] was released in 2012. In that report, the authors reviewed literature and IUPAC-recommended definitions, and proposed two tentative hierarchal schemes for defining and differentiating between coordination polymers, coordination networks, and metal-organic frameworks.

The authors found that the term "coordination polymer" as currently defined by IUPAC[16] includes straight-chain polymers of 1 dimension, but not higher-dimensional compounds. However, 2D and 3D coordination polymers and metal-organic frameworks are types of coordination compounds, defined as "any compound that contains a coordination entity,"[17] where a coordination entity is defined as "an ion or neutral molecule that is composed of a central atom, usually that of a metal, to which is attached a surrounding array of atoms or groups of atoms, each of which is called a ligand." [17] Ultimately, until the final recommendations from the task group are published, an exact distinction might be impossible amongst the various related compounds that make up PCP, PCN, and MOF materials. However, for the purposes of this document, the term "metal-organic framework" will be used to refer to the systems studied.

At this time, a systematic naming convention does not exist. Some MOFs are named after the university where they were synthesized. For example, the MIL family[18] is named after the Materials Institute Lavoisier, HKUST-1[19] is named after the Hong

Kong University of Science and Technology, and the DUT family[20] is named after the Dresden University of Technology. An alternative scheme is based on the crystallographic nets of the framework, modeled after the naming scheme used for zeolites; this is the naming scheme followed by the Reticular Chemistry Structure Database (RCSD).[21] Zeolitic-imidazole frameworks[22], MOFs synthesized with structures based on the structural nets of aluminosilicate zeolites, are named with the prefix ZIF.

1.2.3. Synthesis and Modification

An appealing aspect of MOFs is the ease of synthesis. MOFs are typically synthesized in solvothermal "one pot" syntheses. Unfortunately, the starting materials utilized in the synthesis are not necessarily conserved during the synthetic process; thus there exists a general lack of control over the products from the starting materials in MOF synthesis. [14] The successful syntheses of MOF-2[23] and MOF-5[24] by Yaghi and co-workers and subsequent work demonstrated the flexibility of usage of carboxylates as organic linkers to create SBUs which self-assemble into the regular 3D MOF structures.[25] An alternative approach focusing less on carboxylates has been that used by Ferey and co-workers utilizing a computational automated assembly of secondary building units (AASBU) method that explores the possible connections between metals and linkers from a prebuilt database of possible metals and linkers.[18] This method has led to the discovery of many of the frameworks in the MIL family.

Despite the advances that have been made in MOF synthesis, the nucleation and crystal growth of MOFs is still not very well understood. Recently, *in-situ* AFM experiments showed that the fundamental unit of growth of the framework HKUST-1

during synthesis was smaller than the metal cluster SBU as previously had been assumed.[26] This led to additional work utilizing EXAFS spectroscopy to study the synthesis of HKUST-1 and MIL-53;[27] it was observed that the synthesis of HKUST-1 appeared to be dominated by a more classical nucleation kinetic mechanism involving homogeneous nucleation and growth, while the synthesis of MIL-53 led to the creation of an intermediate amorphous phase similar in structure to that of MOF-235. This work has shown that different types of frameworks nucleate differently in solution, and more work must be done to fully uncover the connection between starting materials, SBUs, and the final synthesized MOF.

Besides the ease of synthesis, MOFs are also highly tunable in functionality due to the modifiable nature of the organic components. While it is possible to synthesize a functionalized MOF by starting with functionalized linkers, care must be taken to avoid cross-reactive processes.[28] One way to avoid this problem is the use of post-synthetic modifications (PSMs), in which the organic linkers are modified after the synthesis of the framework in mild conditions.[28] By using PSM, Cohen and co-workers successfully modified the flexibility of DMOF-1, by adding alkane chains of various lengths to the amine groups of DMOF-1-NH_2.[29]

1.3.Applications of Metal-Organic Frameworks

1.3.1. Carbon Capture and Separation

The separation and capture of CO_2 from anthropogenic sources is a topic of great concern and interest today. While zeolites and activated carbons have been used for gas separations industrially, the flexibility of design of MOFs makes them potentially

attractive candidates to replace the current materials, if MOFs can be made cost-effective. Consequently, there is significant research in the separation of CO_2 from various sources such as power plant flue gas emissions or "sour" natural gas.[30] Due to their tunable nature, MOFs have extremely high potential for being useful materials for carbon capture and separation. In a recent review, Bae and Snurr examined MOFs, looking particularly at four properties amenable to carbon capture: pore size, open metal sites, polar functional groups, and extraframework cations. [31]

MOFs pore sizes can be tuned to separate CO_2 from other gasses by molecular sieving, such as in CUK-1, which separates CH_4 from CO_2 through size exclusion.[32] Kinetic separations in which one gas diffuses more quickly than the other through the framework are also possible, as shown by MIL-96's slow adsorption of H_2 gas.[33] Bae and Snurr noted, however, that pore size does not necessarily correlate with gas separation. [31]

While the metal atoms in most MOFs are coordinated entirely with framework components, some MOFs, when synthesized, contain weakly-coordinated solvent molecules. HKUST-1, one of the most well-studied MOFs, consists of a dicuprate cluster complexed to four benzene-1,3,5-tricarboxylic acid (TMA) molecules in a paddlewheel configuration, with each Copper atom's fifth coordination site coordinated to water molecules during synthesis. Heating of HKUST-1 and other such MOFs leads to the removal of the complexed solvent molecules, leaving open metal sites on the activated framework.[34] Frameworks with open metal sites have been shown to have extremely high CO_2/CH_4 and CO_2/N_2 selectivities, with Mg-MOF-74 showing not only high selectivity but also large CO_2 uptake as well.[35]

The abilities to vary the framework ligands of a MOF during synthesis and to change functional groups of ligands postsynthetically mean that the properties of MOFs can be finely tuned using the known and extensive lore of organic chemistry. In particular, the ability to synthesize frameworks with highly polar functional groups is extremely useful for carbon capture due to the interaction between the CO_2 quadrupole moment and the functional groups. An example of this can be seen with MIL-53(Al), which increases in CO_2 selectivity by over an order of magnitude after being functionalized with amines.[31,36]

Extraframework cations can be introduced into MOFs through metallation processes or chemical reduction. Farha and co-workers showed that the selectivity of a MOF for CO_2 over CH_4 could be accomplished by chemical reduction,[37] while a computational study by Babarao, et. al. predicted that the stabilizing Na^+ ions for anionic ZIF *rho*-ZMOF should be highly selective for CO_2 over H_2, CH_4, and N_2.[38]

While these properties of MOFs give them great potential for usefulness in separations, some issues remain to be resolved before MOFs can be widely accepted as materials for industrial capture of CO_2. First, while significant work exists concerning the separation of two-component mixtures, a review by Sholl and co-workers in 2010 was completely unable to find any measurements that directly characterized the multicomponent adsorption equilibrium in the literature.[30] Second, and more importantly, is the potential problem of water-stability. While some exceptions such as MIL-53(Cr) exist, most MOFs are not water-stable; work by Allendorf and co-workers showed that water molecules could displace ligands whose binding energy were below that of water with the metal ion.[39] In order for MOFs to become contenders with current

technology in industrial applications, materials must be designed that are not only selective but also stable in the presence of water.

1.3.2. Drug Delivery

When a drug is administered, a significant number of barriers exist before its successful delivery to the target protein, including surviving the highly acidic environment of the stomach, preventing derivation by liver enzymes and avoiding excretion by the kidneys.[40]

Due to these difficulties, a current focus of research is development of a drug delivery platform that can circumvent these barriers. Some materials currently being investigated include colloidal drug carriers (CDCs), such as liposomes and micelles.[41] Unfortunately, living organisms have gradually over time evolved elaborate mechanisms dedicated to the recognition of foreign pathogens and their removal from the body which render CBCs suboptimal when utilized *in vivo*.[42]

Some important criteria that an efficient and useful drug delivery system must fulfill include the ability to efficiently store large volume of drug molecules, to have a mechanism of controlled drug release, to contain a stable matrix that does not degrade *in vivo*, and to be detectable by imaging techniques.[43] As a class of porous materials with unique properties and behaviors, MOFs possess many of the properties required for a usable drug delivery system. Experiments of ibuprofen (Ibu)-loaded MIL-100(Cr) and MIL-101(Cr) were shown to be able to not only store large quantities of Ibu, with MIL-100 absorbing up to 0.35 g Ibu/g dehydrated MOF and MIL-101 1.4 g Ibu/g dehydrated MOF. Furthermore, the Ibu was fully released from MIL-100 over a course of 3 days *in*

vitro, while in MIL-101 over a course of 6 days, showing that not only are MOFs viable materials for drug delivery, but that tuning the linkers and functional groups available can change the delivery rate.[44] While this study showed great promise, Chromium-containing compounds are known to be highly toxic[44], and the studies were done *in vitro*. Subsequent work by Horcajada, et. al. investigated a number of non-toxic Fe(III) water-stable MOFs – MIL-53, MIL-88A, MIL-88Bt, MIL-89, MIL-100, and MIL-101-NH_2. Their non-toxicity were demonstrated with *in vitro* mouse macrophage assays and *in vivo* toxicity experiments carried out in Wistar female rats.[43] MIL-88A and MIL-100 were both found to degrade within 7 days after incubation *in vitro* at 37 ° C,[43] also a useful property for a drug delivery platform to have. Due to the non-toxicity of the MOFs, their ability to store and deliver busulfan (Bu), an amphiphilic antitumor drug widely used in combination with high-dose chemotherapy regimes for leukemia, was studied and found to be able to deliver the water-unstable and hepatic toxic Bu intravenously at a rate of 100 and 20 mg/kg/day for MIL-88A and MIL-100, respectively, over a course of four days. These MOFs were also successful at the controlled release of the anti-HIV treatments AZT-TP and CDV, as well as acting as contrast agents *in vivo* in female Wistar rats through the use of MRI measurements.[43]

MOFs that deliver drugs via exchange processes have also been demonstrated, such as with Rosi's bio-MOF-1.[45] Synthesized using Zn-adeninate columns linked together by biphneyldicarboxylates, the negatively-charged bio-MOF-1 system has been shown to exchange loaded procainamide HCl, an antiarrythmia drug with low *in vivo* half-life normally requiring regular doses every 3-4 hours, over a period of 72 hours in a

0.1 M PBS buffer, while retaining 80% of the drug compound when placed in nanopure water.[45]

1.3.3. Proton Conduction

Polymer Electrolyte Membrane Fuel Cells (PEMFCs) are environmentally friendly and efficient power sources with a wide range of application. In PEMFCs that react H_2 and O_2, the H_2 dissociates at the anode creating protons, which are transported through the polymer electrolyte membrane (PEM) to the cathode, where they oxidize O_2 to form water. Unlike most currently-utilized energy sources, this type of fuel cell has nearly no emissions, and does not contribute to the usage of ozone-depleting petroleum-based fuels. The current generation of PEMs are based on the polymer Nafion®.[46] Nafion® polymers are synthesized by the copolymerization of a perfluorinated vinyl ether comonomer with tetrafluoroethylene; they were developed and are produced by the DuPont Company.[47] The performance of conventional PEMFCs perform well below 90 °C. However, at higher temperatures, the loss of water in the cell hinders the proton conductivity.[46] Furthermore, Nafion® membranes do not perform well with methanol as the fuel source, as the proton transport leads to methanol transport, which can cause chemical short-circuiting through the oxidation of the transported methanol at the cathode.[48] As a result, a current focus of research in PEMFCs is the development of alternative PEM materials, including those that conduct protons at high temperatures.

Unlike macromolecular electrolytes, MOFs have a long-range order, which makes them uniquely suited for study of conduction mechanisms and properties.[49] Protons have been observed to through the framework itself[50] or through proton-conducting carrier

molecules, such as water[51] or imidazole.[52] Two methods that have been utilized for improving proton conductivity in MOFs: the incorporation of channel-accessible framework linkers or the addition of extraframework molecules after synthesis.

The incorporation of channel-accessible framework linkers typically involves the use of carboxylic, sulfonic, or phosphonic acid species as channel-accessible functionalities.[53] A MOF that utilizes phosphonate linkers is PCMOF-3, with unit cell $Zn_3(L)(H_2O)_2 \cdot 2H_2O$, where L is the linker [1,3,5-benzenetriphosphonate]$^{6-}$. Structurally, PCMOF-3 is composed of columns of L linkers bridged by Zn^{2+} ions, a configuration which forms neutral layers. Water molecules also coordinate to the Zn atoms. The structure of the phosphonate and coordinated-water oxygen atoms cause the interlayer region to become highly hydrophilic, allowing free water molecules to become highly anchored. This regular distribution of water molecules forms a series of sites that enable Grotthuss proton conduction.[49] Indeed, PCMOF-3 was found to have a conductivity of 35 μS/cm in H_2 gas at 25°C at 98% relative humidity, with proton transfer activation energy of 0.17 eV. This value is in the range usually attributed to Grotthuss proton hopping (0.1-0.4 eV) and is one of the lowest observed, with 1 M HCl having an activation energy of 0.11 eV and Nafion® 0.22 eV.[49]

The addition of non-framework components to a MOF has been shown to be able to improve its proton conduction. In 2010, Long and co-workers[54] synthesized a framework with unit cell $Cu[Ni(pdt)_2]$, where pdt^{2-} is the ligand pyrazine-2,3-dithiolate, based on an earlier proton-conducting framework with unit cell $Cu[Cu(pdt)_2]$ with measured conductivity of 100 μS/cm at room temperature, synthesized in 2008 by the Kitagawa group.[55] While $Cu[Ni(ptd)_2]$ itself has a conductivity of 0.001 μS/cm, the

conductivity of the framework at 50 °C while under an I_2 vapor stream increased to approximately 100 μS/cm, due to partial oxidation of the framework. The oxidation was found to be reversible, with conductivity decreasing to of 50 μS/cm after 12 hours of exposure to air.[54] The Kitagawa group also utilized counterions into negatively-charged frameworks to enhance proton conductivity. By adding in adipic acid to a $[Zn_2(C_2O_4)_3]^{2-}$ anionic layered framework, the proton conductivity was found to be 8000 μS/cm at 25 °C under 98% relative humidity. With an activation energy for proton transfer of 0.63 eV, the mechanism appears to be Grotthuss-like.

1.3.4. Miscellaneous Applications of MOFs

Besides for use with gas separation and capture, drug delivery, and proton conduction, the unique properties of MOFs make them useful in a cornucopia of applications. Due to the regular inclusion of both metallic and organic components in a 3D framework, MOFs are uniquely suited for usage as catalysts and can fill a niche not currently filled by other porous materials. Though MOFs are largely nanoporous materials, unlike zeolites, MOF pores can be larger than found in zeolites, but still smaller than those of mesoporous materials that lack the ability to impose confinement effects, thus bridging the two size scales.[56-57] Indeed, work has shown that HKUST-1 can be utilized as a selective Lewis acid catalyst, and that triniuclear copper networks of similar topology have the most efficient catalytic activity reported to date for the mild peroxidation of alkanes.[40] Ferey and co-workers have shown that MIL-100(Fe) is an effective catalyst for Friedel-Crafts benzylation, better than the zeolites HBEA and HY. MOFs can also be used for base catalysis, with Yaghi's IRMOF-3 showing conversion

for the Knoevenagel reaction and activity for the Aza-Michael condensation.[40] Furthermore, the design of homochiral MOFs has shown promise for the use of enantioselective catalysis, though one remaining challenge lies in the synthesis of a framework that maintains permanent porosity.[40] In addition, the linkers of MOFs can be utilized as regular sites from which organometallic and nanoclustered metallic components may be fixed for use in catalytic processes.[40]

Another area in which MOFs have shown promise over other porous materials is in the usage as semiconductors. Zeolites are hampered by the wide bandgap of aluminosilicates, which causes them to act as electrical insulators. However, Silva and co-workers point out in a review that with the wide variety of possible linker and metal combinations available for MOFs, it is likely that MOFs exist that can be tuned to have the correct bandgap to act as a useful semiconductor. The existence of photoluminescent frameworks like MOF-5 seem to indicate this, and the bandgap can be correlated to the width of the emission band.[58]

MOFs have also shown promise as use in spin-crossover materials. Transition-metal complexes with d^4-d^7 electron configurations may possess a transition between low-spin and high-spin configurations which may be triggered by an external stimulus such as temperature, photochemical input, pressure change, or pressure change. This transition leads to a change in magnetic susceptibility, electronic absorption spectra, vibrational spectra, and bond lengths change. Of particular interest is that ability for the addition or removal of guest molecules to tune the spin-crossover behavior of a MOF, which could have possible applications in molecular sensors. Spin-crossover materials can also be potentially used in spintronic devices for high-density storage media.[59]

1.4.Properties of Metal-Organic Frameworks

1.4.1. Water Stability

The utilization of MOFs for carbon capture and other practical applications is not possible if MOFs are not stable under real-world humidity conditions.[30] The hydrothermal stability of MOFs runs a range from completely unstable to stable after immersion in water. In the lower range, MOF-69C was found to undergo complete structural collapse upon any exposure to moisture or heat.[60] The framework MOF-5 was also found to be extremely unstable, collapsing after exposure to 2% steam in N_2 at 40 °C. [60] The framework HKUST-1 has moderate stability.[60] HKUST-1 has been shown to stable in ambient conditions. In fact, the addition of water to HKUST-1 has been shown to enhance its CO_2 adsorption properties.[34] At relatively high stability are MOFs such as the well-studied framework MIL-53(Al), Mg-MOF-74, and the zeolitic framework ZIF-8.[60] Early MD simulations of MOF-5 by Greathouse and Allendorf in water seemed to indicate that the low hydrothermal stability of MOF-5 stems from the displacement of metal-ligand bonds by water molecules.[39] Indeed, the combined computational and experimental study by Low, Willis, and collaborators showed correlation between the relative hydrothermal stabilities of MOFs with the metal oxide cluster-bridging linker bond strength. [60] Furthermore, the relative stability of open-metal site stems from the ability for water to interact with the metal site, instead of displacing a ligand during the interaction.[60] For the well-studied framework MIL-53, water molecules interact preferentially with the hydroxide linkers between the metal sites, keeping the framework stable.[61] The stability of ZIF-8 appears to stem from the high strength of the Zn-

imidazole N bond, which is expected to be stronger than the Zn-carboxylate O bond found in the carboxylate-linked MOFs.[60] Ultimately, the water-metal interactions and their strength relative to the bridging ligand-metal interactions seems to be a good indicator to the hydrothermal stability of MOFs.

1.4.2. Breathing Behavior

Some MOFs have been observed to undergo a reversible major structural transition upon the application of an external stimulus such as a change in pressure, change in temperature, or adsorption of gas, leading to a dramatic change in cell vectors. While most inorganic solids and zeolites are able to undergo small reversible displacive phase transitions, the atomic displacement involved are typically small. In contrast, MOFs can undergo large phase transitions in porosity.[62] Not all MOFs breathe. DMOF-1 has been found to breathe after the adsorption of benzene and isopropyl alcohol (IPA).[63-64] Some of the most-studied breathing MOFs are the MIL-53 family. Consisting of corner-sharing $MO_4(OH)_2$ groups connected by 1,4-benzenedicarboxylate (BDC) ligands, where M can be the metals Ga^{3+}, V^{3+}, Cr^{3+}, Al^{3+}, or Fe^{3+}, the MIL-53 family has proved to have interesting properties, including water-stability and breathing in the presence of H_2O, H_2S, and CO_2.[61,65-67] Depending on gas adsorbed, the breathing behavior of a MOF varies. DMOF-1, prior to adsorption, exists in a large pore (LP) state. Upon the addition of 2 benzene molecules per unit cell, the DMOF-1 pore volume decreases into a narrow pore (NP) state. During adsorption of IPA, the adsorption of 3 IPA molecules leads to the LP to NP transition. However, further addition of 1 IPA molecule per unit cell leads to a reopening of the framework into a LP structure. [68] This

behavior is similar to that observed in MIL-53(Cr) upon the adsorption of CO_2.[61] Molecular dynamics simulations in this group have shown that while the DMOF-1 LP to NP transition with benzene is caused primarily through the benzene-BDC and benzene-DABCO interactions, the bistability observed upon the adsorption of IPA has a different mechanism. The initial transition into the NP state occurs due to the hydrogen bonds formed between the alcohol hydroxide with the BDC oxygen atoms due to the preferential alignment adopted by the IPA molecules when the filling reaches 3 IPA molecules per unit cell. However, the additional of 1 additional IPA molecule per unit cell allows for the formation of weak hydrogen bonds through the pore walls, breaking the preferential alignment of the IPA molecules in each pore, causing the return of the DMOF structure to the LP configuration.[68] While theoretical models[69-71] of breathing mechanisms have been developed, and simulations[68,72] carried out, a unifying predictive model for breathing behavior does not yet exist.

In a review in 2009, Ferey[62] listed a number of empirical structural rules that might allow for MOF breathing. First, the existence of a plane of symmetry with the carboxylates in symmetric position for the SBU might allow for breathing. This rule is violated by MOF-5 but not DMOF-1. Second, from the literature, Ferey discovered that the ratio of the number of carbons in the surrounding carboxylates to the number of metallic atoms in the cluster (C/M) should be at least 2 – DMOF-1 and MIL-88, which both can breathe, have C/M values of 2, while MOF-5 and the entire family of IRMOF frameworks have C/M of 1.5. Ferey conceded, however, that this rule still required validation. Third, breathing was found to also be somewhat dependent on the denticity of the carboxylate ligands. Ditopic carboxylate ligands allow for the O-O axes of different

carboxylates to be parallel, allowing for a uniform compression. In contrast, tri- or tetra-topic ligands do not lead to parallel carboxylates, suppressing breathing, as seen in MOF-103, which contains the tritopic 1,3,5-benzene trisbenzoate and MIL-102, which contains 1,4,5,8-tetracarboxylate; neither MOF-103 nor MIL-102 breathe. Fourth, the framework should not contain irregularly-shaped topological components. For example, MIL-101 cannot breathe because though it has ditopic ligands and a trimeric SBU, the pores are pentangonally-shaped, a configuration not easily compressed. All four of these conditions must be met simultaneously to allow for breathing. [62]

Breathing behavior has been found to be tunable by various techniques. Cohen and co-workers treated DMOF-1-NH_2, an amino derivative of DMOF-1, with linear alkyl anhydrides of molecular formula $O[CO(CH_2)_nCH_3]_2$, n = 0-5 under gentle heating, to generate a series of amide-functionalized DMOF-1 derivatives, designated DMOF-1-AM(n+1). Gas sorption measurements showed an absence of breathing behavior upon CO_2, N_2, or Ar adsorption in the parent DMOF-1-NH_2 structure. However, the DMOF-1-AM1 CO_2 adsorption isotherm displayed hysteretic behavior generally associated with breathing. DMOF-1-AM2 and DMOF1-AM3 showed breathing behavior for all 3 gasses, with large observed hysteresis for the CO_2 adsorption at 196 K. However, the remaining members of the AM family, DMOF-1-AM4, DMOF-1-AM5, and DMOF-1-AM6 did not display breathing behavior, instead having type I gas sorption isotherms for all 3 gasses. Interestingly, unlike many other documented cases of breathing, the DMOF-1-AM(n+1), n=0-2 frameworks are more stable in a narrow pore (NP) configuration, and then expand to a large pore (LP) configuration after gas adsorption, being stabilized in

the LP configuration by the adsorbate.[29] These results show how subtle modifications of the framework components can lead to the successful tuning of breathing behavior.

An alternate method for triggering breathing behavior in MOFs through the properties of adsorbed guest molecules has also been demonstrated. Kitagawa and co-workers[73] introduced *trans*-azobenzene (AB) molecules into DMOF-1 at 120 °C. Upon irradiation with UV light, the AB molecules underwent *cis-trans* isomerization, changing the DMOF-1 from a tetragonal unit cell structure to an orthorhombic structure with angle of 67°. The framework was also found to have increased in volume per unit cell after the AB isomerization from 1042.0 $Å^3$ to 1169.3 $Å^3$. Gas sorption experiments showed that while the *trans*-AB-filled DMOF-1 system did not adsorb N_2 gas at 77 K, the adsorption increased dramatically with *cis*-AB filled DMOF-1, reaching saturation after adsorption of 45 mL/g. Thus, it can be seen that it is also possible to trigger breathing behavior in MOFs by judiciously utilizing guest molecules with responsive interactions to external stimuli.

2. Theoretical Background

2.1.Introduction

Due to their unique properties and potential technological applications, MOFs have been extensively studied through the use of both electronic structure and molecular mechanics methods. Electronic structure methods can be utilized to calculate a wide range of molecular properties, such as optimized geometries, partial atomic charges, and energy profiles. However, these calculations are constrained by the system size. To circumvent this limitation, the results of electronic structure calculations are used to parameterize force fields to calculate molecular mechanics calculations in extended systems.

2.2.Quantum Chemistry Calculations

2.2.1. Prelude: Approximations and Assumptions

When utilizing quantum mechanics to study a system, the key equation involved is the Schrödinger equation:

$$\mathbf{H}\Psi = E\Psi \tag{2.1}$$

Typically, the Hamiltonian operator **H** is split into components:

$$\left(\mathbf{T}_n + \mathbf{T}_e + \mathbf{V}_{nn} + \mathbf{V}_{ee} + \mathbf{V}_{ne}\right)\Psi = E\Psi \tag{2.2}$$

where $\mathbf{T}_n$ and $\mathbf{T}_e$ are the kinetic energies of the nuclei and electrons, respectively, and $\mathbf{V}_{nn}$, $\mathbf{V}_{ee}$, and $\mathbf{V}_{ne}$ the potential energies due to interactions between nuclei with nuclei, electrons with other electrons, and nuclei and electrons, respectively. Typically, when

studying systems at or relatively near equilibrium, the Born-Oppenheimer Approximation is also assumed. In the Born-Oppenheimer approximation, the motions of electrons are assumed to be on a significantly faster timescale than those of the nucleus, due to the orders of magnitude difference in their masses. Hence, the nuclei can be viewed as "frozen" relative to the electrons. This allows us to separate the nuclear and electronic components of the Hamiltonian from Equation 2, and to focus on the electronic part:

$$\left(\mathbf{T}_e + \mathbf{V}_{ext} + \mathbf{V}_{ee} + \right)\psi = E\psi \tag{2.3}$$

where $\mathbf{T}_e$ is the kinetic energy of the electron, $\mathbf{V}_{ext}$ is an external potential, and $\mathbf{V}_{ee}$ the electron-electron repulsion. The equation to be solved is now simplified. The equation is nearly, but not quite analytically tractable: the electron-electron correlation must be approximated because it is a many-body interaction. Thus, several approaches, including Hartree-Fock (HF), post-Hartree Fock methods, and Density Functional Theory (DFT) have been devised to solve the Schrödinger equation, with different ways of approximating the electron-electron correlation term.[74-75]

2.2.2. The Hartree-Fock Method

To solve the Schrödinger equation, we construct a trial wavefunction and utilize the variational principle, since the minimum energy of a trial wavefunction will be greater than or equal to the energy of the exact solution. To follow the Pauli Exclusion Principle, the trial wavefunction must be antisymmetric with respect to the exchange of any two electrons. Thus, the wavefunction is built using a Slater determinant. A Slater determinant is built up from orthonormal orbitals (single-electron wave functions), and for a system with N electrons with N spin orbitals, is given by the expression

$$\Phi = \frac{1}{\sqrt{N!}} \begin{vmatrix} \phi_1(1) & \phi_2(1) & \cdots & \phi_N(1) \\ \phi_1(2) & \phi_2(2) & \cdots & \phi_N(2) \\ \vdots & \vdots & \ddots & \vdots \\ \phi_1(N) & \phi_2(N) & \cdots & \phi_N(N) \end{vmatrix} \tag{2.4}$$

where $\phi_i(j)$ corresponds to *i*th spin orbital of the *j*th electron, $i = 1,2,\ldots N$ and $j = 1,2,\ldots N$. We now take the additional approximation that the trial wavefunction consists of only a single Slater determinant.[74]

Using the variational principle, we are ultimately left with the HF equations

$$\mathbf{F}_i \phi_i = \sum_{j=1}^{N_{electron}} \lambda_{ij} \phi_j \tag{2.5}$$

Here $\mathbf{F}_i$ is the Fock operator given by $\mathbf{F}_i = \mathbf{h}_i + \sum_{j=1}^{N_{electron}} \left(\mathbf{J}_j - \mathbf{K}_j \right)$ where $\mathbf{h}_i$ contains the kinetic energy of the *i*th electron and the interaction of the *i*th electron with the N_{nuclei} nuclei, $\mathbf{J}_j$ is the Coulomb operator, corresponding to the classical repulsion between the electron and the remaining charge distribution, and $\mathbf{K}_j$ is the exchange operator, which has no classical analog. The set of HF equations forms a Hermitian matrix. However, if the matrix is diagonalized, which corresponds to using a set of canonical molecular orbitals ϕ'_i, we obtain

$$\mathbf{F}_i \phi'_i = \varepsilon_i \phi'_i \tag{2.6}$$

Because the Fock operator depends on the Coulomb and exchange operators, which themselves depend on knowing all of the occupied MOs, solving the HF equations requires knowledge of all of the occupied MOs. Since these are not initially known, an iterative method is required. First, an initial guess is generated of the MO coefficients.

The Fock matrix is then diagonalized utilizing these coefficients, and the diagonalized coefficients utilized to generate a new Fock matrix. This process is repeated until the convergence of the solution is achieved. The MOs thus obtained are the Hartree-Fock solutions. Usually molecular orbitals are expanded using atomic orbitals as basis functions. This is known as the Linear Combination of Atomic Orbitals (LCAO) method. The solving of the HF equations through a self-consistent field (SCF) method is the basis of the HF method.[74]

Though HF is a good starting point, the method does not fully treat electron correlation. Instead, the interaction between one electron and the others is treated in a mean field-type fashion – this arises from the treatment of the electron-electron repulsion by assuming the remaining electron distribution can be described solely by a set of molecular orbitals. Unfortunately, electron correlation typically is important in chemical processes. Consequently, HF has some weaknesses such as overestimation of activation barriers.[75]

2.2.3. Møller-Plesset Perturbation Theory

Several post-HF methods known as electron correlation methods (ECM) have been developed to calculate the energy arising from the electron correlation. Perturbation theory is an approximation method in which the Hamiltonian is broken apart into a reference Hamiltonian and a small correction term:

$$\mathbf{H} = \mathbf{H}_0 + \lambda \mathbf{H}' \tag{2.7}$$

The perturbative part of the Hamiltonian can be Taylor-expanded in terms of λ. In general, the first-order correction is given by

$$W_1 = \langle \Phi_0 | \mathbf{H}' | \Phi_0 \rangle \tag{2.8}$$

and the second-order correction by

$$W_2 = \sum_{i \neq 0} \frac{\langle \Phi_0 | \mathbf{H}' | \Phi_i \rangle \langle \Phi_i | \mathbf{H}' | \Phi_0 \rangle}{E_0 - E_i} \tag{2.9}$$

More specifically, in quantum chemistry, Møller-Plesset (MP) Perturbation Theory[76] is utilized frequently as an improvement to HF calculations. In MP perturbation theory, the sum over the Fock operators is taken to be the reference Hamiltonian. With MP theory, the highest order *n* to which the corrections are calculated is denoted by MP*n*. The first-order (MP1) correction to the reference Hamiltonian is exactly the difference between the reference energy and the HF energy. The MP2 energy-correction term is

$$E_{MP2} = \sum_{i<j} \sum_{a<b} \frac{\langle \phi_i \phi_j | \phi_a \phi_b \rangle - \langle \phi_i \phi_j | \phi_b \phi_a \rangle}{\varepsilon_i + \varepsilon_j - \varepsilon_a - \varepsilon_b} \tag{2.10}$$

MP2 can account for 80-90% of the correlation energy, and MP3 can account for 90-95%. The fourth-order correction MP4 can account for 95-98% of the energy. However, MP2 scales on the order of M_{basis}^5, MP3 on the order of M_{basis}^6, and MP4 on the order of M_{basis}^7. As HF also scales on the order of M_{basis}^4, MP2 is typically chosen as the level of perturbation to improve on the HF energy.[74]

While HF is a variational theory, MP theory is perturbative in nature. Consequently, unlike with HF, there is no guarantee that the energy calculated by MP theory is an upper bound to the exact energy – instead, the energy can be above or below in value. Furthermore, the perturbative nature of MP theory means that the less accurately the reference HF wavefunction describes the system, the larger each higher-order correction term will be, requiring the use of higher levels of perturbation, which

quickly becomes computationally expensive. Furthermore, MP2 is known to overshoot the correlation effect. However, despite these disadvantages, MP theory is size-extensive, unlike Configuration Interaction (CI) methods, and MP2 is scales significantly better than Coupled Cluster (CC).[74-75]

2.2.4. Basis Sets

In electronic structure calculations, the expansion of an MO into basis sets is necessary since the form of the MO itself is unknown. If the basis set is complete, the expansion is not an approximate and fully describes the MO. However, a complete basis requires an infinite number of functions, which is impossible. Consequently, the choice of basis set for quantum chemistry calculations is important, as a basis set that is large enough to have sufficient accuracy, but small enough to be usable in a reasonable amount of time, must be chosen.

The two types of basis functions typically used are Slater Type Orbitals (STO) and Gaussian Type Orbitals (GTO). STOs have the functional form

$$\chi_{\zeta,n,l,m}(r,\theta,\varphi) = NY_{l,m}(\theta,\varphi)r^{n-1}e^{-\zeta r} \tag{2.11}$$

where N is a constant of normalization and $Y_{l,m}(\theta,\varphi)$ a spherical harmonic function. GTOs have the functional form

$$\chi_{\zeta,n,l,m}(r,\theta,\varphi) = NY_{l,m}(\theta,\varphi)r^{2n-2-l}e^{-\zeta r^2} \tag{2.12}$$

The Gaussian-like nature of the GTO functions makes them unable to accurately describe electrons near the nucleus. They also fall off more rapidly than STOs. However, computationally, the integrals of GTOs are more easily calculated than STOs. Typically

basis sets consist of STO and GTO terms. Furthermore, all basis sets must have at least the number of functions necessary to contain all the electrons of the neutral atoms in the system. Thus, the minimum basis set necessary to describe hydrogen would require only a single 1s function. Basis sets that have two of each type of basis function are known as a double zeta (DZ) basis set. The name refers to the constant zeta in the exponential term in both the STO and GTO functions. Basis sets with even three of each type of basis function are triple zeta (TZ) basis sets; those with four are quadruple zeta (QZ). Basis sets with five or more types of basis functions are refered to as *n*Z, where $n = 5, 6, \ldots$[74]

A basis set constructed for a molecule contains basis functions that describe every electron, from inner-shell electrons to valence electrons. However, in many chemical processes, the inner-shell electrons do not significantly contribute. Thus, the use of inner-shell electrons in quantum chemistry calculations adds to computational cost without significantly improving accuracy. A process known as basis set contraction can be utilized to decrease the computational cost of using a basis set without significant loss in accuracy. In basis set contraction, the variational coefficients for the inner-shell basis functions are set as constants. This decreases the number of effective basis functions that must undergo the variational process, and thus decrease the computational cost.[74]

Basis sets can also be correlation consistent (cc). Originally introduced by Dunning and coworkers,[77] the correlation-consistent basis sets are specifically designed to recover the maximum correlation energy of valence electrons through the inclusion of similarly-energetic basis functions at the same stage. The correlation-consistent functions can also have diffuse functions added. These basis sets are denoted with an aug- prefix, which refers to the "augmentation" of the basis set by diffuse functions.[74-75]

Large atoms suffer from a number of issues in the calculations in their representation through basis sets. Large atoms have large inner cores, which require significant computational resources to simulate. Furthermore, extremely large atoms have electrons whose velocities are high enough that relativistic effects must be taken into effect. One method utilized to circumvent these issues involves the use of Effective Core Potentials (ECPs); another name for these potentials is pseudopotentials (PP). With ECPs, the core electrons are not treated explicitly. Instead, the nucleus and inner-shell electrons are treated as an effective core, while the valence electrons are still treated explicitly. This method deals with relativistic effects and decreases the computational cost of the calculations.[74]

2.2.5. Density Functional Theory

In 1964, Hohenberg and Kohn showed that the ground state energy of a chemical system is dependent solely on its electron density.[78] This led to the development of Density Functional Theory, a quantum chemistry method that eschews the use of wavefunctions in favor of the electron density. Initial efforts in DFT by Thomas, Fermi, and Dirac divided the energy functional into three terms: kinetic energy, nuclear-electron attraction, and electron-electron repulsion, and described the electron density as a free electron gas. However, the free electron gas approximation, while relatively valid in metallic systems, breaks down upon application to more typical chemical systems, because the approximation describes the kinetic energy badly, leading to strange predictions such as the instability of any molecule relative to its constituent atoms. In 1965, Kohn and Sham[79] suggested that the kinetic energy of the system could be split into

two parts: the HF kinetic energy, which could be calculated exactly, and a small correction term. That is, the Hamiltonian can be written in a form such as

$$\mathbf{H} = \mathbf{T} + \mathbf{V}_{ext}(\lambda) + \lambda \mathbf{V}_{ee} \tag{2.13}$$

where $0 < \lambda < 1$, and $\mathbf{V}_{ext}(\lambda)$ is constructed such that for all λ the total electron density is the same for the $\lambda = 1$ case. For this Hamiltonian, the $\lambda = 1$ case corresponds to the real system, and a system with $\lambda = 0$ corresponds to a different system with non interacting electrons that has the same electron density as the real system. Thus, the key is to build a system containing non interacting electrons but with the same electron density as the real system; for this system we can write the expression for the system energy as

$$E\left[\rho(\boldsymbol{r})\right] = T\left[\rho(\boldsymbol{r})\right] + V_{ne}\left[\rho(\boldsymbol{r})\right] + V_{ee}\left[\rho(\boldsymbol{r})\right] + \Delta T\left[\rho(\boldsymbol{r})\right] + \Delta V_{ee}\left[\rho(\boldsymbol{r})\right] \tag{2.14}$$

where the first term corresponds to the kinetic energy of the non interacting system, the second to the nuclei-electron interaction, the third to the classical electron-electron repulsion, and the last two being correction terms to the HF energy and classical repulsion. Typically, the correction terms are absorbed into the exchange correlation term E_{xc}:

$$E\left[\rho(\boldsymbol{r})\right] = T\left[\rho(\boldsymbol{r})\right] + V_{ne}\left[\rho(\boldsymbol{r})\right] + V_{ee}\left[\rho(\boldsymbol{r})\right] + E_{xc}\left[\rho(\boldsymbol{r})\right] \tag{2.15}$$

Compared to other quantum chemical methods, DFT has one distinct advantage: DFT is an exact method. Whereas HF, MP theory, and other computational methods are approximate, DFT has been defined in such a way that the exact energy is theoretically obtainable: each term in the expression for the energy functional can be calculated exactly from HF or classical methods, except for the exchange correlation. The one caveat is that while the exchange correlation functional must exist, the Kohn-Hohenberg

theorem does not give any indication to what form it should have. Consequently, while the method is exact, the solutions must be obtained approximately, since the form of the exchange correlation is not known. Furthermore, the determination of the form of the exchange functional is thus very important in the DFT procedure.[74-75]

Despite its advantages, such as its relatively low cost for high accuracy, DFT does have some disadvantages. First, DFT does not model dispersion forces accurately. Second, chemical bonds are often predicted to have greater stability than in reality. Third, the choice of density functional can significantly impact the calculated energies.[74] However, these issues do not significantly impact the accuracy of this work. The electronic structure calculations carried out for this project were utilized to parameterize bonded force fields. Consequently, the first issue is not a problem, since potential energy scans were being utilized to generate bonded interactions. Since classical bonded force fields do not model bond breaking, the second issue does not cause any problems as the bond-breaking process is not being modeled. Finally, the third (and to an extent, second) issue can be resolved by comparing the DFT results with high-accuracy wavefunction methods, and judiciously choosing functional that yield similar results to those from more expensive but more accurate methods. For this work, all DFT calculations were checked against MP2 calculations.

2.2.6. Density Functionals

The name "exchange correlation" belies somewhat the scope of the corrections in the exchange correlation term. The exchange correlation contains not only the correction due to electron correlation and exchange interactions, but also a correction to the self-

interaction energy and the kinetic energy. Furthermore, any other interactions that cannot be easily modeled such as magnetic field interactions are also absorbed by the exchange correlation term. Since the exact nature of the term is not known, significant work has gone into the development of functionals for application in different types of systems.

Typically, the exchange correlation energy term is split into an exchange part and a correlation part, and represented in terms of the energy density:

$$E_{xc}\left[\rho(\boldsymbol{r})\right] = \int \rho\varepsilon_x(\rho)\mathrm{d}\mathbf{r} + \int \rho\varepsilon_c(\rho)\mathrm{d}\mathbf{r} \tag{2.16}$$

where ε_x is the exchange energy per particle and ε_c the correlation energy per particle. A variety of approximations exist for determining the exchange and correlation energy functionals.

In the Local Density Approximation (LDA), the local electron density is assumed to be that of a uniform electron gas. For such a density, the exchange energy is given by

$$E_x^{\mathrm{LDA}}[\rho] = -C_x \int \rho\varepsilon_x \mathrm{d}\mathbf{r} = -C_x \int \rho^{4/3}\mathrm{d}\mathbf{r} \tag{2.17}$$

if the system is closed-shell. If the α and β spin densities are not equal, the LDA scheme can be extended to the Local Spin Density Approximation (LSDA); the exchange energy can then be described in terms of the total density and a spin polarization function:

$$\varepsilon_x^{\mathrm{LSDA}}[\rho] = -C_x \left[\frac{(1+\varsigma)^{4/3} + (1-\varsigma)^{4/3}}{2} \right] \rho^{1/3} \tag{2.18}$$

The LSDA correlation energy was analytically calculated at low- and high-density limits through quantum Monte Carlo methods. The VNW[80] and PW[81] functionals are two popular families of functionals fitted to reproduce the behavior at the density limits. The PW functional is

$$E_{c/a}^{\mathrm{PW}}[x] = -2a\rho\left(1+\alpha x^2\right)\ln\left(1+\frac{1}{2a\left(\beta_1 x+\beta_2 x^2+\beta_3 x^3+\beta_4 x^4\right)}\right) \qquad (2.19)$$

where a, α, β_1, β_2, β_3, and β_4 are fitting parameters. The LSDA approach tends to underestimate the exchange energy by up to 10% and overestimates electron correlation by up 100%. This can lead to calculated bond energy errors of nearly 20 kcal/mol. However, despite this, LSDA methods have been found to yield approximately the same accuracy as HF methods.[74-75]

As discussed earlier, the free electron gas model does not very accurately describe the electron density. Indeed, utilizing a non-uniform electron density should lead to an improvement in the energy functional. Methods that depend not only on the electron density but also on the first derivative of the density are known as Generalized-Gradient Approximation (GGA) methods. One of the GGA methods proposed was Becke's[82] exchange functional, known as B:

$$\varepsilon_x^{\mathrm{B}} = \varepsilon_x^{\mathrm{LDA}} - \beta\rho^{1/3}\left[\frac{x^2}{1+6\beta x\sinh^{-1}x}\right] \qquad (2.20)$$

where x is a dimensionless gradient parameter given by $x=\frac{|\nabla\rho|}{\rho^{4/3}}$ and β obtained by fitting experimental data to x. Though its exchange potential is incorrect, the B functional correctly models the energy density at asymptotic limits and describes the exchange energy more accurately by up to 2 orders of magnitude than the LSDA exchange functional.[74-75] A very popular correlation functional is that of Lee, Yang, and Parr[83], LYP, obtained by fitting four parameters to empirical Helium atom data:

$$\varepsilon_x^{\mathrm{LYP}} = \begin{cases} -4a\dfrac{\rho_\alpha\rho_\beta}{\rho^2\left(1+d\rho^{-1/3}\right)} \\ -ab\omega\left(\dfrac{\rho_\alpha\rho_\beta}{18}\begin{bmatrix} 144\left(2^{2/3}\right)C_F+\left(47-7\delta\right)\left|\nabla\rho\right|^2 \\ -\left(45-\delta\right)\left(\left|\nabla\rho_\sigma\right|^2+\left|\nabla\rho_\beta\right|^2\right) \\ +2\rho^{-1}\left(11-\delta\right)\left(\rho_\sigma\left|\nabla\rho_\sigma\right|^2+\rho_\beta\left|\nabla\rho_\beta\right|^2\right) \end{bmatrix} \right. \\ \left. +\dfrac{2}{3}\rho^2\left(\left|\nabla\rho_\sigma\right|^2+\left|\nabla\rho_\beta\right|^2-\left|\nabla\rho\right|^2\right)-\left(\rho_\alpha^2\left|\nabla\rho_\beta\right|^2+\rho_\beta^2\left|\nabla\rho_\alpha\right|^2\right)\right) \end{cases} \tag{2.21}$$

where $\omega = \dfrac{e^{-c\rho^{-1/3}}\rho_\alpha\rho_\beta}{\rho^{14/3}\left(1+d\rho^{-1/3}\right)}$, $\delta = c\rho^{-1/3}+\dfrac{d\rho^{-1/3}}{\left(1+d\rho^{-1/3}\right)}$, and *a, b, c,* and *d* are constants. It should be noted, however, that LYP is an unusual GGA exchange correlation functional. Most GGA correlation functionals start with the LDA energy and add a correction term. LYP, however, does not begin with the LDA energy, as can be seen in Equation 2.21.[75] The B exchange correlation and LYP correlation functional are used together to represent the exchange correlation. This is typically referred to as BLYP. Another GGA exchange correlation functional is the PBE functional of Perdew, Burke, and Ernzerhof.[84]

Logically, the next improvement over GGA functional is to have an additional dependence in addition to the electron density and derivative of the electron density. With meta-GGA functional, the exchange correlation is constructed with an additional dependence on either the second-order derivative (the Laplacian $\nabla^2\rho$) of the electron density or the orbital kinetic energy $\tau = \dfrac{1}{2}\sum_i^{\substack{\text{occupied}\\ \text{orrbitals}}}\left|\nabla\phi_i\right|^2$.[74] Some meta-GGA functionals include the BR exchange functional of Becke and Roussel[85] and Becke's B95[86] correlation functional.

Another approach at approximating the exchange correlation involves the connection of the Hamilton in Equation 2.13 with the definition of the exchange correlation energy. This connection, known as the Adiabatic Connection Formula (ACF), is obtained by integrating over the parameter λ. This methodology ultimately leads to the usage of combinations of different types of functional. For this reason, this type of approach leads to what are known as hybrid functionals.[74] One extremely popular hybrid method is the Becke 3 parameter functional used with the LYP functional – the B3LYP[87] functional, which has the form

$$E_{xc}^{\mathrm{B3LYP}} = (1-a)E_x^{\mathrm{LSDA}} + aE_x^{\mathrm{HF}} + b\Delta E_x^{\mathrm{B88}} + (1-c)E_c^{\mathrm{LSDA}} + cE_c^{\mathrm{LYP}} \tag{2.22}$$

Another popular hybrid functional, particularly for use with hybrid metal/organic systems is the M062X functional of Truhlar.[88] M06-2X utilizes the M05 exchange functional, which has the form

$$E_x^{\mathrm{M062X}} = \sum_{\sigma}\left[\int \mathrm{d}r F_{x\sigma}^{\mathrm{PBE}}\left(\sum_{i=0}^{m} a_i \frac{\tau_\sigma^{\mathrm{LSDA}} - \tau_\sigma}{\tau_\sigma^{\mathrm{LSDA}} + \tau_\sigma}\right)\right] \tag{2.23}$$

where τ_σ is the spin kinetic energy, $\tau_\sigma^{\mathrm{LSDA}} = \frac{3}{10}\left(6\pi^2\right)^{2/3}\rho_\sigma^{5/3}$, with ρ_σ being the spin density, and σ being the component along an arbitrary space-fixed axis of electron spin angular momentum. The correlation functional uses that of the earlier M06-L and M06-HF functionals.[88] The overall form of the exchange correlation for M062X is given by

$$E_{xc}^{\mathrm{M062X}} = \frac{X}{100}E_x^{\mathrm{HF}} + \left(1 - \frac{X}{100}\right)E_x^{\mathrm{DFT}} + E_c^{\mathrm{DFT}} \tag{2.24}$$

where $E_x^{\mathrm{HF}}, E_x^{\mathrm{DFT}}$, and E_c^{DFT} are the HF nonlocal exchange energy, the local DFT exchange energy (as defined previously), and the local DFT correlation energy (as

defined previously), respectively, and X sets the percentage of Hartree-Fock exchange utilized in the functional. For M062X, $X = 54$. The 2X in the name stems from the fact that the percentage of nonlocal exchange in M062X is twice that of the percentage in the M06 functional $(X = 27)$.[88] Truhlar and co-workers concluded that M062X is recommended for main-group thermochemistry, kinetics, and noncovalent interactions.[88]

2.2.7. Partial Charge Determination

While calculating the energy of a chemical system is important in its study, another property that is necessary for usage in atomistic force fields is the atomic partial charges. While partial charges do not correspond directly to a physical observable, they are used in force fields to describe polar interactions such as electrostatic potential or dipole or quadrupole moments. The partial charges are typically obtained through the use of one of three population analysis methods: wave function partitioning in terms of basis functions, fitting schemes, or the portioning of electron density into atomic domains. In this work, the method utilized to obtain partial charges was a fitting scheme, and as such, that will be focus of this section.[74]

In a force field, the non-bonded interactions between polar groups are dominated by the interaction of the partial charge distribution of one of the groups with the electrostatic potential (ESP) of the other. The ESP at a specific location is the sum of the nuclei and electronic contributions. While the part from the nuclei is easily calculated from the nuclear charges, the electronic part requires knowledge of the wavefunction. Thus, fitting methods typically fit a set of parameters that reproduces the calculated ESP.[74]

The method utilized in this work for calculating partial charges is the CHELPG method of Breneman and Wiberg.[89] Based on the earlier CHELP (Charges from Electrostatic Potentials) method[90], CHELPG works to correct the orientational dependence artifact that arises through the CHELP algorithm. In CHELPG, a cube of points spaced 0.3-0.8 Å apart containing the molecule, along with a 2.8 Å buffer, is generated. All points within the vdW radius of any atom are discarded. Afterwards, an initial guess is generated to carry out a for a Lagrange multiplier least-squares fit to the exact system charge.[90] CHELPG charges were preferred over other types of atomic partial charges such as Mulliken charges because the CHELPG charges were found more suitable for simulating MOFs in prior work[68] by this group.

2.3.Molecular Dynamics Simulations

2.3.1. Introduction

While quantum chemistry methods such as MP2 and DFT can very accurately determine the energies and partial charges of molecules in various configurations, scaling difficulties cause the application of such calculations to extended systems with 100 atoms or more impractical. Consequently, MOFs cannot be directly studied through electronic structure methods. However, their extended nature also means that except under specific conditions, classical effects should dominate. Thus, classical simulation methods such as Molecular Dynamics (MD) should yield a reasonable first-order approximation of the behavior of MOFs. MD methods that incorporate nuclear quantum effects such as Path Integral Molecular Dynamics (PIMD)[91-92] and Centroid Molecular Dynamics (CMD)[93] also exist, and can be applied to capture the subtleties in the behavior of MOFs. The

trajectories generated by MD simulations can be analyzed in a multitude of ways: the distributions of atoms can be studied by generating radial distribution functions (RDFs), and properties of the system such as negative thermal expansion or enthalpy of adsorption can be studied by obtaining quantities such as unit cell vector magnitude or configurational energy.

2.3.2. Force Fields

Classical MD simulations assume that Newtonian mechanics is the dominant contribution to the behavior of the system being simulated, and consequently ignore the quantum mechanical behavior of the nuclei. Thus, MD methods are primarily involved in determining the structural minima of the molecule's potential energy surface (PES). The mathematical description of the PES of a system is termed a force field (FF). To represent the classical force field energy, two-, three-, and four-body interaction energies are summed with nonbonded interaction energy terms and coupling cross-terms:

$$E_{\mathrm{FF}} = E_{\mathrm{str}} + E_{\mathrm{bend}} + E_{\mathrm{tors}} + E_{\mathrm{cross}} + E_{\mathrm{VDW}} + E_{\mathrm{el}} \tag{2.25}$$

where E_{str} is the energy of bond stretching between two atoms, E_{bend} is the energy of angle bending, E_{tors} is the torsional energy of the rotation around a bond, E_{cross} is the energy from coupling cross-terms for these three interactions, E_{VDW} the van der Waals energy, and E_{el} the electrostatic energy.[74] Many different classical force fields exist in the literature, each with its own form for each energy term.[94-99] There are three types of classical force fields. Class I force fields contain only harmonic terms, and ignore coupling cross-terms ($E_{\mathrm{cross}} = 0$). In contrast, class II force fields utilize anharmonic

terms and have nonzero cross-terms. Class III force fields contain not only anharmonicity but also other chemical properties such as electronegativity and hyperconjugation.[100] A popular class I force field is the AMBER force field, parameterized originally for simulating proteins, nucleic acids, and small organic molecules.[95] The MM3 force field is a widely-used class II force field for many types of systems.[94] AMBER- and MM3-like force fields were utilized in this work. Consequently, this section will focus solely on the functional form of those force fields.

In MD simulations, the atoms are treated essentially as balls, bonded to one another with springs as bonds. Consequently, a simple bond-stretch interaction approximation is the second-order Taylor expansion around the natural bond length r_0. This is known as a harmonic interaction, named after the harmonic oscillator, whose PES has a similar form:

$$E_{\text{str}} = \frac{1}{2}k\left(r - r_0\right)^2 \tag{2.26}$$

where k is the bond stretching constant and $r - r_0$ the displacement from the natural bond length. The AMBER force field bond-stretching is modeled harmonically. While the harmonic models reproduce the behavior of bond stretching extremely well near the natural bond length, they can break down quickly in some systems. One method of improving the accuracy of bond-stretching is to utilize higher-order terms of the Taylor Expansion. Unfortunately, the third-order term of the Taylor expansion is not usable, because it predicts that at large displacements, the bond energy goes to $-\infty$, which is unphysical. Consequently, the next-usable Taylor approximation must go up to the

fourth-order term. This quartic potential is utilized by the MM3 force field, and has the following form:

$$E_{\text{str}} = \frac{1}{2}k_1\left(r - r_0\right)^2 + \frac{1}{3}k_2\left(r - r_0\right)^3 + \frac{1}{4}k_3\left(r - r_0\right)^4 \tag{2.27}$$

While the quartic potential is an improvement over a harmonic potential, it also suffers from unphysical predictions at large displacements – the quartic (and harmonic) potential predicts the energy goes to ∞. However, the potential should ideally go to 0 at large displacements, not infinity. A potential that is physically correct asymptotically and handles anharmonicity reasonably is the Morse Potential, which has the form

$$E_{\text{str}} = E_0\left[\left(1 - e^{-k(r-r_0)}\right)^2 - 1\right] \tag{2.28}$$

where E_0 is the bond dissociation energy.[74-75,100]

Similarly to the bond energy, the in-plane angle bending is modeled using a Taylor expansion around a reference angle θ_0. The AMBER force field uses a harmonic angle term:

$$E_{\text{bend}} = \frac{1}{2}k_\theta\left(\theta - \theta_0\right)^2 \tag{2.29}$$

For additional accuracy, the MM3 force field utilizes a sextic potential:

$$E_{\text{bend}} = \frac{1}{2}k_1\left(\theta - \theta_0\right)^2\left[1 - k_2\left(\theta - \theta_0\right) + k_3\left(\theta - \theta_0\right)^2 - k_4\left(\theta - \theta_0\right)^3 + k_5\left(\theta - \theta_0\right)^4\right] \tag{2.30}$$

The out-of-plane bending angle of the central atom of a sp^2-hybrdizied atom is also similarly defined, with AMBER using a harmonic out-of-plane bending:

$$E_{\text{bend}} = \frac{1}{2}k_{oop}\chi^2 \tag{2.31}$$

where χ is the out-of-plane bending angle, and MM3 using a sextic potential:

$$E_{\text{bend}} = \frac{1}{2}k_1\chi^2\left[1 - k_2\chi + k_3\chi^2 - k_4\chi^3 + k_5\chi^4\right] \tag{2.32}$$

(the reference out-of-plane angle is assumed to be 0°).[74-75,100]

The torsion, or dihedral, energy is a 1,4-interaction that models the steric interactions caused by the rotation around a bond. To model the periodicity, the torsional energy is typically modeled as one or more terms of a Fourier series, with a popular expression being of the form

$$E_{\text{tors}} = V_1\left[1 + \cos(\omega)\right] + V_2\left[1 - \cos(2\omega)\right] + V_3\left[1 + \cos(3\omega)\right] \tag{2.33}$$

where ω is the torsional angle. For the AMBER and MM3 force fields used in this study, only the Fourier series term for $n = 2$ was used:

$$E_{\text{tors}} = V_2\left[1 - \cos(2\omega)\right] \tag{2.34}$$

Though it is also possible to treat out-of-plane sp^2-hybridized atoms using a type of torsion interaction called an improper dihedral instead of as an out-of-plane angle bend, was not done in the present work.[74-75,100]

The van der Waals energy is the energy of the nonbonded interaction caused by London dispersion interactions, which occur when the electron distribution of an atom creates an instantaneous dipole, which interacts with another atoms' instantaneous dipole, even if neither atom has a permanent dipole moment. The vdW potential tends to infinity in the repulsive region and to zero in the attractive region. AMBER utilizes the commonly-used Lennard-Jones potential, of the form

$$E_{\text{VDW}} = 4\varepsilon\left[\left(\frac{\sigma}{r}\right)^{12} - \left(\frac{\sigma}{r}\right)^{6}\right] \tag{2.35}$$

where ε corresponds to the potential's well depth and σ is given by the expression $\sigma = r_0 / (2)^{1/6}$, where r_0 is the internuclear distance corresponding to the minimum energy.[95] The Lennard-Jones potential was derived using a hard-sphere approximation. However, it is known that actually some electron cloud overlap is possible – meaning the repulsive r^{-12} term is too hard. With this in mind, the MM3 potential uses another commonly-used potential – the Buckingham potential:

$$E_{\mathrm{VDW}} = Ae^{r/\rho} - \frac{C}{r^6} \tag{2.36}$$

where A, ρ, and C are constants that can be described in terms of ε and σ.[101] The exponential leads to a softer repulsive term, though at the cost of having a minimum distance below which the potential inverts and tends to $-\infty$. Some MD codes add a switching function to switch from Buckingham to Lennard Jones r^{-12} term near the inversion distance.

Typically, force fields only contain the homonuclear vdW ε and σ parameters. Mixing rules must be used to generate the heteronuclear ε and σ parameters. A set of commonly-used mixing rules are the Lorentz-Berthelot mixing rules.[100] For to atoms A and B, the Lorentz-Berthelot mixed vdW parameters are obtained from the arithmetic and geometric means for σ and ε, respectively:

$$\sigma_{\mathrm{AB}} = \frac{\sigma_{\mathrm{A}} + \sigma_{\mathrm{B}}}{2} \tag{2.37}$$

$$\varepsilon_{\mathrm{AB}} = \sqrt{\varepsilon_{\mathrm{A}} \varepsilon_{\mathrm{B}}} \tag{2.38}$$

The Lorentz-Berthelot mixing rules were utilized in this work to generate the mixed vdW parameters.

The electrostatic energy in a force field is the non-bonded energy that stems from the charge distribution in the system. Many force fields, including AMBER, utilize only partial charges assigned to each atom for the electrostatic energy. The energy in this case for a pair of atoms is easily obtained from the Coulomb potential:

$$E_{\text{el}} = \frac{1}{\varepsilon}\frac{q_1 q_2}{r_{12}^2} \tag{2.39}$$

where ε is the relative dielectric constant, q_1 and q_2 are the atomic charges, and r_{12} is the distance. The MM3 force field represents the electrostatic energy in terms of the more physically meaningful bond dipoles instead of partial atomic charges, and the energy of a pair of atoms can be obtained from

$$E_{\text{el}} = \frac{1}{\varepsilon}\frac{\mu_1 \mu_2}{r_{12}^3}\left(\cos\chi - 3\cos\alpha_1 \cos\alpha_2\right) \tag{2.40}$$

where ε is the relative dielectric constant, μ_1 and μ_2 are the bond dipoles, r_{12} is the distance, χ the angle between the dipole moment vectors $\boldsymbol{\mu_1}$ and $\boldsymbol{\mu_2}$, and α_1 and α_2 the complements of the angles between the $\boldsymbol{\mu_1}$ and $\mathbf{r}_{12}$ and $\boldsymbol{\mu_2}$ and $\mathbf{r}_{12}$ respectively.[74-75,100]

The terms above completely describe any class I force field such as AMBER. However, bonded interactions – bond stretching, angle bending, and torsion interactions – involving the same atoms are coupled to one another. This is because changes from equilibrium in one interaction lead to changes in energy of the other bonded interactions. Class II force fields such as MM3 take into account these interactions to maximize the computational accuracy. In this work, the cross-term energy accounts for two coupled interactions for two bonds that share a common atom: the bond stretchings that occur when the angle between the two bonds changes, known as the stretch-bend interaction,

and the bond stretching that occurs on one bond when the length of the other bond changes, known as the stretch-stretch interaction. While the stretch-bend interaction is implemented in MM3, the stretch-stretch interaction is not. However, these interactions are utilized in the present work, with the cross-term having the form

$$E_{\text{cross}} = A(r_{ab} - r_{ab}^{\circ})(r_{bc} - r_{bc}^{\circ}) + (\theta - \theta_0)[B(r_{ab} - r_{ab}^{\circ}) + C(r_{bc} - r_{bc}^{\circ})] \qquad (2.41)$$

where r_{ab}° and r_{bc}° are the reference bond lengths and θ_0 the reference angle.[74-75,100]

These are the basic interactions included in class I and II type force fields such as the AMBER and MM3 force fields. However, while these force field terms are a good approximation of the system on average, they do not accurately model polarization effects, which naturally occur when any atom approaches any other atom. Treating polarization effects correctly becomes important in confined environments, since that is when polarization has the largest effect on the local electron density. Consequently, a number of polarizable force field models have been developed for simulations of such systems. One such model is the Thole-Type Model (TTM).[102] In this model, each atom is considered to be polarizable, with the induced dipole moment given by

$$\boldsymbol{\mu_p} = \alpha_p \left(\boldsymbol{E}_p - \sum_{p \neq q} \boldsymbol{T}_{pq} \boldsymbol{\mu}_p \right) \qquad (2.42)$$

where $\boldsymbol{E}_p$ is the applied electric field on the atom, α_p is the atomic polarizability of the atom, and $\boldsymbol{T}_{pq}$ is the dipole field tensor. The polarization of the atoms are thus modeled through the change of the dipole moment that occurs when the environment changes. The advantage the Thole-type model has over other models such as the Applequist model[103] is that the charges that lead to the polarizability are "smeared out" as opposed to

being represented as point charges. This prevents the prediction of overly large anisotropies as seen when using the Applequist model.[102]

As can be seen from the terms that form the force field, a significant number of parameters is required per interaction to represent the PES. Thus, particularly for large extended systems, it would be prohibitively expensive to model each atom individually. As a result, in force fields, chemically equivalent atoms are typically assigned the same properties, such as charge and force field parameters for interactions with other types of chemically equivalent atoms. These types of chemically equivalent atoms are called atom types. Different force fields have different numbers of atom types, depending on the types of system for which they are parameterized.

2.3.3. Molecular Dynamics

Fundamentally, MD simulations involve the integration of Newton's second law for every atom in a chemical system. However, since this problem is analytically intractable for any system that has more than 2 particles (and a significant amount of interesting chemistry occurs in systems of larger size), the equation of motion is typically integrated using a finite difference method. In a finite difference method, instead of integrating over time continuously, the time is split into discrete timesteps. The force on each particle is calculated at a timestep, and used to determine their positions at the next timestep; this process is then repeated until convergence is reached. One common finite difference method utilized by MD codes is the velocity Verlet method.[100,104] In the velocity Verlet method, the positions and velocities at the next timestep are given by

$$\mathbf{r}(t+\delta t)=\mathbf{r}(t)+\delta t\mathbf{v}(t)+\frac{1}{2}\delta t^2\mathbf{a}(t) \tag{2.43}$$

$$\mathbf{v}(t+\delta t)=\mathbf{v}(t)+\frac{1}{2}\delta t\left[\mathbf{a}(t)+\mathbf{a}(t+\delta t)\right] \tag{2.44}$$

Since the velocity depends on the future acceleration, an intermediate step after the calculation of the future position must be carried out. In this intermediate step, a linear approximation is made

$$\mathbf{v}\left(t+\frac{1}{2}\delta t\right)=\mathbf{v}(t)+\frac{1}{2}\delta t\mathbf{a}(t) \tag{2.45}$$

From this intermediate half-time step position, the forces are calculated, leading to the acceleration at the next half-timestep, which corresponds to the $\mathbf{a}(t+\delta t)$.[100]

In a MD simulation, the system is first initialized by assigning velocities to the molecules from either a Maxwell-Boltzmann or Gaussian distribution. These velocities are then modified to maintain the distribution while zeroing the total momentum. Afterwards, the forces are calculated for each atom, and then the Verlet algorithm utilized to propagate the trajectories of the atoms, for a large number of timesteps, until the system has reached equilibrium. This algorithm carries out MD simulations in the microcanonical ensemble, also known as the NVE ensemble, for having a constant number of atoms (N), constant volume (V), and constant energy (E).[100]

However, it is often desirable to carry out the simulations in other ensembles besides NVE. A number of thermostats exist that maintain constant the temperature of the system, allowing simulations in the NVT ensemble (constant N, V, and T). Using the Berendsen thermostat[105], the system is coupled to an external heat bath with the desired temperature. Since the system temperature is the average kinetic energy

$$\langle K \rangle = \frac{3}{2} N k_b T \tag{2.46}$$

each atom's velocity is then rescaled, such that the rate of change of temperature in the system fulfills the following criterion:

$$\frac{dT}{dt} = \frac{1}{\tau}\left(T_{bath} - T\right) \tag{2.47}$$

where τ is a coupling parameter. While the Berendsen thermostat allows the system temperature to fluctuate slightly around the desired value, it does not generate a rigorous canonical distribution, since it is based on velocity scaling. A thermostat that does generate a canonical distribution is the Nosé-Hoover thermostat.[106] This thermostat treats the heat bath as an additional degree of freedom, s, with a fictitious mass Q. The heat bath has a potential energy of

$$U = \left(f + 1\right) k_b T \ln s \tag{2.48}$$

where f is the number of degrees of freedom of the system, and a kinetic energy of

$$T = \frac{1}{2} Q \left(\frac{\mathrm{ds}}{\mathrm{dt}}\right)^2 \tag{2.49}$$

The fictitious mass Q determines the strength of the coupling between the thermostat and the real system.[100]

In the NPT ensemble, the system energy and volume vary, while the pressure and temperature are held constant. This enables the studying of phase transitions. The pressure is held constant using a barostat. The Berendsen and Nosé-Hoover barostats function analogously to their corresponding thermostats.[100] In the NPT ensemble, there is only one degree of freedom that describes the system volume. Consequently, the variation in system volume is isotropic. However, this means that the NPT ensemble is

inadequate to model processes such as MOF breathing. In addition to maintaining a constant pressure, the constant stress ensemble (NσT) allows the stress tensor to vary anisotropically, using the same types of feedback mechanisms as those employed by thermostats and barostats to keep the stress near a given value.[107]

It is also possible to run MD simulations using stochastic dynamics – Langevin dynamics can be utilized to maintain a NVT, NPT, or NσT ensemble.[100] With Langevin dynamics, collisions between particles are dissipative, creating a friction force proportional to the particle's velocity:

$$\boldsymbol{f} = -m\gamma\mathbf{v} \tag{2.50}$$

where m is the particle mass and γ the velocity relaxation time. Furthermore, a random force due to molecular fluctuations **R** also acts upon each particle. The Langevin equation of motion for particle i in the system is given by

$$m_i \frac{\mathrm{d}^2 x_i}{\mathrm{d}t^2} = \mathbf{F}_i - m_i \gamma_i \frac{\mathrm{d}x_i}{\mathrm{d}t} + \mathbf{R}_i \tag{2.51}$$

where $\mathbf{F}_i$ is the force from the interactions with other particles. Langevin dynamics leads to the generation of canonical distributions, and so can be utilized in place of Berendsen or Nosé-Hoover thermostats and barostats.[100]

2.3.4. Water Models

Water models are force fields specifically designed to reproduce the dynamical and/or structural properties of bulk water. Many different water models exist in the literature, each parameterized to reproduce different properties of water under different conditions, with different levels of accuracy. As with all types of force fields, many are

nonpolarizable, but some polarizable water models exist as well. Some water models utilize rigid molecules of water, while others are flexible. Two of the more commonly-utilized families of water models include TIP4P[108] and SPC[109] families.

The TIP4P family of water models is based on a planar, rigid model of water with four sites. Three of the sites correspond to the two hydrogen and one oxygen atoms; the fourth site is located at the center of mass of the water molecule. In the TIP4P water model, the oxygen atom has no charge; this charge has been moved to the center of mass. Furthermore, the hydrogen atoms and center of mass site have no vdW parameters. One of the currently popularly-used water models from the TIP4P family is TIP4P/2005.[110] Parameterized to reproduce at normal pressure the temperature of minimum density of water, the TIP4P model more accurately predicts many properties of water such as expansivity, compressibility, melting properties, and phase diagrams than earlier TIP4P family water models. However, when compared to the original TIP4P model, which was parameterized to reproduce the vaporization enthalpy of water, it can be seen that TIP4P/2005 predicts a somewhat large vaporization enthalpy and somewhat low melting point.[110] The TIP4P/2005 water model parameters are listed in Table 2.1.

The SPC (Single Point Charge) family of water models is based on a planar, three-site rigid model of water. Each site corresponds to one of the atoms in the water molecule. The hydrogen and oxygen atoms each have charge, unlike in TIP4P-type models, though as with TIP4P, the hydrogen atoms lack vdW parameters. A flexible variant of the SPC water model is the SPC/Fw model of Voth,[111] which adds harmonic bond and angle potentials to the water model. The SPC/Fw model was developed to improve the SPC calculation of the self-diffusion constant and the static dielectric

constant, which are important properties during proton conduction. The aSPC/Fw[112] (anharmonic SPC/Fw) model corrects the bond stretching by introducing cubic and quartic terms. Compared to the harmonic SPC/Fw, the anharmonic model predicts a proton diffusion coefficient nearly 40% higher, which leads to significantly better agreement with experimental data. The aSPC/Fw water model parameters can be seen in Table 2.2.

Table 2.1 – TIP4P/2005 Water Model
The center of mass site M is located on the plane of the water molecule. Its placement is such that O-M bisects the H-O-H bond angle.

Parameter	Value
O-H bond distance	0.9572 Å
H-O-H bond angle	104.52°
O σ	3.1589 Å
O ε	0.77547 kcal/mol
O charge	0.0000 e
H charge	0.5564 e
M charge	-1.1128 e
O-M distance	0.1546 Å

Table 2.1 – aSPC/Fw Water Model

Parameter	Value
O-H bond distance	0.995 Å
H-O-H bond angle	116.09°
O-H α	2.287 $Å^{-1}$
H-O-H angle bending constant	75.9 kcal/mol rad^{-2}
H-O-H reference bond angle	112.5°
O charge	-0.8350 e
H charge	0.4175 e
O σ	3.165492 Å
O ε	0.1554253 kcal/mol

2.3.5. Radial Distribution Functions

A tool for analyzing the structure of a system is the radial distribution function (RDF), *g(r)*. RDFs are computed between a chosen atom and all other atoms in the system. To compute an RDF, an infinitesimal shell of thickness dr a distance *r* from the

chosen atom is taken. The RDF is the density of molecules in that shell relative to the ideal gas density; $g(r)$ is also known as the pair distribution function. RDFs are particularly useful because X-ray diffraction spectra can be used to generate an experimental distribution function, which can then be compared with the simulated RDF, thus providing experimental data that can be compared with the molecular dynamics results, allowing for the verification of the current force field used in the simulation.[100]

2.3.6. Correlation Functions

Correlation functions are a quantitative measure whether or not various properties of a system correlate. Normalized correlation functions have the form

$$c_{xy} = \frac{\langle x_i y_i \rangle}{\sqrt{\langle x_i^2 \rangle \langle y_i^2 \rangle}} \tag{2.52}$$

where x_i and y_i are the two properties whose correlation are being examined. Typically, if x and y correspond to the same quantity, this function is referred to as the autocorrelation function, whereas if x and y are different quantities, this is referred to as the cross-correlation function. A normalized correlation function will have a value between 0 (indicating no correlation) and 1 (indicating a high degree of correlation).

Because MD simulations are time-dependent, correlations can be analyzed at different times throughout the MD trajectory. Consequently, the evolution of the correlation through time can be analyzed using time correlation functions. A normalized time correlation function has the form

$$c_{xy}(t) = \frac{\langle x_i(t) y_i(0) \rangle}{\langle x_i(0) y_i(0) \rangle} \tag{2.53}$$

and is a measure of how long a system retains a correlation. Generally, autocorrelation functions typically begin with an initial value of 1, and drop off to 0 over time. The time it takes to lose correlation is known as the correlation or relaxation time. The relaxation time is physically important because it can be correlated to experimental measurement.[100]

3. Effects of electronic polarization on H_2O adsorption in MIL-53(Cr)

The molecular-level characterization of the structure and dynamics of water in confining environments is key to understanding many processes of relevance to chemistry,[113-114] geology,[115] and biology.[116] Furthermore, determining how the thermodynamic behavior and molecular mobility of water change upon confinement is of fundamental importance on its own for the development of a microscopic understanding of the unique properties of water under different conditions.[117-118] In this regard, it has been shown that the interactions with chemically different substrates significantly perturb the water hydrogen-bond network, leading to pronounced changes in the freezing and melting behavior,[119] and orientational dynamics.[120-121] The impact of nuclear quantum effects on the water properties upon confinement has also been studied.[122-123]

Metal-organic frameworks (MOFs) represent a relatively new class of nanoporous materials consisting of metal ions or clusters coordinated to organic molecules that act as linkers to form extended three-dimensional networks.[14] Because of their chemical diversity, high surface area, and porosity, MOFs have recently received increasing attention for potential applications in gas storage and separation, catalysis, sensing, nonlinear optics, luminescence and magnetism.[56] In particular, it has been shown that MOFs exhibit exceptional CO_2 adsorption capacity under equilibrium conditions,[124-126] which makes these materials promising candidates for CO_2 capture and separation from flue gas emitted by fossil-fuel power plants. However, before MOFs can actually find practical applications in large-scale technologies, it is critical to assess their stability and adsorption capacity under realistic conditions.[127] In particular, since the flue gas is not pure CO_2 but rather a mixture of ~12% CO_2, ~73% N_2 and ~11% H_2O (with the balance

composed of O_2, SO_x and NO_x), with H_2O effectively competing for the binding sites within the framework and directly impacting the stability of the overall structure, a molecular-level characterization of the MOF-water interactions is needed.[30]

Experimentally it has been shown that the behavior of MOFs in the presence of water displays a large degree of variability. Some frameworks degrade irreversibly under low-hydration conditions,[39] while other structures remain highly stable even when completely immersed in water.[128-129] Water adsorption isotherms at 303 K have been reported for water-resistant three-dimensional pillared layer MOFs,[130] and analogous measurements have shown that the HKUST-1 and DUT-4 materials become unstable when put in direct contact with water.[131] By contrast, MIL and ZIF materials display high hydrothermal stability.[131] Framework functionalization with water-repellent groups has recently been shown to represent a viable route for improving the stability of MOFs under hydrated conditions.[132-134] In general, it has been found that the hydrothermal stability of MOFs correlates with the estimated dissociation energy of the metal-ligand bond.[60] In this regard, earlier computer simulations with classical force fields suggested that the displacement of the BDC (1,4-benzenedicarboxylate) organic linkers coordinated to the Zn atoms in MOF-5 was likely involved in the dissociation process.[39] Subsequent simulations performed with a reactive force field found that water hydrolysis, promoted by direct interactions of H_2O molecules with the Zn atoms of the framework, was responsible for the collapse of the structure.[135] Interestingly, the decomposition of DMOF-1, which is structurally related to MOF-5, appears to occur via a different mechanism that involves the removal of the DABCO (1,4-diazabicyclo[2,2,2]octane) pillars.[136] This has found support from recent computer simulations indicating that the

dissociation energy of the DABCO linkers in DMOF-1 is relatively low, which implies that these ligands can be easily displaced by guest molecules capable of interacting more strongly with the Zn ions of the framework.[68] Although the presence of water in the MOF nanopores in general limits the adsorption of other guest molecules, in some cases the hydration of open metal sites can actually increase the amount of CO_2 that can be adsorbed under mild conditions relative to the dehydrated material.[34]

Computer modeling plays an important role in the characterization of the adsorption capacity of MOFs, providing molecular-level insights into the binding sites, adsorption energies, and distribution of guest molecules within the nanopores. With very few exceptions,[137-140] all computer simulations of MOFs have been carried out with fixed charge (i.e., non-polarizable) force fields. Although common non-polarizable force fields incorporate polarization effects in an average fashion, it is recognized that these models are not capable of correctly reproducing the variation of the electrostatic environment in inhomogeneous molecular systems.[141] It is also important to note that the behavior of molecules adsorbed in the MOF nanopores can vary significantly as a function of loading, and, importantly, can be qualitatively different from that of the bulk phase, which is generally used as the reference state in the parameterization of non-polarizable force fields.

In this study, the effects of electronic polarization on water adsorption in MIL-53(Cr) are investigated using *ab initio* calculations and molecular dynamics (MD) simulations. MIL-53(Cr) is a three-dimensional MOF that is built-up from infinite chains of corner-sharing $CrO_4(OH)_2$ clusters interconnected by terephthalate linkers.[142] MIL-53(Cr) belongs to a family of MOFs that undergo reversible structural transitions (the so-

called "breathing" effect) in response to external stimuli. In particular, it has been shown that the unit cell of MIL-53 crystals can shrink up to 32% in volume upon hydration.[61-62]

A periodic system consisting of 32 MIL-53(Cr) unit cells was used in all MD simulations. To explicitly take into account polarization effects, a fully polarizable Thole-type model (TTM)[102] of MIL-53(Cr) was developed based on the flexible force field of Ref. 61. Specifically, atomic polarizabilities (α) were added to the framework atoms, while retaining the original atomic partial charges and parameters for the bonded and non-bonded interactions. The atomic polarizabilities for the H, C, and O atoms were taken from Ref. 143 while the corresponding values for the Cr(III) atoms were taken from Ref. 144. The water molecules were represented by the *ab initio* based and polarizable TTM3-F force field.[145] According to Thole's approach, an effective density, $\rho(r)$, replaces the interactions between point charges/dipoles,

$$\rho(r) = \frac{1}{A^3}\frac{3a_s}{4\pi}\exp\left[-a_s\left(\frac{r}{A}\right)^3\right] \tag{3.1}$$

The dimensionless parameter a_s, which determines the width of the density, was kept at the TTM3-F value (a_s = 0.175), while $A = (\alpha_i \alpha_j)^{1/6}$ with α_i and α_j being the atomic polarizabilities of atoms *i* and *j*, respectively. For comparison, MD simulations with the rigid TIP4P/2005[110] and flexible aSPC/Fw[112] water models were also carried out using the original non-polarizable MIL-53(Cr) force field.[61] In all cases, the parameters associated with the non-bonded framework-water interactions were obtained using the Lorentz-Berthelot mixing rule.[100] A series of MD simulations were carried out for different water loadings (N_{H_2O}), ranging from 1 to 20 H_2O molecules per unit cell. The

water molecules were initially distributed uniformly in the nanopores and each system was allowed to relax during a 1 ns simulation carried out at T = 300 K and P = 1 atm in the constant stress and constant temperature (NσT) ensemble. The temperature and pressure were maintained using the Nosé-Hoover thermostat and barostat with relaxation times of 1 ps and 5 ps, respectively.[100] The structural and thermodynamic properties of water inside the MIL-53(Cr) nanopores were then calculated from NσT simulations of 500 ps. In all cases, the equations of motion were propagated according to the velocity-Verlet algorithm with timesteps Δt = 0.5 fs and 0.2 fs for the non-polarizable and polarizable force fields, respectively. The short-range interactions were truncated at an atom-atom distance of 10.0 Å, while the electrostatic interactions were treated using the particle mesh Ewald method and the standard Ewald sum in simulations with the non-polarizable and polarizable force fields, respectively.[100] The simulations with the non-polarizable force fields were carried out with DL_POLY4[146] while those with the TTM force field were performed using a modified version of DL_POLY2.[147]

Density functional theory (DFT) calculations were initially performed to characterize the MIL-53(Cr)-water interactions and, consequently, assess the accuracy of both the non-polarizable and polarizable force fields. For this purpose, a reduced model of MIL-53(Cr) was built containing six Cr(OH)[O_2C-C_6H_4-CO_2] units (Figure 3.1). Six Li^+ ions were also included in the model system to coordinate the free $-CO_2^-$ groups of the terephthalate linkers, while the hexacoordination of the Cr(III) atoms was maintained by adding two HCO_2^- and three H_2O molecules. All calculations were performed with Gaussian 09[148] using the M062X density functional.[88] The cc-pVDZ basis set was used for C, H, O and Li,[77] while the LANL2DZ basis set was used for the Cr atoms.[149] The

M062X functional was chosen because it was shown to provide an accurate description of the electronic properties of DMOF-1, another breathing MOF,[68] as well as of hydrogen-bonded systems.[88] An appropriate initial guess was used to reproduce the correct spin configuration of the Cr(III) atoms and, consequently, the experimentally measured antiferromagnetism of MIL-53(Cr).[62] To model the water-framework interactions, a single H_2O molecule was placed in the central nanopore of the reduced MIL-53(Cr) model with the oxygen atom pointing towards the hydrogen atom of the hydroxyl ($-OH^-$) group of the framework (Figure 3.1). This specific orientation was chosen because it was found that the water molecules adsorbed in MIL-53(Cr) interact with the framework preferentially via hydrogen bonds to the $-OH^-$ groups.[61] Potential energy scans were then performed by moving the water molecule within the nanopore along the *x* and *y* directions indicated in Figure 3.1. The comparison between the M062X potential energy profiles and the corresponding curves obtained using the non-polarizable and polarizable models is shown in Figure 3.2. The three different force fields provide similar agreement with the corresponding *ab initio* data, reproducing with reasonable accuracy the shape of the potential energy curves as well as the equilibrium positions.

Direct insights into the effects of electronic polarization on the adsorption of water in the MIL-53(Cr) nanopores were obtained from MD simulations. As discussed in detail in Ref. 61, MIL-53(Cr) undergoes two successive transitions from a large to a narrow pore structure and then from a narrow to a large pore structure as a function of water loading. The variation of the unit cell volume as a function of the number of H_2O molecules adsorbed per unit cell is shown in Figure 3.3a. Similar results are obtained with all three force fields indicating that the breathing behavior of MIL-53(Cr) is not

specifically dependent on the description of the underlying interactions but rather is related to the effective volume occupied by the H_2O molecules. It is important to mention that some differences exist between the present results and those reported in Ref. 61, which are due to slight different distributions of the water molecules within the nanopores.[150] To characterize the variation of the molecular properties as a function of loading, the distributions of the water dipole moments, P(μ), for $N_{H_2O} = 3, 5, 7, 10, 14, \text{and } 20$ calculated with the TTM force field are shown in Figure 3.3b. It can be seen that the average value of the molecular dipole moment increases, with the distributions becoming significantly broader, as N_{H_2O} increases. This directly correlates with the more polarizing environment and larger number of possible hydrogen-bond configurations that exist when the H_2O molecules fill the MIL-53(Cr) nanopores. Interestingly, the average H_2O dipole moment decreases between $N_{H_2O} = 10$ and $N_{H_2O} = 14$ as a result of the transition from the narrow to the large pore structure.

Figure 3.4 shows the radial distribution functions (RDFs) describing the spatial correlations between the atoms of the H_2O molecules and those of the framework. A specific comparison is made between the Ow-Ho, Ow-C1, and Ow-Ow RDFs calculated with the three different force fields with the atomic labels being defined in Figure 3.1. The comparison between all other RDFs is reported in Appendix A. Large qualitative differences are found between the RDFs obtained from simulations with the non-polarizable and polarizable force fields. In particular, independently of the water loading, the polarizable TTM force field predicts a more localized water structure near the hydroxyl group of the framework as illustrated by the persistence of a sharp peak located

at ~2.0 Å in the Ow-Ho RDFs. This first peak, which effectively represents H_2O molecules hydrogen-bonded to the $-OH^-$ group, is found at slightly larger Ow-Ho separations in the RDFs calculated with the TIP4P and aSPC/Fw water force fields for $N_{H_2O} \leq 7$ and then disappears at higher water loading. The different evolution of the Ow-Ho RDFs as a function of N_{H_2O} implies that, at higher loading, the non-polarizable force fields predict the water molecules to interact preferentially with each other rather than with the framework. Based on the agreement with the DFT potential energy curves calculated for a single water molecule within a MIL-53(Cr) nanopore (Figure 3.2), this different behavior appears to be related to many-body water-framework and water-water polarization effects that cannot be effectively captured by the TIP4P/2005 and aSCP/Fw non-polarizable force fields.

Appreciable differences, which become smaller as the number of water molecules per unit cell increases, also exist in the Ow-C1 and Ow-Ow RDFs. These differences can be understood by considering that, especially at low loading, the properties of the H_2O molecules adsorbed in the MIL-53(Cr) nanopores are significantly different from those of bulk water, and consequently cannot be accurately described by the TIP4P/2005 and aSPC/Fw models that have been parameterized to reproduce the properties of the liquid phase. This directly correlates with the variation of the H_2O dipole moment as a function of loading calculated with the TTM force field (Figure 3.3b). Since the OH vibrational frequencies of the H_2O molecules are extremely sensitive to the surrounding environment,[151] linear and nonlinear vibrational spectroscopy can be used to provide direct insights into the molecular structure and distribution of H_2O molecules inside the

MIL-53(Cr) nanopores. In this regard, work is in progress in our group to determine the spectroscopic properties of water in MIL-53(Cr) using the TTM3-F model, which has been shown to predict accurate linear and nonlinear infrared spectra of the liquid phase.[152-153]

In summary, this study demonstrates that electronic polarization effects play an important role in the adsorption of water in MIL-53(Cr) and, very likely, in other metal-organic frameworks containing both polar and nonpolar subunits. Specifically, a fully polarizable TTM force field based on the Thole model was developed and applied to the characterization of the water behavior inside the MIL-53(Cr) nanopores as a function of loading. The comparison with DFT calculations shows that both non-polarizable and polarizable models reproduce with reasonable accuracy the interactions of a single water molecule with the MIL-53(Cr) framework. However, MD simulations indicate that the spatial distributions of the H_2O molecules within the MIL-53(Cr) nanopores calculated with the polarizable TTM model are qualitatively different from those obtained using common fixed-charge water models. These differences can be related to the variation of the water dipole moments as a function of loading which give rise to many-body water-framework and water-water effects that cannot be reproduced by non-polarizable force fields. The present analysis suggests that polarization effects can significantly impact the binding energies and spatial distributions of H_2O molecules in the nanopores, and, consequently, should be taken into account explicitly in simulations of molecular adsorption in MOFs under hydrated conditions.

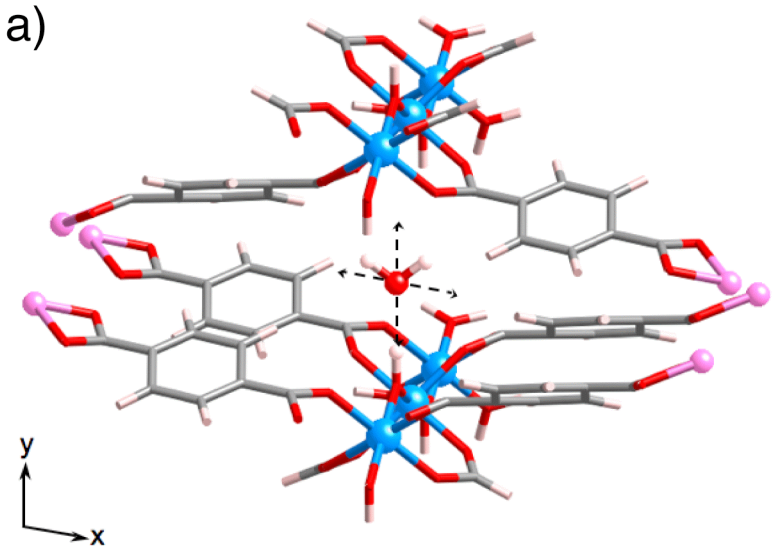

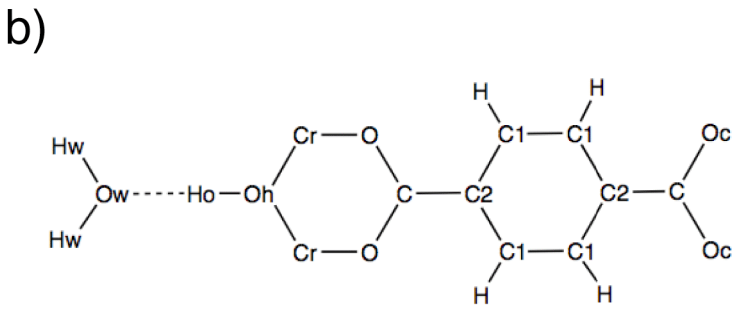

Figure 3.1 – MIL-53(Cr) models and atom labels
(a.) Schematic representation of the reduced MIL-53(Cr) model used in the DFT calculation. Also indicated as dashed lines are the x and y directions along which the potential energy scans were performed. Color scheme: Blue = Cr, red = O, gray = C, white = H, pink = Li.
(b.) Atom labels used in the definition of the RDFs.

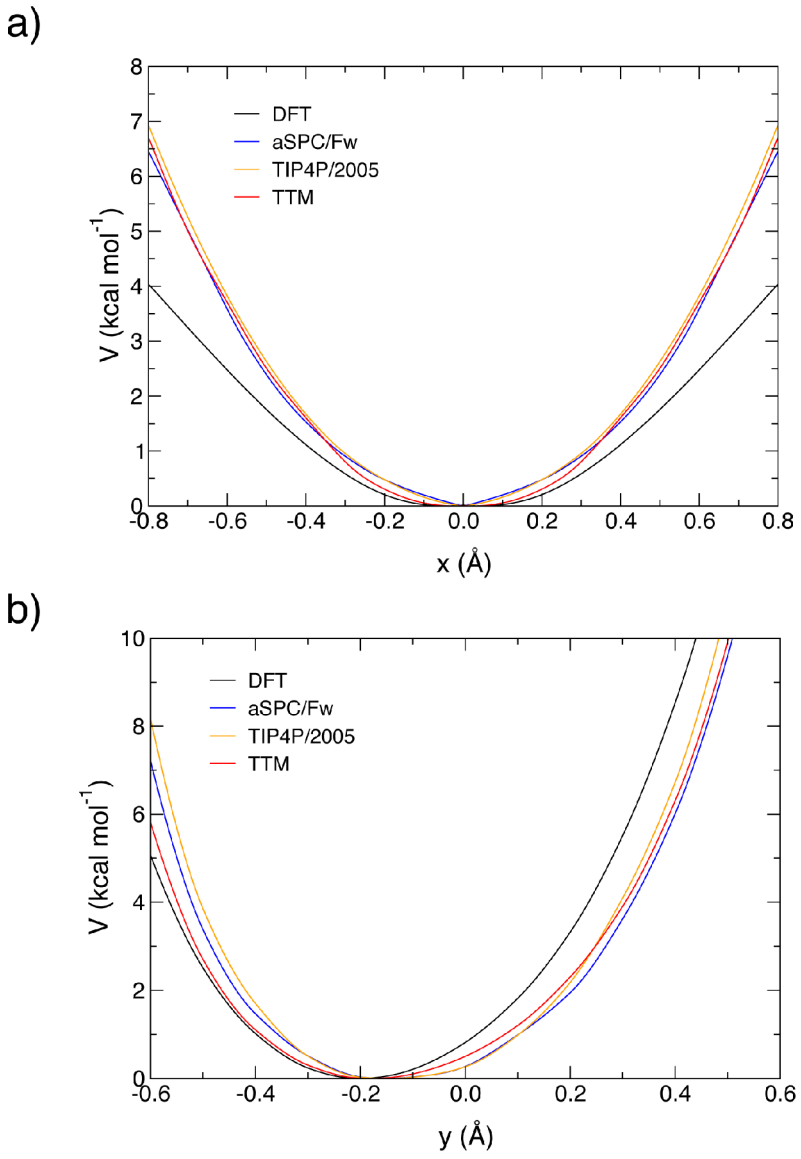

Figure 3.2 – Interaction between MIL-53(Cr) and H_2O
Potential energy curves corresponding to the interaction of a single water molecule with the MIL-53(Cr) framework calculated along the *x* and *y* directions defined in Figure 1a. Black: DFT calculations with the M062X functional, blue: calculations with the non-polarizable MIL-53(Cr) force field combined with the aSPC/Fw water model, orange: calculations with the non-polarizable MIL-53(Cr) force field combined with the TIP4P/2005 water model, red: calculations with the polarizable TTM force field of MIL-53(Cr) combined with the TTM3-F water model.

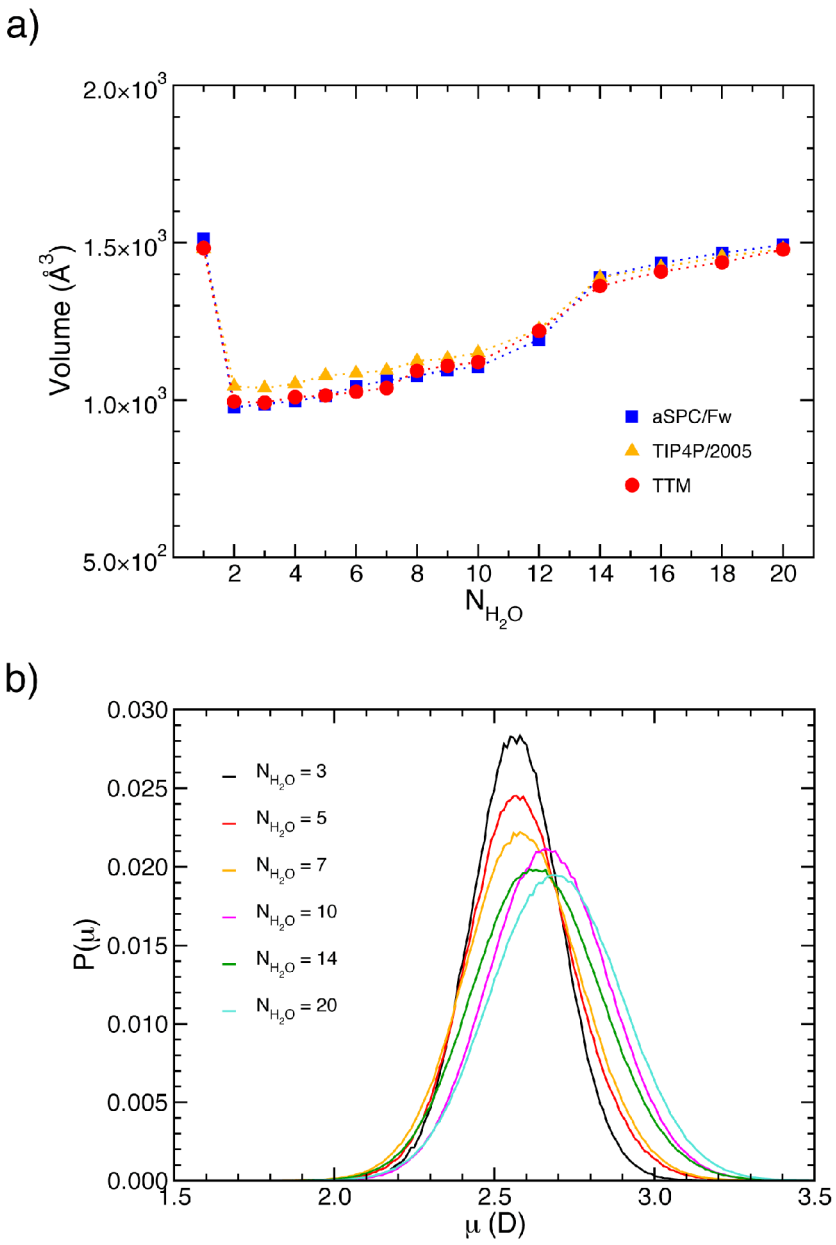

Figure 3.3 – MIL-53(Cr) unit cell volume vs H_2O loading and P(μ) of H_2O.
(a.) Variation of the MIL-53(Cr) unit cell volume as a function of water loading from MD simulations with the aSPC/Fw (blue), TIP4P/2005 (orange), and TTM (red) water models.
(b.) Probability distribution of the water dipole moment, P(μ), calculated using the TTM force field as a function of water loading.

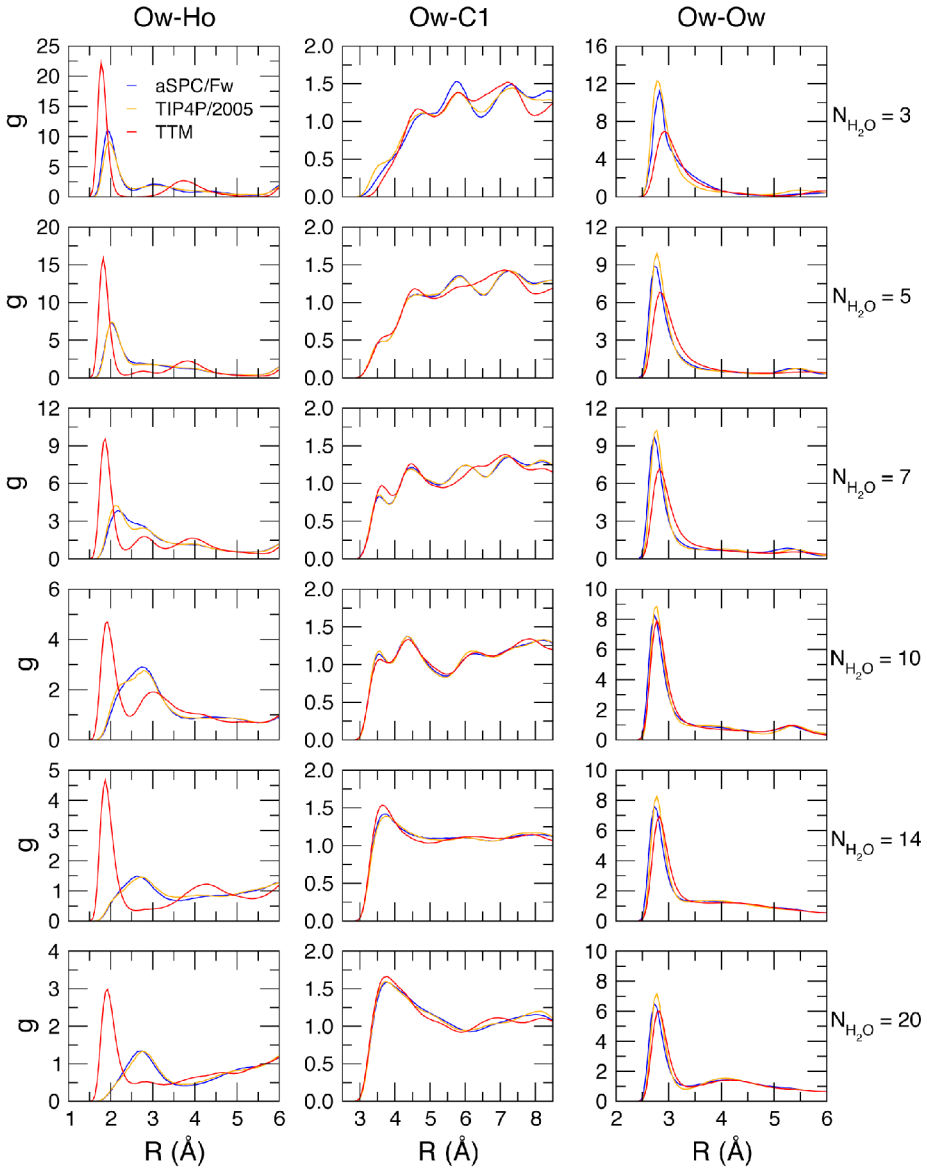

Figure 3.4 – Comparison between the Ow-Ho, Ow-C1, and Ow-Ow RDFs (radial distribution functions) calculated using the non-polarizable aSPC/Fw (blue) and TIP4P/2005 (orange) force fields, and the polarizable TTM (red) force field as a function of water loading, N_{H_2O}. The atom labels are defined in figure 3.1b.

Chapter 3, in full, is currently being prepared for submission for publication of the material. Cirera, J.; Sung, J. C.; Howland, P. B.; Paesani, F. The dissertation author was a contributor and co-author of this material.

4. Breathing Behavior of DMOF-2,3-NH_2Cl versus DMOF-2,5-NH_2Cl

DMOF-1 was originally synthesized by Dybtsev and co-workers by combining $Zn(NO_3)_2$, terephthalic acid (H_2bdc), and 1,4-diazabicyclo[222,]octane (DABCO) in DMF and heating at 110 °C for 2 days to yield a solvated crystalline product.[64] With a unit cell of [Zn (BDC)$(DABCO)_{0.5}$], DMOF-1 is a pillared MOF: its structure consists of 2D lattices of Zn dimers tetracoordinated to BDC ligands, with DABCO "pillars" coordinated between Zn atoms of adjacent lattices supporting the framework in the third dimension. The Zn cluster unit consisting of $Zn_2(COO)_4(DABCO)_2$ forms the paddlewheel configuration which is commonly seen amongst a large variety of MOFs. When evacuated, DMOF-1 has a BET surface area of 1450 m^2/g[64] with pores of dimensions 7.5 Å × 7.5 Å in the direction parallel to the DABCO nitrogens and 4.8 Å × 3.2 Å in the perpendicular direction.[19] The structure of DMOF-1 can be seen in Figures 4.1 – 4.2.

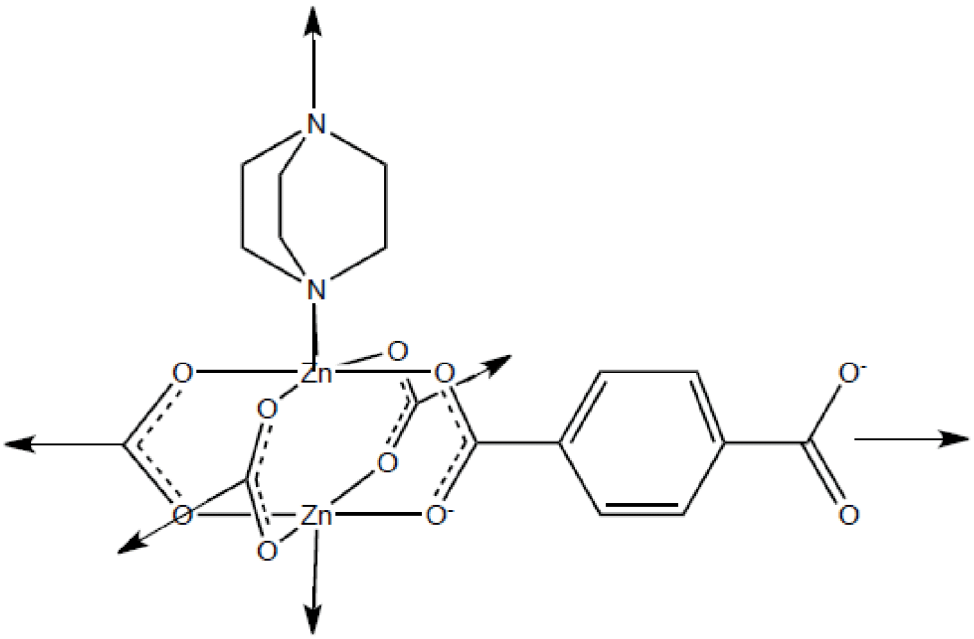

Figure 4.1 – Schematic of DMOF-1 structure. One BDC moiety and one axial DABCO moiety is shown. The arrows indicate periodic continuations of the structure.

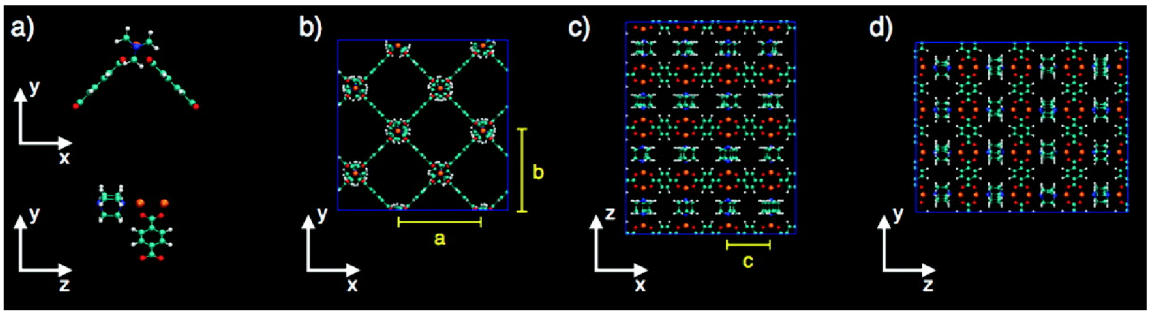

Figure 4.2 – 2D projections of DMOF-1. (a.) DMOF-1 unit cell projected in the *x-y* (top) and *z-y* (bottom) planes. (b.) DMOF-1 structure projected into the *x-y* plane. (c.) DMOF-1 sturucture projected into the *z-y* plane. Orange = Zn, cyan = C, red = O, white = H, blue = N, yellow = unit cell parameters. This figure from Ref. 68.

Unfunctionalized DMOF-1 exhibits breathing behavior upon adsorption of benzene[64] (BEN) and isopropyl alcohol (IPA)[63], but not upon the addition of CO_2 or H_2[68]. The breathing behavior of DMOF-1 is particularly interesting because it lacks highly polar groups that mediate its breathing behavior, unlike other breathing MOFs such as

MIL-53. Thus, a molecular-level characterization of its breathing behavior could lead to information relevant to the rational design of novel MOFs that take advantage of breathing behavior.

Prior work by this group simulating the breathing behavior of DMOF-1 showed that its breathing upon the adsorption of benzene is mediated by different interactions than the breathing upon the adsorption of IPA – the benzene interacts with the BDC and DABCO carbons, while the IPA forms hydrogen-bonds with BDC carboxylate oxygens. The resultant breathing behavior also differs, with the DMOF+BEN system transitioning from a LP structure to NP at 223 K with the adsorption of 0.5 – 4.0 benzene molecules per unit cell, and the DMOF+IPA system showing a bistability, transitioning first from LP to NP upon the addition of 1 to 3 IPA per unit cell, and then back to LP upon adsorption of 1 additional IPA per unit cell at 303 K. Furthermore, varying the temperature of the DMOF+BEN system from 123 to 298 K with 2 benzene molecules per unit cell adsorbed led to DMOF undergoing a NP to LP transition between 223 and 248 K, showing how temperature affects the framework structure.[68] These results imply that by modifying the framework properties at a specific temperature, DMOF-1 breathing behavior could potentially be fine-tuned such that upon the adsorption of different substances, it would transition in either the LP to NP or NP to LP direction, which would be very useful in applications such as chemical sensing or molecular switches.

As shown previously, the introduction of interesting functional groups to the BDC ligands can modulate the interactions of the framework.[29] Recently, Cohen and co-workers synthesized DMOF-1 derivatives using 2,3-NH_2Cl-BDC and 2,5-NH_2Cl-BDC as substituted BDC linkers. These two frameworks with isomeric ligands were named

DMOF-2,3-NH_2Cl and DMOF-2,5-NH_2Cl, but will be referred to here as the ortho-DMOF and para-DMOF systems respectively. In the synthetic process, $Zn(NO_3)_2 \cdot 6H_2O$ and the corresponding substituted DMOF were dissolved in DMF, and then reacted with DABCO to form a white precipitate. After filtering out the precipitate, the solution's temperature was raised from 35 ºC to 100 ºC at a rate of 2.5 ºC per minute, and maintained at that temperature for 48 hours, before being cooled back to 35 ºC at a rate of 2.5 ºC per minute. The crystals were then washed in DMF, and the solvent subsequently exchanged with chloroform over 3 days, replacing the old chloroform every 24 hours.[154]

Despite the similarity between the two frameworks, their N_2 adsorption isotherms showed a significant difference – the ortho- framework had BET surface area of nearly 1169 m^2g^{-1}, while the para- framework was nearly nonporous to N_2, with a BET surface area in the range of 6-61 m^2g^{-1}. A similar trend was observed for DMOF-2,3-NH_2Br and DMOF-2,5-NH_2Cl. Single crystal X-Ray diffraction data of the two isomers indicated that after synthesis, the ortho-DMOF structure maintains a cubic unit cell, while the para-DMOF structure is more flexible, adopting a more rhombohedral configuration.[154] The differences in unit cell and the adsorption isotherms for ortho- and para-DMOF can be seen in Figures 4.3 – 4.4.

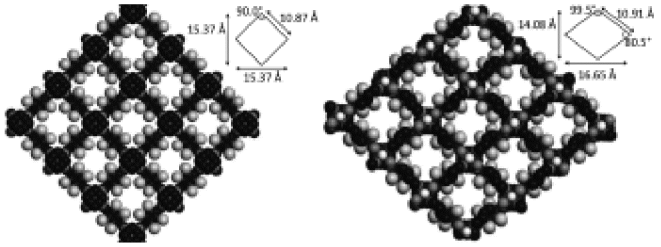

Figure 4.3 – Structures of DMOF-2,3-NH_2Cl and DMOF-2,5-NH_2Cl. The difference in unit cell shape between the cubic ortho-DMOF structure (left) and rhombohedral para-DMOF structure (right) can be clearly seen. Figure taken from Ref. 154.

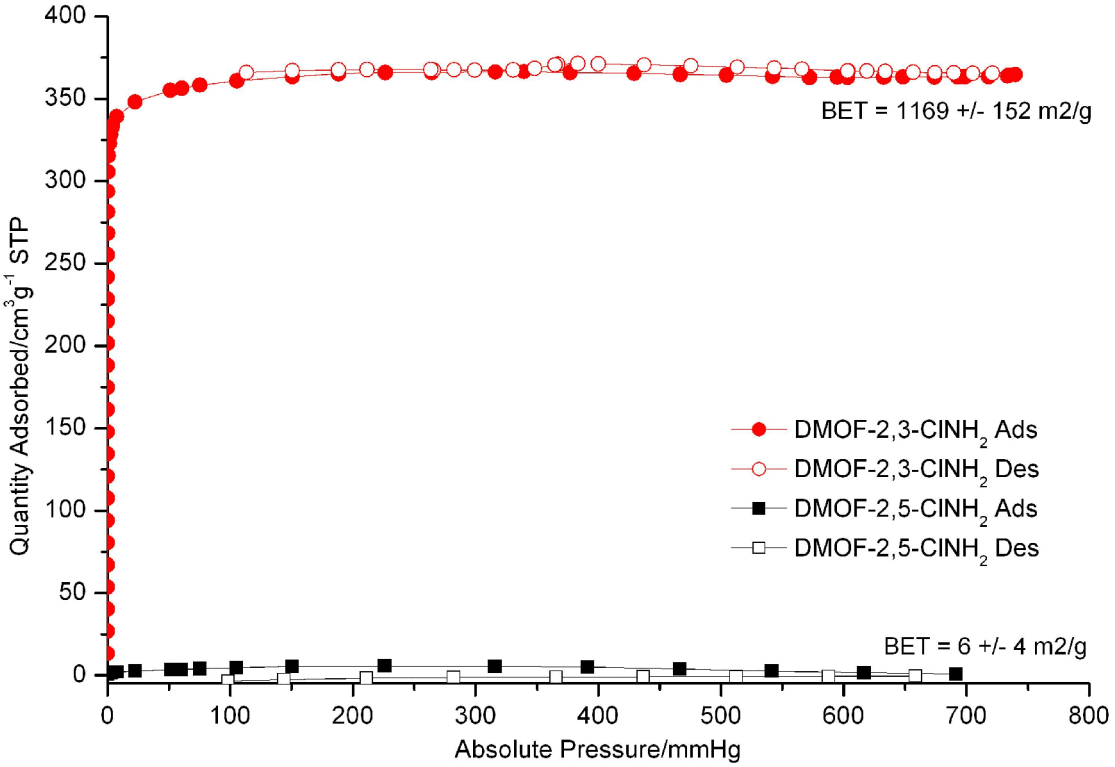

Figure 4.4 – N_2 gas sorption isotherms for DMOF-2,3-NH_2Cl and DMOF-2,5-NH_2Cl at 77 K. Figure adapted from Ref. 154.

Since making such a small change in the framework – using an ortho-disubstituted ligand instead of para-disubstituted ligand, leads to a difference in BET surface area of 2-3 orders of magnitude, determining the underlying molecular mechanism that causes this difference in N_2 adsorption behavior would yield very valuable insights on the considerations that should be taken to tune MOF flexibility.

To obtain the equilibrium geometry of the chlorine and amine substituents, a similar procedure to that used in Ref. 68 was utilized. The optimized geometry cluster consisting of unfunctionalized BDC connected to two truncated metal clusters capped by carboxylates was taken, and the ortho- and para- NH_2Cl substituted isomers generated by replacing the corresponding H atoms. All of the atoms besides the NH_2 and Cl atoms

were then fixed, and the system optimized. The substituent partial charges were calculated using the CHELPG method, [90] with the Zn van der Waals cutoff radius set to 1.0 Å, for consistency with the prior parameterization of the force field. The cc-pVDZ[77] basis set was utilized for all atoms in the DFT calculations except for Zn, for which the ECP of the aug-cc-pVDZ-PP[155] was used (though comparisons to the LANL2DZ[149] Zn ECP were made). The M062X[88] functional was likewise retained, though comparisons were made with calculations using the B3LYP[87] functional. The Gaussian 09[148] software package was utilized for all quantum chemistry calculations.

The DMOF-1 force field of Ref. 68 was designed to be transferrable amongst simulations of the framework with different guest molecules. Due to the similarities between DMOF-1 and the modified DMOF derivatives, the force field assumed to be applicable to these derivative systems as well, and the bond stretching, angle bending, torsion, and vdW parameters taken as a starting point for the ortho- and para-DMOF force fields. However, to preserve the differences in electronic structure between unfunctionalized DMOF-1 and the ortho- and para-DMOF systems as much as possible, the partial charges calculated for the ortho- and para-DMOF clusters were not averaged for the different atom types, but were instead kept at the *ab initio*-calculated values. The different components of the framework with the corresponding atom are shown in Figure 4.5, and the clusters used in the *ab initio* calculations in Figure 4.6. The systems consisting of 2 ortho- and para-DMOF unit cells, PDB files, and charges corresponding to atom index are shown in Appendix B. While the bond stretch, angle bend, and van der Waals parameters were found to describe the ortho- and para- frameworks with accuracy, preliminary simulations using the force field failed to successfully reproduce the out-of-

BDC-plane benzene rotations seen in experimental data[154]. Instead, the unfuncationalized DMOF-1 force field dihedral parameters for the O-C2-Ca-Ca interaction keep the benzene rings in the BDC plane. A comparison of the *ab* initio and force field potential energy surfaces of the framework clusters (Figure 4.6) as a function of O-C2-Ca-Ca dihedral angle from 0 to 90° showed significant differences. Thus, it was decided to tune the O-C2-Ca-Ca dihedral angle parameters in the force field for the ortho- and para-DMOF systems to more accurately describe the interaction. In order to minimize the changes from the unfunctionalized DMOF-1 force field, only the dihedral strength V and van der Waals scaling factor were changed, as small changes to those values produced greater changes in the shape of the potential energy of the dihedral angle than a change to the electrostatic scaling factor. The dihedral strengths were varied by increments of 1/10 of their starting value, and the vdW scaling factor varied in increments of 0.1, and scans of the potential energy surface of the O-C2-Ca-Ca dihedral angle were taken with the different parameters. The optimized parameters for the ortho- and para-DMOF O-C2-Ca-Ca dihedral were then determined by least-squares minimization of the error. The force field parameters are listed in Table 4.1 – 4.4.

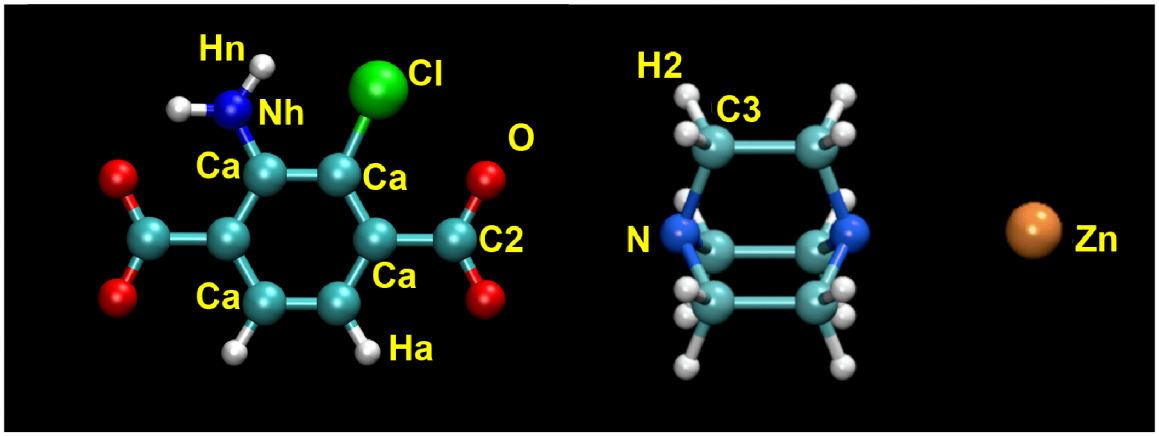

Figure 4.5 – Atom labels for the DMOF-2,3-NH_2Cl force field. The DMOF-2,5-NH_2Cl force field atom labels are identical.

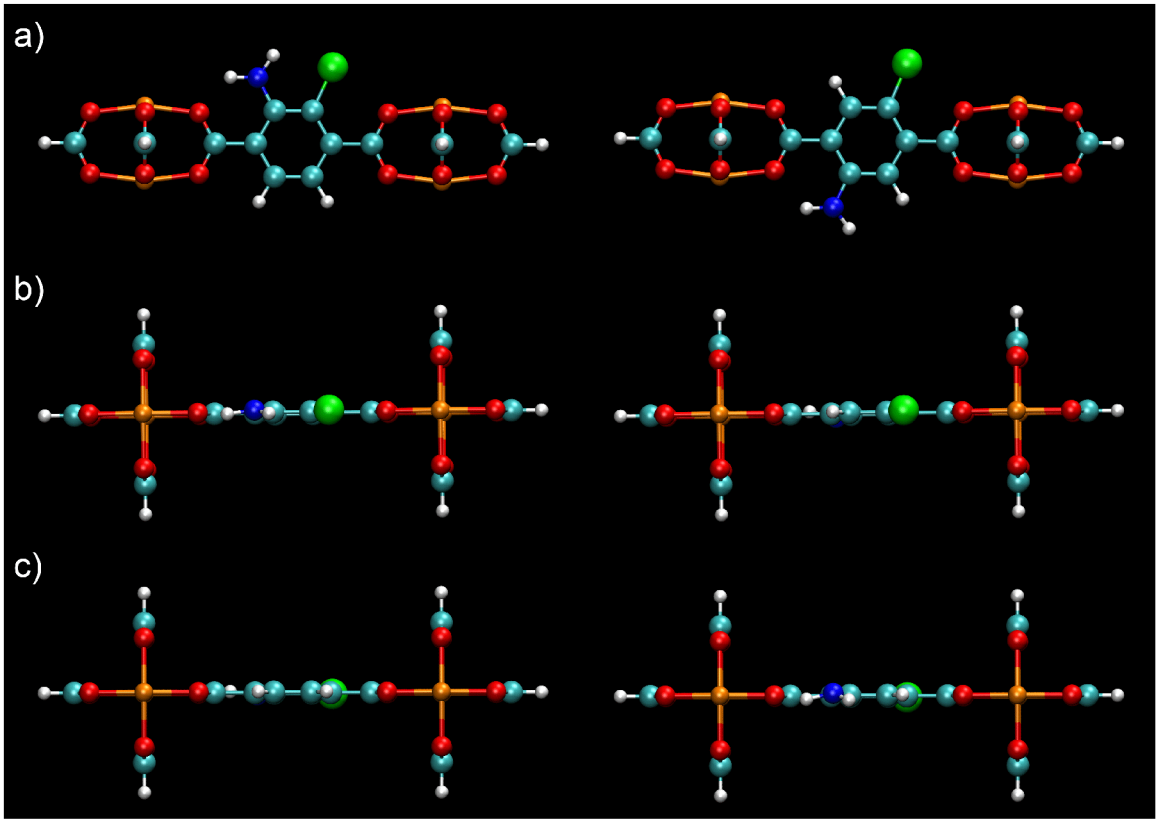

Figure 4.6 – Top and side views of the framework fragments including one substituted BDC ligand between two metal units, $[Zn_2(HCO_2)_3]$, used in the *ab initio* calculations. (a.) Top view of fragment for ortho-DMOF (left) and para-DMOF (right). (b and c.) Side views of fragment for ortho-DMOF (left) and para-DMOF (right).

Table 4.1 – DMOF-2,3-NH_2Cl and DMOF-2,5-NH_2Cl atom types and vdW parameters.

Atom Type	ε (kcal/mol)	σ (Å)
Zn	0.0125	2.495
O	0.2100	2.960
C2	0.0860	3.400
Ca	0.0860	3.400
Ha	0.0150	2.600
H2	0.0157	2.471
N	0.1700	3.250
C3	0.1094	3.400
Hn	0.0150	1.069
Nh	0.1700	3.250
Cl	0.2650	3.471

Table 4.2 – DMOF-2,3-NH_2Cl and DMOF-2,5-NH_2Cl force field bond stretch parameters.
Top: Morse potentials. Bottom: Harmonic potentials.

Bond	E_0 (kcal/mol)	k (Å^{-1})	r_0 (Å)
Zn-O	25.83	1.800	2.093
Zn-N	32.00	1.550	2.090

Bond	k (kcal/mol A^{-2})	r_0 (Å)
Zn-Zn	100.0	2.884
Nh-Hn	802.4	1.014
Nh-Ca	898.0	1.364
Ca-Ca	956.8	1.387
Ca-Cl	645.6	1.729
Ca-C2	699.4	1.480
C2-O	1296	1.214
Ca-Ha	688.6	1.087
C3-H2	671.8	1.093
C3-C3	606.2	1.535
C3-N	641.2	1.470

Table 4.3 – DMOF-2,3-NH_2Cl and DMOF-2,5-NH_2Cl force field angle bending parameters.

Angle	k (kcal/mol rad^{-2})	θ_0 (Degrees)
Zn-O-C2	5.000	125.5
Nh-Ca-Ca	138.7	120.1
Hn-Nh-Hn	80.10	114.9
Hn-Nh-Ca	98.16	116.1
Ca-Ca-Ca	134.4	120.0
Cl-Ca-Ca	125.8	119.4
Ca-Ca-Ha	96.92	120.0
C2-Ca-Ca	129.3	120.1
O-C2-Ca	137.3	123.4
O-C2-O	156.3	130.4
O-Zn-O	30.76	88.45
O-Zn-N	30.76	99.45
C3-C3-H2	92.72	110.1
C3-C3-N	132.4	110.4
C3-N-C3	128.0	110.9
H2-C3-H2	78.36	109.6
H2-C3-N	98.78	109.9

Table 4.4 – DMOF-2,3-NH_2Cl NH_2Cl and DMOF-2,5-NH_2Cl torsion parameters
(a.) Common torsion parameters for both DMOF-2,3-NH_2Cl and DMOF-2,5-NH_2Cl
(b.) Top: Torsion parameters unique to DMOF-2,3-NH_2Cl (ortho-DMOF). Bottom: Torsion parameters unique to DMOF-2,5-NH_2Cl (para-DMOF)
The electrostatic scaling factor was 0 for both the ortho- and para-DMOF systems.
a.)

Dihedral	V (kcal/mol)	ω_0 (Degree)	n	vdW Scaling
Zn-O-C2-Ca	1.640	180.00	2	1.0
Zn-O-C2-O	1.640	180.00	2	1.0
Nh-Ca-Ca-Ca	3.625	180.00	2	1.0
Nh-Ca-Ca-C2	3.625	180.00	2	1.0
Hn-Nh-Ca-Ca	1.050	180.00	2	1.0
Ca-Ca-Ca-Ca	3.625	180.00	2	1.0
Ca-Ca-Ca-Ha	3.625	180.00	2	1.0
Cl-Ca-Ca-Ca	3.625	180.00	2	1.0
Cl-Ca-Ca-C2	3.625	180.00	2	1.0
O-C2-O-Ca	1.100	180.00	2	1.0
O-Zn-O-C2	0.000	180.00	2	1.0
Ha-Ca-Ca-C2	3.625	180.00	2	1.0
C3-C3-N-C3	0.480	180.00	2	1.0
C3-N-C3-H2	0.300	0.00	3	1.0
H2-C3-C3-H2	0.156	0.00	3	1.0

b.)

Dihedral	V (kcal/mol)	ω_0 (Degree)	n	vdW Scaling
Ca-Ca-C2-O	2.014	180.00	2	0.9
Cl-Ca-Ca-Nh	3.625	180.00	2	1.0
Ha-Ca-Ca-Ha	3.625	180.00	2	1.0

Dihedral	V (kcal/mol)	ω_0 (Degree)	n	vdW Scaling
Ca-Ca-C2-O	1.785	180.00	2	0.9
Nh-Ca-Ca-Ha	3.625	180.00	2	1.0
Ha-Ca-Ca-Cl	3.625	180.00	2	1.0

The frameworks were originally synthesized using DMF, which was later exchanged with chloroform. Prior to the gas sorption experiments, the framework was placed under vacuum overnight at room temperature, and then degassed at room temperature for 12 hours or until the outgas rate was below 5 μmHg/min.[154] However, if the chloroform or DMF solvent interacted strongly enough with one of the framework

isomers, the solvent-framework interaction could potentially cause that isomer to undergo a transition into the NP form, causing the experimentally-observed difference in porosity. To investigate the effects of chloroform and DMF on the frameworks, a series of MD simulations were carried out for different chloroform and DMF loadings ($N_{chloroform}$ and N_{DMF} respectively), ranging from 0.25 to 4 solvent molecules per unit cell. The solvent molecules were initially distributed evenly in the pores, and the system allowed to relax in the constant volume (NVT) ensemble for 20 ps. The structural and thermodynamic properties of the chloroform and DMF molecules in the pores were then calculated from 1.0 ns simulations in the constant stress (NσT) ensemble, at 200 K, the temperature at which the x-ray data was taken. For all MD simulations, the equations of motion were propagated using the velocity-Verlet algorithm, with a timestep of $\Delta t = 0.1$ fs. The short range interaction radius cutoff was 9.0 Å; electrostatic interactions were treated using the particle mesh Ewald (PME) method.[104] The simulations were carried out using the DL_POLY 4[146] MD code. The force field parameters for the ortho- and para-BDC ligands were obtained from the GAFF database available in the AMBER 11 MD package[156], with the charges from the DFT calculations. The remaining framework interactions were taken from the flexible and transferable DMOF-1 force field of Jason Grosch. Initially, the chloroform and DMF were set to be modeled by rigid force fields found in the literature – parameters from the Evans force field for chloroform[157] and from the OPLS organic liquid simulation force field for DMF[98] – but it was decided ultimately to utilize a flexible force field built using GAFF.[95] To calculate the pore volumes per unit cell, vectors between the Zinc atoms corresponding to the corners of each pore were determined, and used to calculate the pore's cross-sectional area. The *c* component

vector of the framework was halved to determine the third pore vector, and its magnitude multiplied by the surface area to determine the pore volume per unit cell.

Figure 4.7 shows the ortho- and para-DMOF pore volumes per unit cell as a function of chloroform loading at a temperature of 200 K, and Figure 4.8 shows 2D projections of the ortho- and para-DMOF frameworks with 0 – 4 chloroform molecules per unit cell. The empty ortho- and para-DMOF frameworks are both in LP configurations with average pore volumes of approximately 1150 $Å^3$. If we take a change in the DMOF framework pore volume per unit cell of approximately 10% or greater to mean a transition into the NP configuration, which was essentially the criterion utilized in Chapter 3 when examining the MIL-53 unit cell pore volumes, we see that the addition of 1 chloroform molecule per unit cell causes a transition into the NP configuration for both the ortho- and para-DMOF frameworks. The addition of a second chloroform per unit cell does lead to a changes in pore volumes per unit cell for both framework isomers, but neither ortho- nor para-DMOF isomers transition back into the LP configuration. The addition of a third chloroform molecule per unit cell also does not induce an NP-LP transition. A cursory glance at Figure 4.7 seems to indicate a qualitative difference in framework pore volume per unit cell between the ortho- and para-DMOF frameworks, with a difference of nearly 250 $Å^3$. However, as can be seen in Figure 4.8, both frameworks are in fact in a rhombohedral NP configuration. The difference in pore volume is caused by a combination of the disorder in the structure of the ortho-DMOF structure and the method by which the pore volume is calculated. However, the disorder in the ortho-DMOF framework leads to an overestimation of its average pore cross-sectional area per unit cell. The addition of a fourth chloroform

molecule per unit cell causes another change in the average pore volume per unit cell, for each framework isomer. However, there is once again no NP to LP transition. The addition of a fifth chloroform molecule per unit cell to the ortho- and para-DMOF frameworks led to unphysical simulation results. This was taken to show that the maximum chloroform adsorption possible for the frameworks is between 4 and 5 molecules per unit cell.

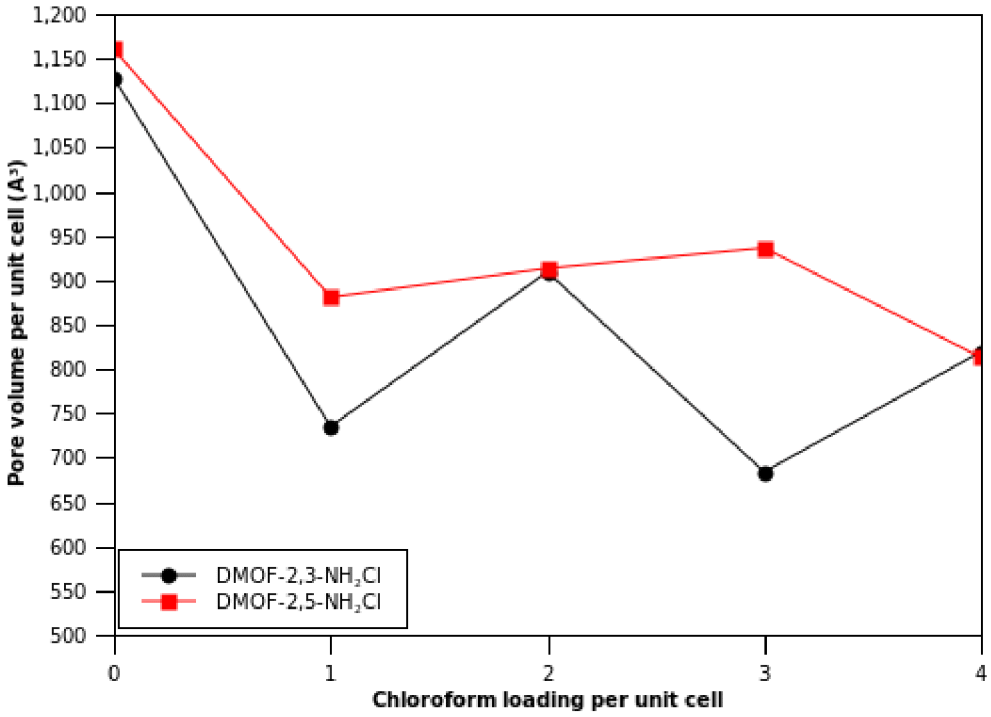

Figure 4.7 – Average pore volumes per unit cell as a function of chloroform loading.

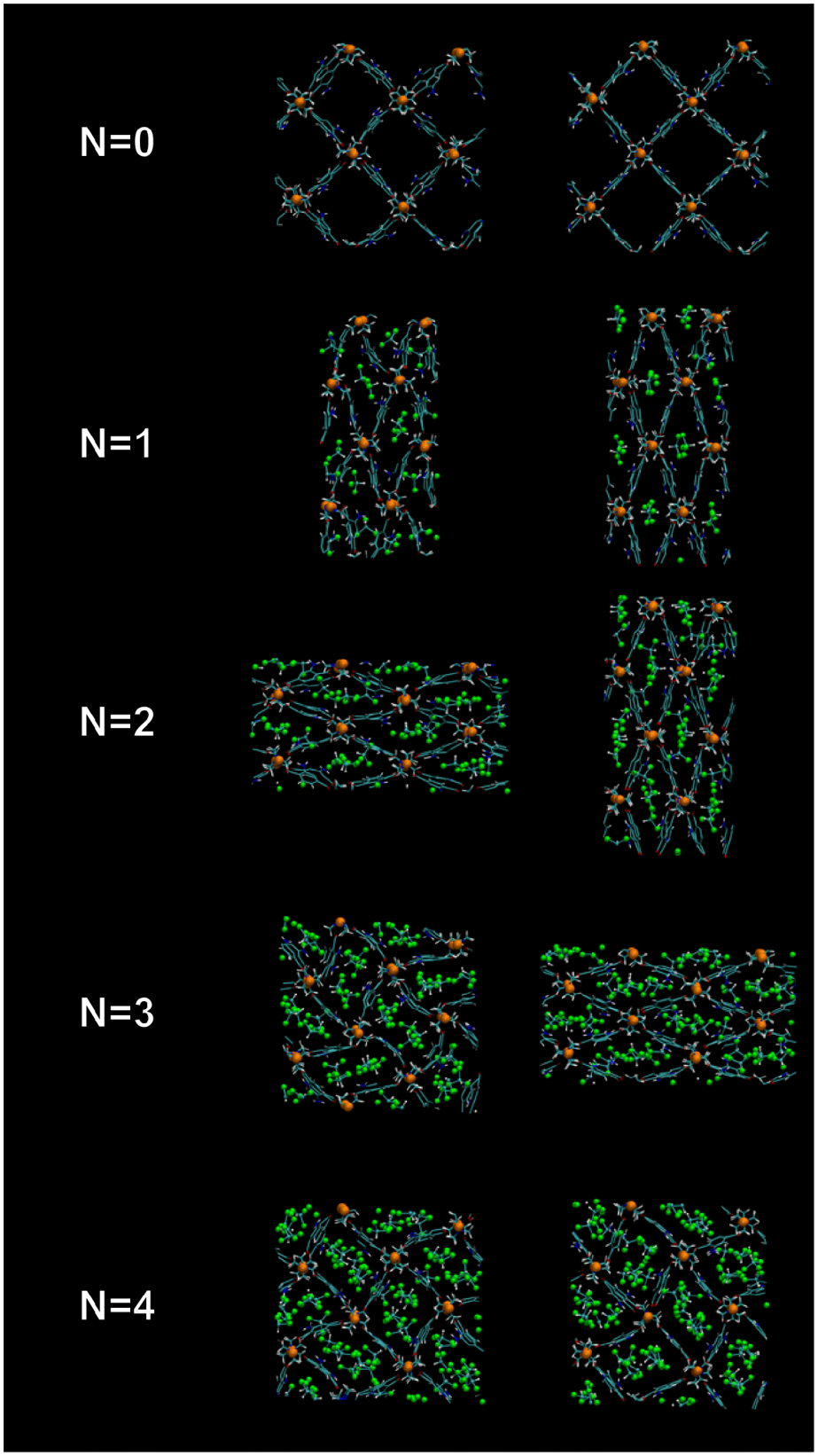

Figure 4.8 – 2D projections of $CHCl_3$ loaded DMOF-2,3-NH_2Cl and DMOF-2,5-NH_2Cl.

Figure 4.9 shows the ortho- and para-DMOF pore volumes per unit cell as a function of DMF loading at a temperature of 200 K, and Figures 4.10 show 2D projections of the ortho- and para-DMOF frameworks with 0 – 4 DMF molecules per unit cell. As with the 0 chloroform molecules per unit cell loading, the empty ortho- and para-DMOF frameworks are both in LP configurations with average pore volumes of approximately 1150 $Å^3$. The addition of 1 DMF molecule per unit cell seemingly leads to differences in behavior of the ortho- and para-DMOF systems, with the ortho-DMOF pore volume per unit cell decreasing to slightly below 1000 $Å^3$ while the para-DMOF pore volume per unit cell stays at nearly 1150 $Å^3$. However, an examination of the 2D projection shows that the para-DMOF framework is in fact closing into an NP configuration, though oscillation between the NP and LP configurations raise the volume average. As the ortho-DMOF framework is not oscillating, the graph deceptively shows a difference in behavior. The addition of the second DMF molecule per unit cell leads to a definitive transition from LP to NP. The addition of a third DMF per unit cell also seems to show a difference between the ortho- and para-DMOF framework pore volumes per unit cell. However, this is, as with the differences in the chloroform simulations, due primarily to the increased disorder in the ortho-DMOF framework leading to an overestimate of the volume. With 4 DMF molecules per unit cell, the frameworks reopen into a LP configuration. The addition of a fifth DMF molecule per unit cell leads to unphysical behavior, placing the maximum DMF loading also between 4 and 5 DMF molecules per unit cell.

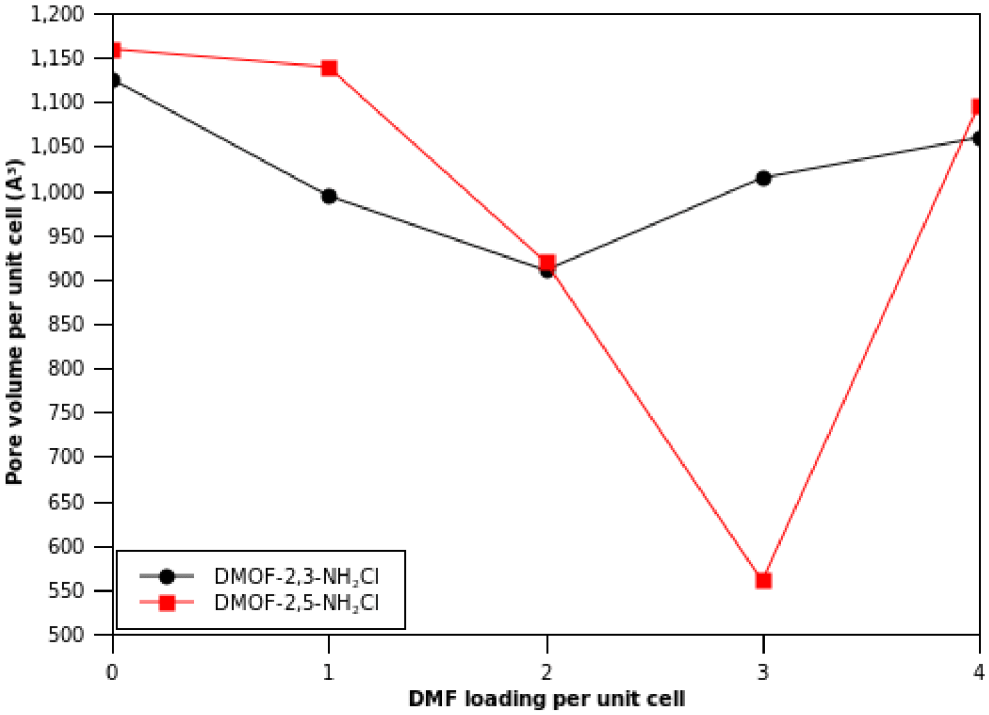

Figure 4.9 – Average pore volumes per unit cell as a function of DMF loading.

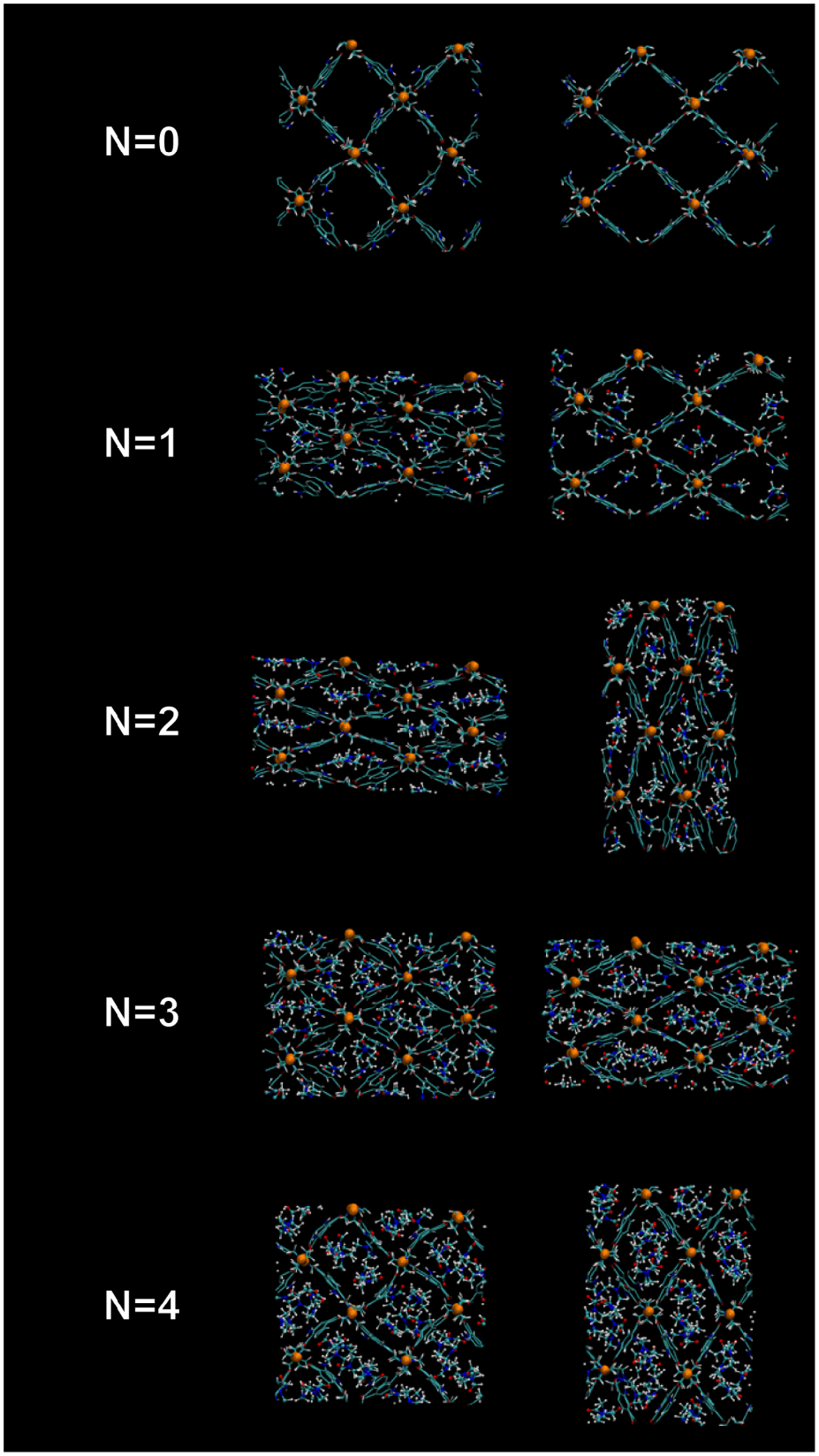

Figure 4.10 – 2D projections of DMF loaded DMOF-2,3-NH_2Cl and DMOF-2,5-NH_2Cl.

As can be seen, no significant differences exist in the behavior of the ortho- and para-DMOF frameworks when the same solvent is loaded in each. This fact, coupled with the increased disorder in one of the frameworks versus the other, seems to indicate that whatever is driving the difference in N_2 sorption behavior is not mediated by the presence of remaining solvent molecules such as chloroform or DMF, but might instead be driven by an implicit property of the framework such as the electronic structure.

Since the interaction of the framework with solvent molecules is not the cause of the difference in N_2 sorption behavior, it is possible that implicit differences in the electronic structure of the ortho-BDC and para-BDC ligands are responsible. Due to the different electronic structure in the ligands, the difference in molecular orbitals might allow one framework isomer to maintain a LP configuration after the evacuation of solvent, while the other isomer, would transition into a NP configuration. The molecular orbitals (MOs) of the 2,3-NH_2Cl-BDC and 2,5-NH_2Cl-BDC were calculated, and can be seen in Figure 4.11. While there are differences in the MOs, they are too minor to effect any difference in the adsorption.

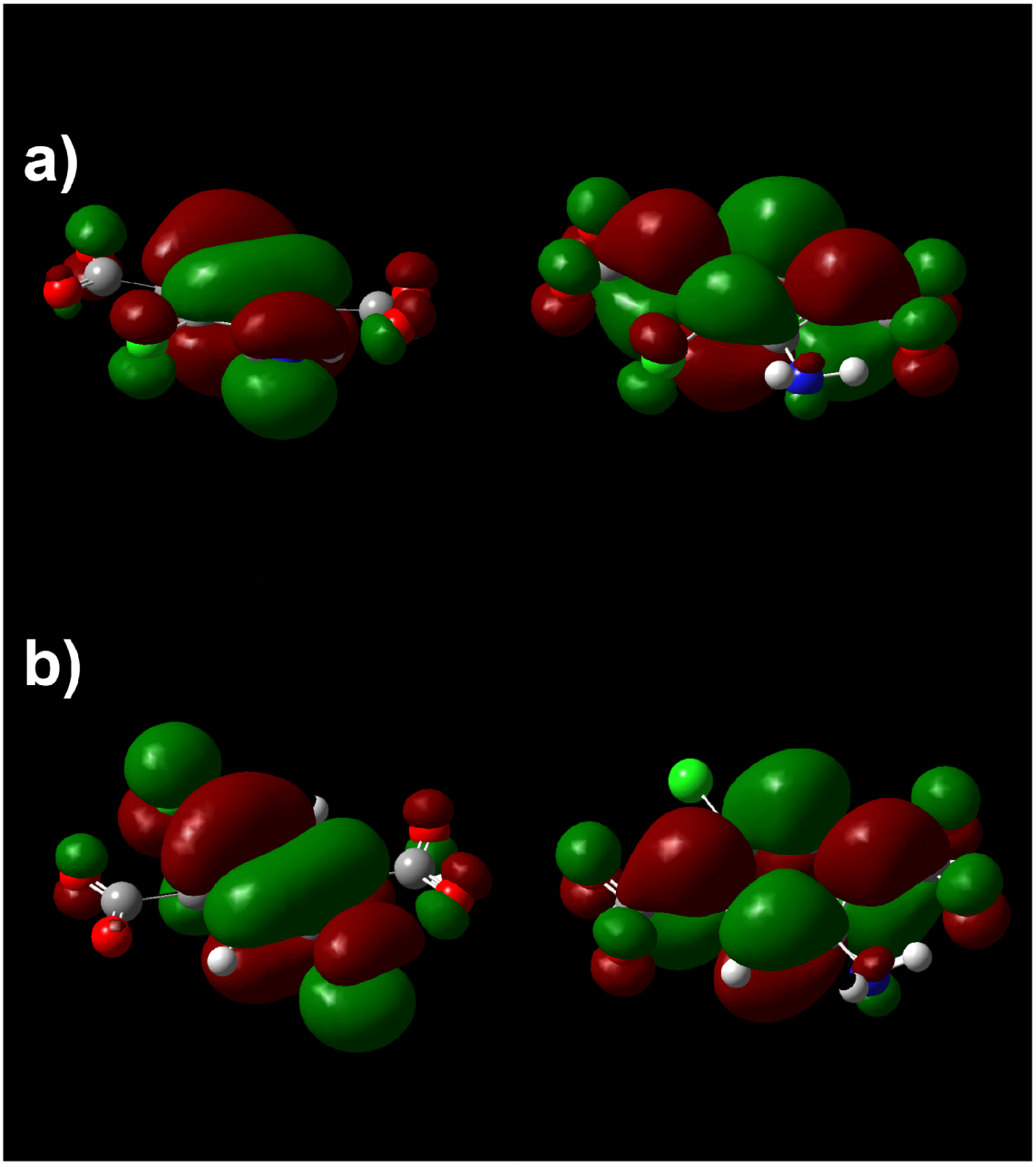

Figure 4.11 – 2,3-NH_2Cl-BDC and 2,5-NH_2Cl-BDC Molecular Orbital isosurfaces.
Contour values +0.02 e (green), -0.02 e (red)
(a.) HOMO (left) and LUMO (right) isosurfaces for 2,3-NH_2Cl-BDC.
(b.) HOMO (left) and LUMO (right) isosurfaces for 2,5-NH_2Cl-BDC.

However, the ligand system of ortho- and para-substituted BDC ligands studied does not accurately represent the configuration of the ligand in the MOF – in the systems studied, the benzene plane angle with the carboxylates was 0°, unlike in the experimental

data.[154] Furthermore, the electronic structure of the ligand in the MOF would be different due to the metal-ligand interactions that exist in the framework. To study both of these effects, the benzene moieties in the substituted BDCs of the clusters originally utilized for the calculation of atomic partial charges (Figure 4.5) were rotated relative to the plane of the carboxylates from 0 to 90° in increments of 10°, and the HOMO and LUMO molecular orbitals energies computed. These energies can be seen in Figure 4.12. As can be seen, independent of the benzene plane angle, there is no significant difference in the HOMO-LUMO bandgap between the ortho- and para-DMOF clusters, indicating a lack of implicit electronic structure difference. Thus, the electronic structure of the isomers is also not the cause of the difference in gas sorption behavior.

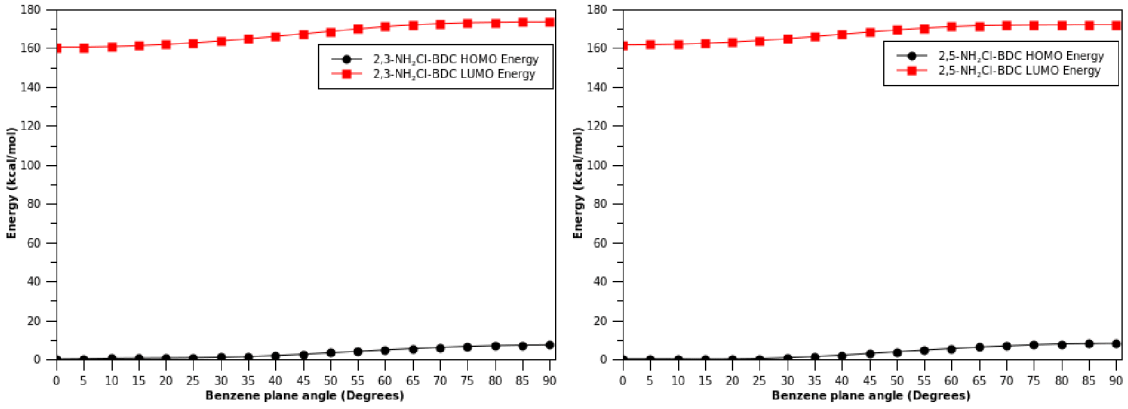

Figure 4.12 – 2,3-NH_2Cl-BDC and 2,5-NH_2Cl-BDC HOMO and LUMO orbital energies. Left: ortho-BDC. Right: para-BDC.

Though electronic structure differences are not responsible for the difference in framework behavior, a physical structural difference between the ortho- and para-BDCs could lead to different accessible pore volumes, which might lead to different gas sorption behavior. To determine the effects of the structural differences, the energies of the clusters from Figure 4.5 was calculated by DFT as a function of the benzene plane

angle. To best simulate the framework, the coordination spheres of the Zn atoms were completed using ammonia molecules to represent the DABCO ligands. The results of these calculations are shown in Figure 4.13. As can be seen, while a minor difference exists in the energies of the cluster structures, overall no significant difference exists as a function of the rotation between the ortho- and para-DMOF systems. While it is tempting to take the different minima of the ortho- and para-system energies (at 0° for the ortho system and 30° for the para system) as an interesting result, the actual energy difference is within 1 kcal/mol. It can thus furthermore be concluded that the benzene angle rotation does not significantly contribute to the difference in N_2 adsorption between the two isomers.

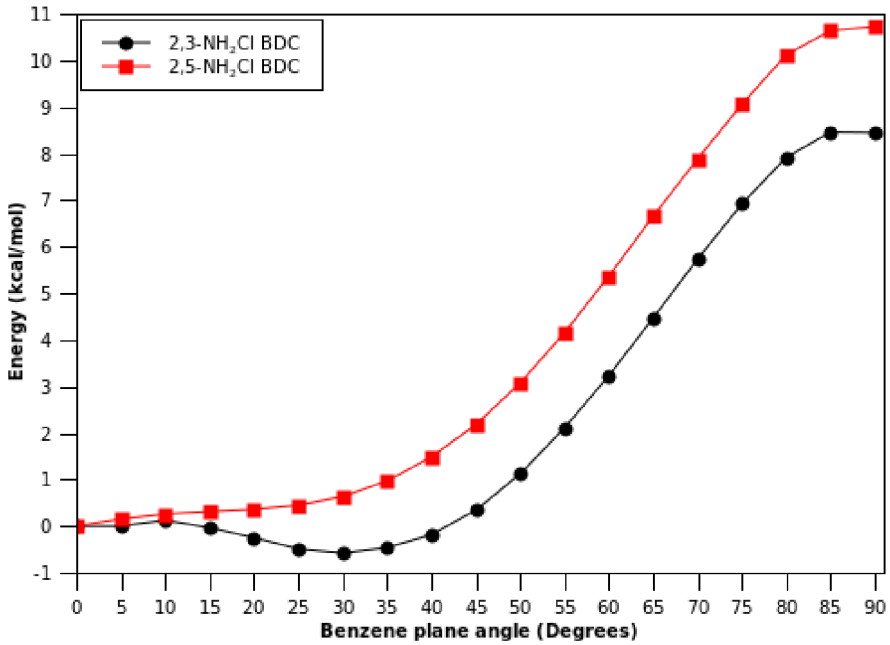

Figure 4.13 – Rotational energy profiles for the benzene ring in the substituted BDC ligands. The scan was carried out on the cluster of Figure 4.5 with NH_3 molecules completing the Zn atom coordination spheres.

Solvent effects are caused by interaction between the framework and non-framework components, and the electronic structure effects are implicit to the framework. A third possible cause of the observed difference in breathing behavior between the ortho- and para- DMOF systems involves emergent properties from after the assembly of the framework: the effects of different distributions of substituted-BDC ligands. Though the framework pore walls are known to consist of the ortho- and para-BDC linkers, the X-ray data is unable to determine if there are preferred orientations for the ligands that make up the pore. It is easy to see, particularly for para-BDC, that some orientations of the ligands will have greater steric interaction with the other BDC ligands of the same pore. Thus, it is possible that some sort of long-range order exists in the orientational distribution of the linkers, and the steric interactions of the BDCs of that particular distribution of the BDC linkers is high enough to keep the ortho-DMOF to stay in the LP configuration, but not high enough for para-DMOF to stay in the LP configuration. A figure showing two different types of distributions of linker orientations is shown in Figure 4.14. A larger cluster than that used to parameterize the charges was required to investigate this effect, due to the longer range of the distribution. This cluster consisted of two BDC molecules, bonded to a common Zn cluster, and terminated on the other end by another Zn cluster. The Zn clusters were capped by carboxylates to represent BDCs and ammonia molecules to represent DABCO. This system will be referred to as the linear system. DFT calculations were utilized to determine the optimized geometries of two high-symmetry configurations of the linear system. Two possible linear systems with unique ligand distributions were generated.

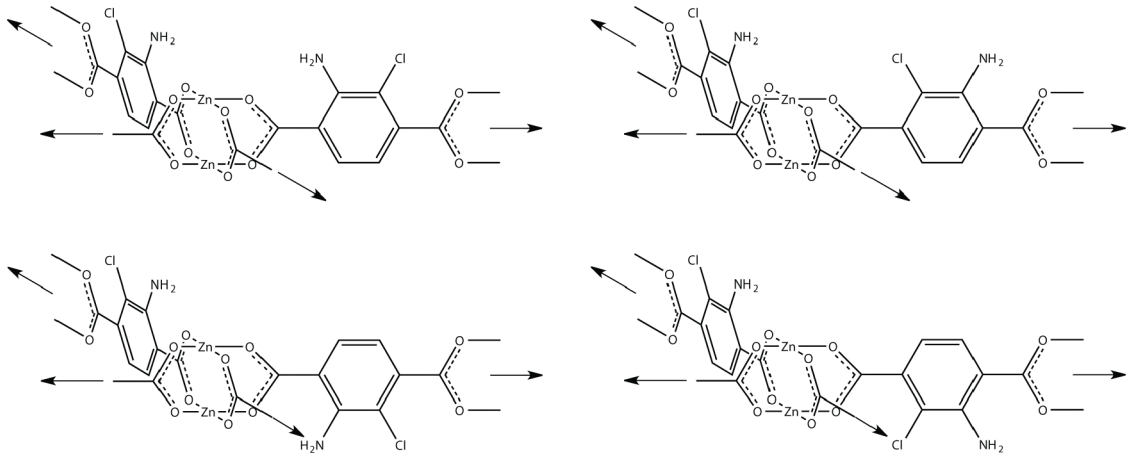

Figure 4.14 – Four possible distributions of BDC linker substituent orientation. DABCO ligands were omitted in the figure for the sake of clarity.

2D projections of the optimized structures of the two linear systems are shown in Figure 4.15. The average benzene plane angle of the first type of system is 24.97°, while the average for the second type of system is 26.80°. However, it is clear from Figure 4.15 that the capping Zn clusters have rotated into a configuration not possible in an extended framework, thus skewing the benzene plane angles. This unnatural rotation appears to stem from a lack of constraints on the capping Zn clusters. Since the clusters would not be able to rotate in the actual framework, these results are unphysical and as a whole, the optimization results are not usable. However, it is interesting to notice that in the central Zn clusters, a twisting effect can be observed in some of the Zn coordination sphere that lead to differences in the Zn-O-O-Zn dihedral angle. What is particularly interesting is that in the x-ray data, the ortho- and para- DMOF frameworks have different Zn-O-O-Zn dihedral angles. Since the two linear systems have different distributions of ligand orientation – the NH_2Cl-BDC ligands from the configuration in 4.15a have their Cl atoms facing the central Zn cluster of the system, while the NH_2Cl-BDC ligands from configuration 4.15b have their Cl atoms facing the outer Zn clusters – and both have

different central Zn-O-O-Zn dihedral angles, it seems the distribution of the orientation of the BDC ligands in the framework might have an effect on the framework properties.

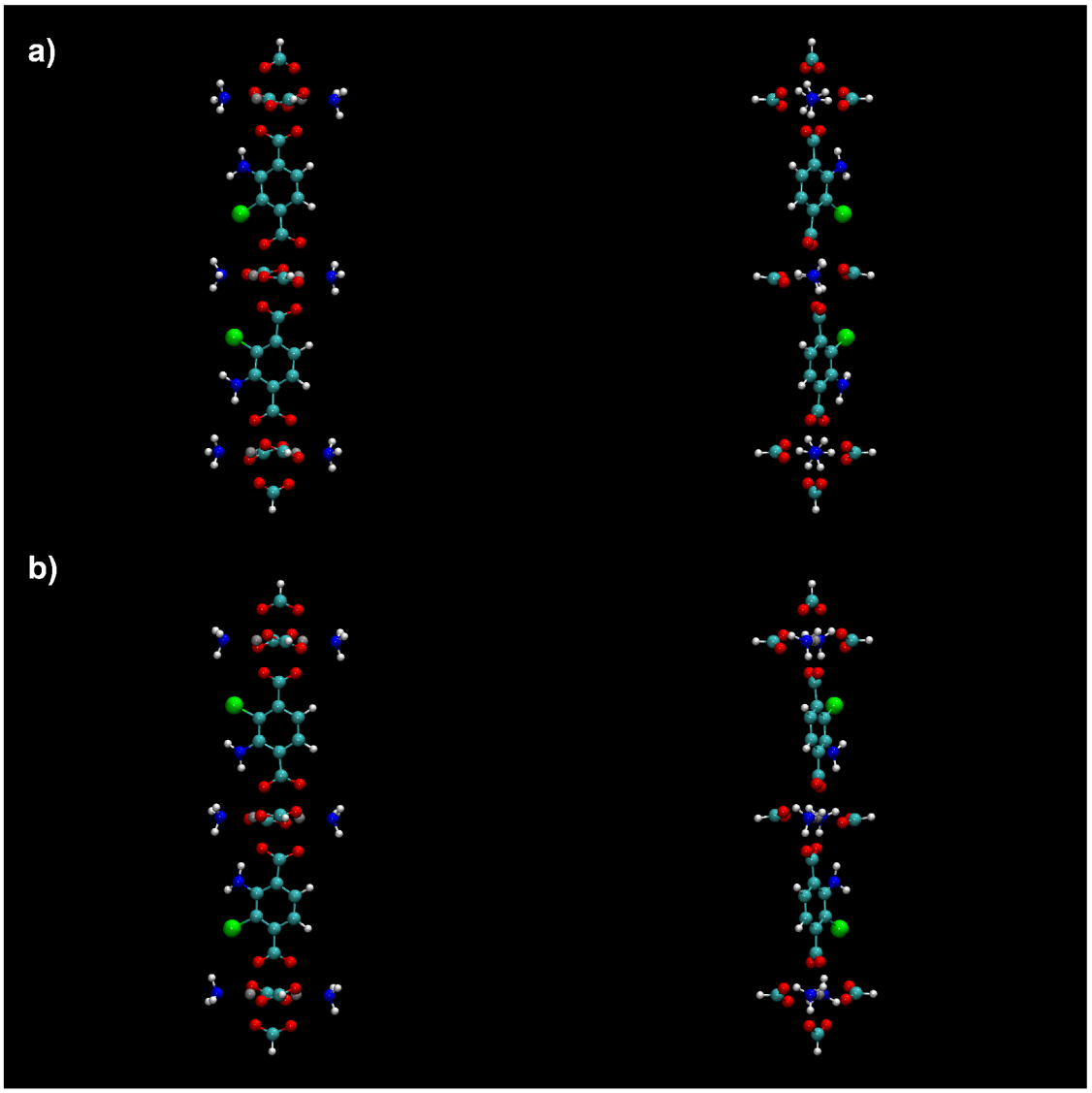

Figure 4.15 – 2D projections of the optimized ortho linear cluster in the *xy* and *zx* planes. (a) and (b) correspond to two different types of substituted ligand orientation distributions.

The para linear clusters showed similar results overall.

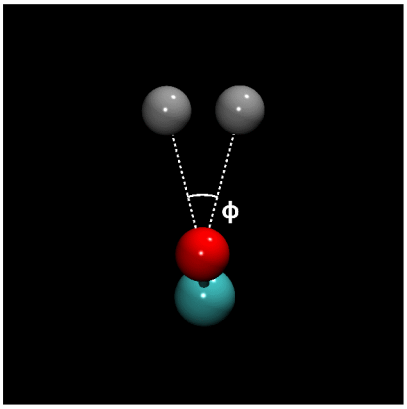

Figure 4.16 – The Zn-O-O-Zn twisting effect observed in the two linear systems. The Zn-O-O-Zn dihedral angle is marked in the figure.

The unnatural rotation observed in the ortho- and para- linear systems probably stems at least partially from the lack of interaction of the linear BDC ligands with the other ligands complexed perpendicularly to the central Zn cluster that are not modeled in the system. Consequently, a system containing perpendicular substituted BDC ligands was created to more accurately model the steric interactions of perpendicular BDCs. These systems consisted of a central Zn cluster with four coordinated substituted BDC ligands and two coordinated ammonia molecules to represent coordinated DABCO groups. Each BDC ligand was terminated not with a Zn cluster, but a Li cluster, which was capped by a single carboxylate. Replacing Zn clusters with Li clusters for quantum chemistry calculations has been shown to provide reasonable accuracy for a significant decrease in the computational cost.[158] This system will be referred to as the cross system. Every possible ligand orientation substituent distribution for the cross system was generated, for both the ortho- and para-DMOF systems. Diagrams of all possible ortho-DMOF ligand orientation distributions are shown in Appendix B. The optimized geometries and configuration energies of the 6 highest-symmetry cross configurations

were generated using DFT calculations to study the ligand orientation distribution in a system representative of the framework. The structures of these 6 structures as seen from the *c* cell vector direction are shown in Figure 4.17. These cross systems form a reasonable cluster that, with the addition of periodic boundaries, would fully model the pores of the framework. It should be noted that pairs of these 6 structures must be studied together to fully represent the framework. Structures 4.17a and 4.17b are pairs: in the full framework, each adjacent cross to 4.17a would be a 4.17b structure, and vice versa. Similarly, 4.17c and 4.17d are pairs. Each one of structures 4.17e-4.17h pairs with itself. The optimized geometries are shown in Figures 4.18 – 4.22, and the relative average energies of the pairs listed in Table 4.5. As can be seen, the unphysical rotation of the capping Li clusters, seen in the optimized geometries of the linear systems, is not present in the optimized crosses. Unfortunately, the energies of the high-symmetry cross configurations are too similar (within 2 kcal/mol) to demonstrate the exceptional stability of any particular cross configuration. Thus these calculations are insufficient to determine whether any substituted BDC ligand orientation distributions is favored, ortho or para.

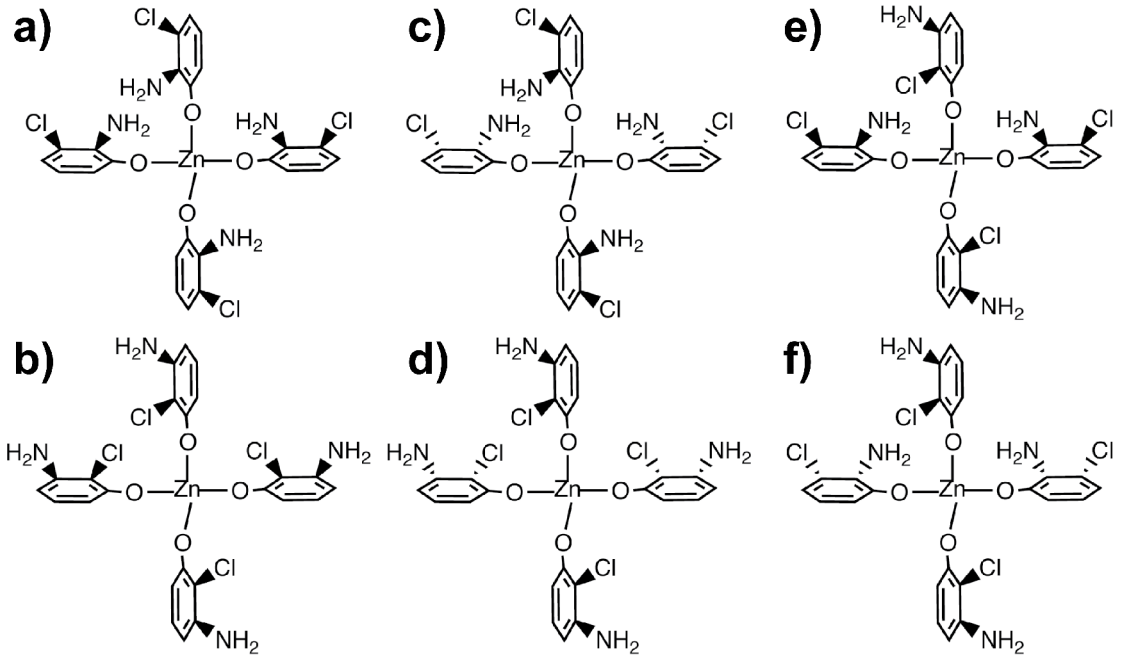

Figure 4.17 – Structures of 6 high-symmetry cross configurations. Dashed bonds correspond to substituents oriented downwards into the plane of the page, and wedge bonds to substituents oriented out of the plane of the page.

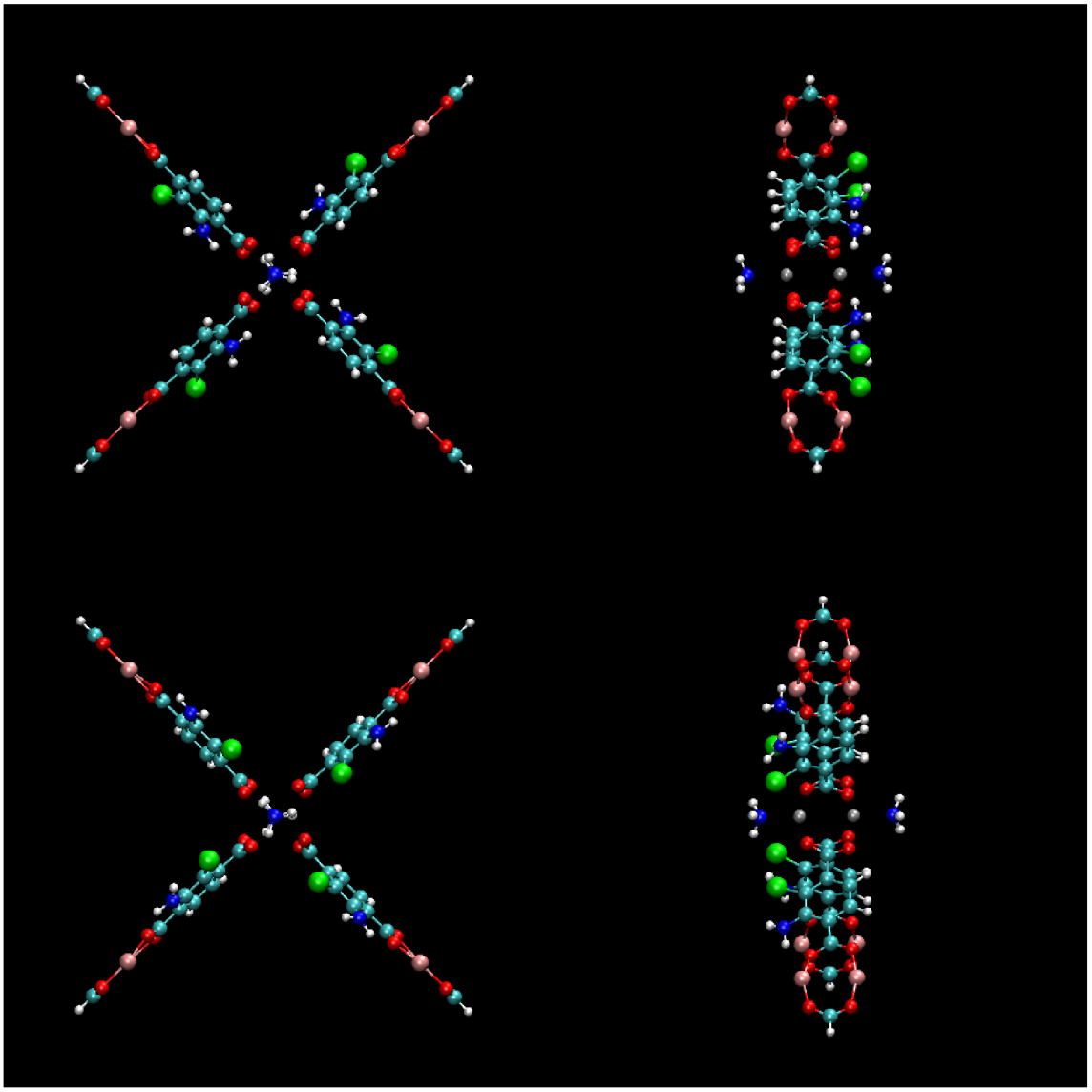

Figure 4.18 – Optimized geometries of cross configurations 4.17a (top) and 4.17b (bottom).

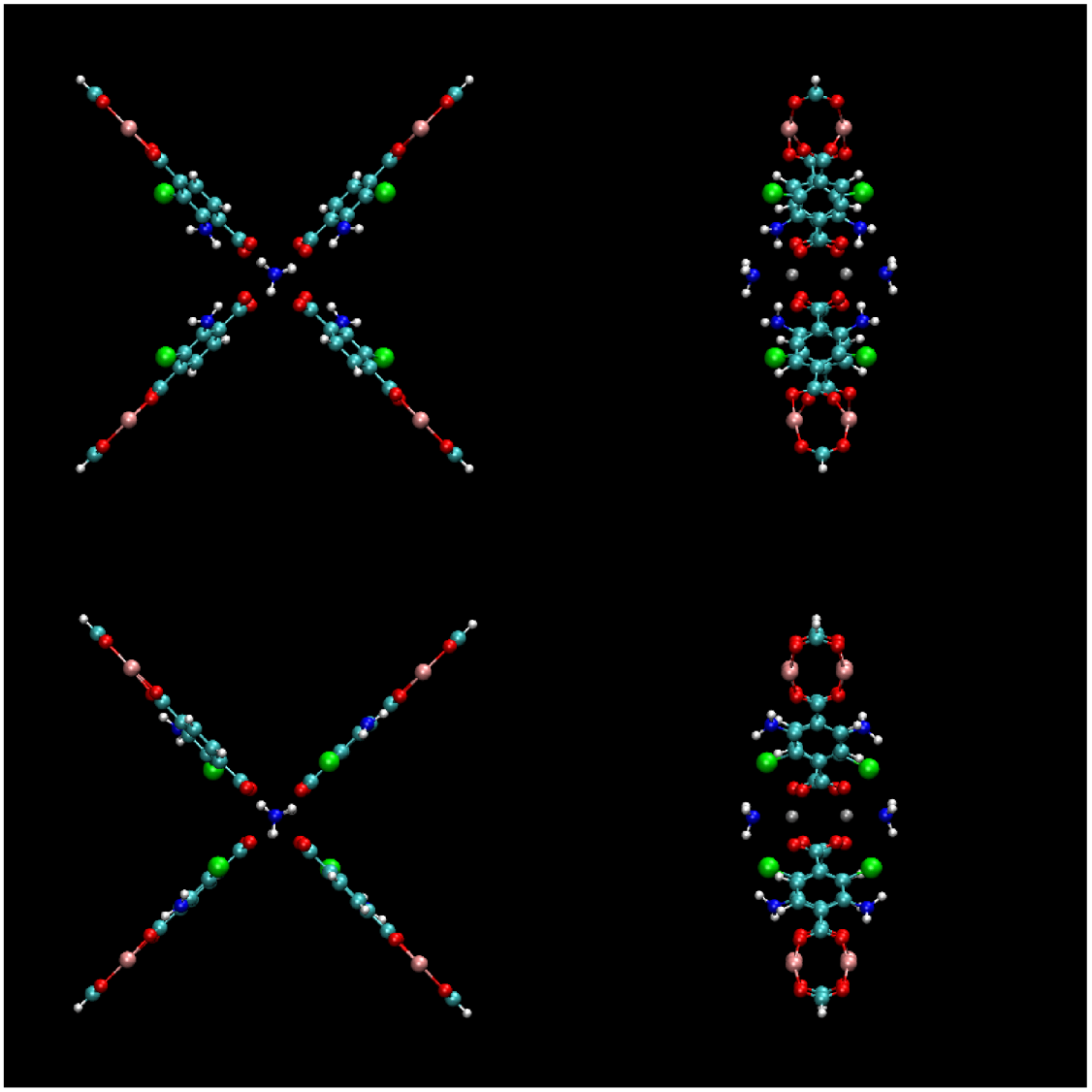

Figure 4.19 – Optimized geometries of cross configurations 4.17c (top) and 4.17d (bottom).

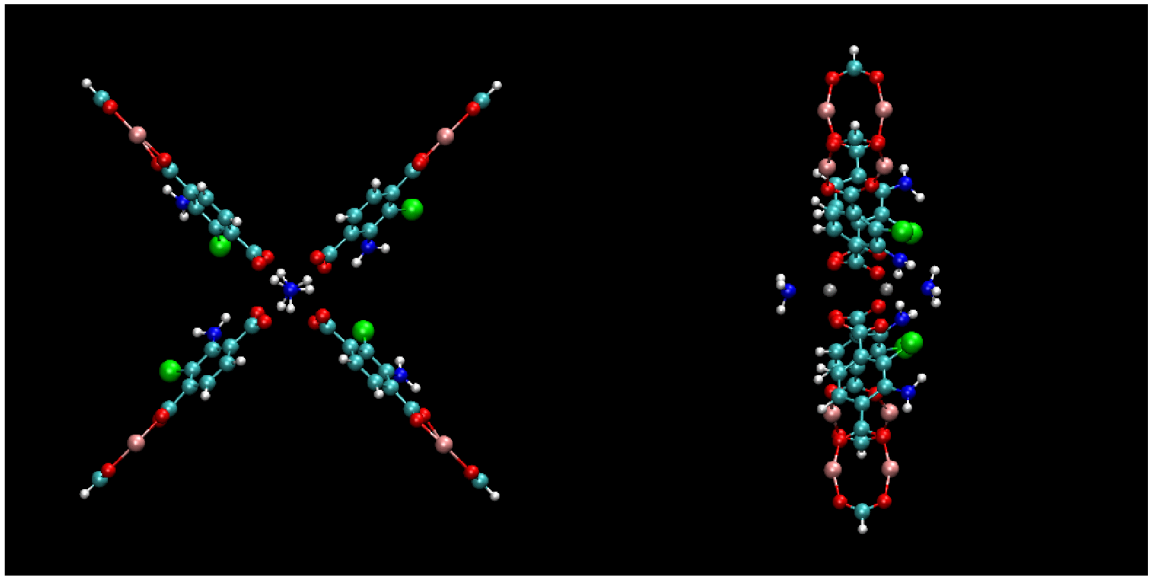

Figure 4.20 – Optimized geometry of cross configuration 4.17e.

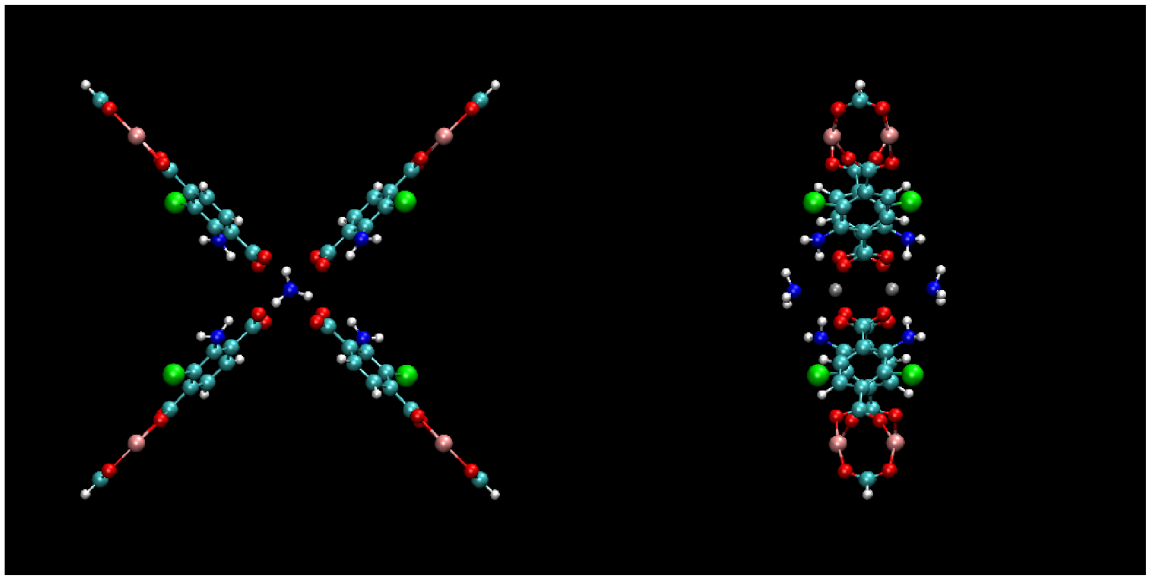

Figure 4.21 – Optimized geometry of cross configuration 4.17f.

Table 4.5 – Relative average energies of cross configuration pairs.
The relative energy was calculated by subtracting the lowest average cross configuration energy from each cross configuration energy values.

Cross configuration pair	Relative Energy (kcal/mol)
4.17a and 4.17b	1.797
4.17c and 4.17d	1.291
4.17e (and 4.17e)	0.646
4.17f (and 4.17f)	0.000

Though the optimized cross structures show little differences in energetics amongst the different ligand distributions, the energy calculations and optimizations utilized examined only a series of static states, and not the dynamics of the pore closing. Thus, the energetics of pore closing from square to rhombohedral configuration was studied. A cross system representing a rhombohedral cell was generated based on the geometry of the X-ray data[154] of the para-DMOF system. A square cross system was generated similarly from the ortho-DMOF X-ray data. The square and rhombohedral system coordinates were aligned such that the only changing coordinates were those of the atoms involved in the Zn-O-O-Zn dihedral change and the resultant BDC rotation. Nine intermediate cross configurations were generated for both the ortho- and para-DMOF systems, by linearly transforming the atomic coordinates of the rhombohedral cross system into the coordinates of the square cross system over the course of 10 steps. These eleven cross configurations form a simple model for the pore closing for each DMOF system. Single-point DFT energy calculations were used to establish an energy profile for the pore closing as a function of the changing Zn-O-O-Zn angle. This process was carried out for the six high-symmetry BDC ligand orientation distributions. The eleven configurations corresponding to the pore closing of the Figure 4.17a cross configuration can be seen in Appendix B. Since cross configuration pairs are needed to fully describe the framework, the average energies of the pore for those cross configuration pairs were plotted versus the Zn-O-O-Zn dihedral angle in Figures 4.22 – 4.25 for both the ortho- and para-DMOF frameworks. It can be seen from these figures that the pore closing has different energy profiles for different ligand orientation distributions. A promising sign is that in most of the configurations, there is a clear

difference in the energetics between the ortho- and para-DMOF frameworks. These are the first results of this investigation to yield a significant difference in energetics, with a difference in the energy barrier of almost 30 kcal/mol for the Figure 4.17e cross system. A difference of that magnitude in the energetics could explain the difference in breathing behavior of the ortho- and para-DMOF systems.

At first glance, the magnitude of the energy barrier for the LP to NP transition, ~100 kcal/mol for each of the systems generated here, seems very large – perhaps too large to ever occur. However, it should be noted that each cross system corresponds to two unit cells, and contains two pore walls for four different pores. Thus, barrier could be considerably lowered by interactions with the molecules in four different pores, which is consistent with the need for external stimuli such as the adsorption of guest molecules. It is conceivable that the adsorption of gas molecules, in conjunction with thermal fluctuations, could overcome the barrier and allow for LP to NP transitions.

It can also be seen that the LP cross configuration is higher in energy than the NP configuration. This implies that the LP configuration of the ortho- or para-DMOF framework is a local minimum, and not the global minimum as was previously assumed. This result explains the difficulties seen in prior work within this group in using hybrid Grand Canonical Monte Carlo/Molecular Dynamics (GCMC/MD) simulations in the constant stress ensemble to study MOF breathing – once the framework enters the NP configuration, the MD step driving the volume changes has difficulty in crossing back to the LP configuration due to the height of the energy barrier (~150-180 kcal/mol in the cross systems studied here).

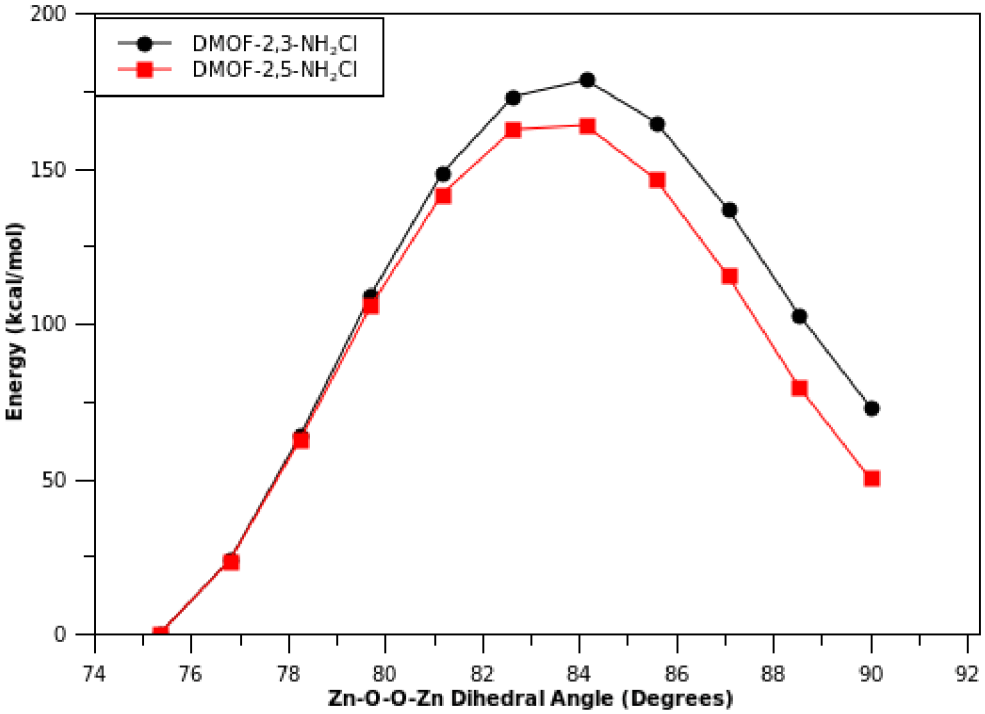

Figure 4.22 – Energy profile of pore closing for configurations 4.17a and 4.17b.

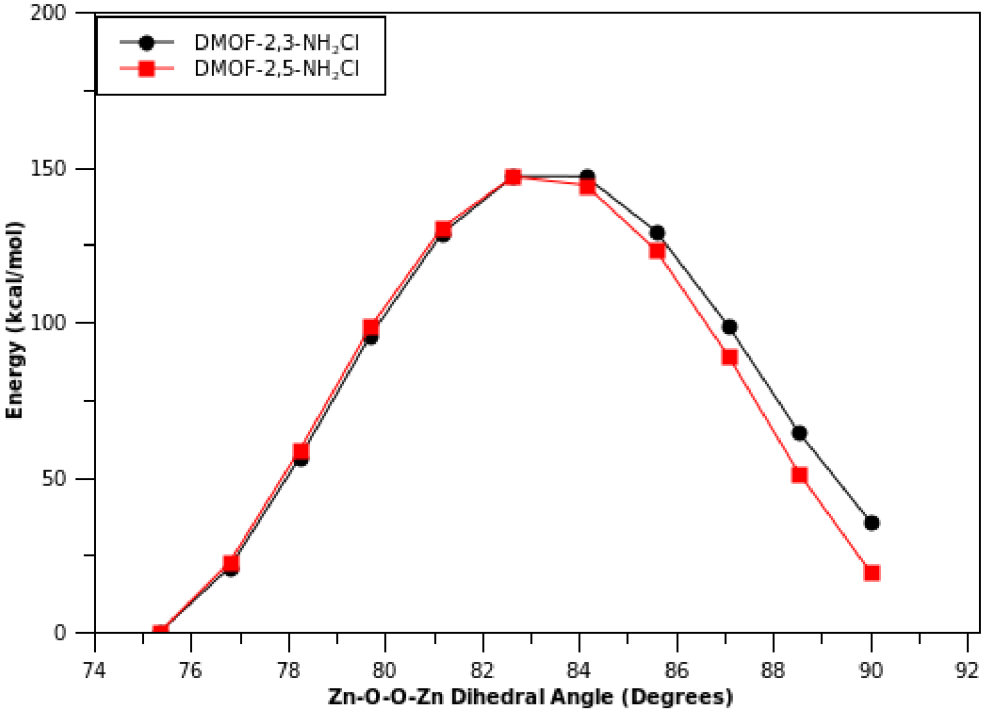

Figure 4.23 – Energy profile of pore closing for configurations 4.17c and 4.17d.

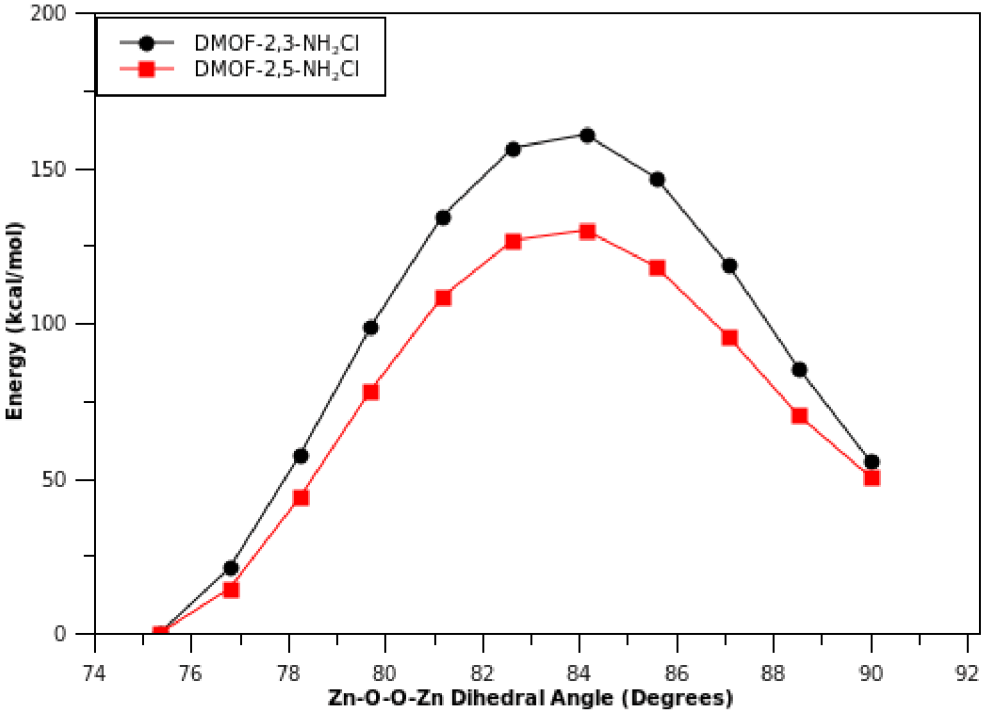

Figure 4.24 – Energy profile of pore closing for configurations 4.17e (and 4.17e).

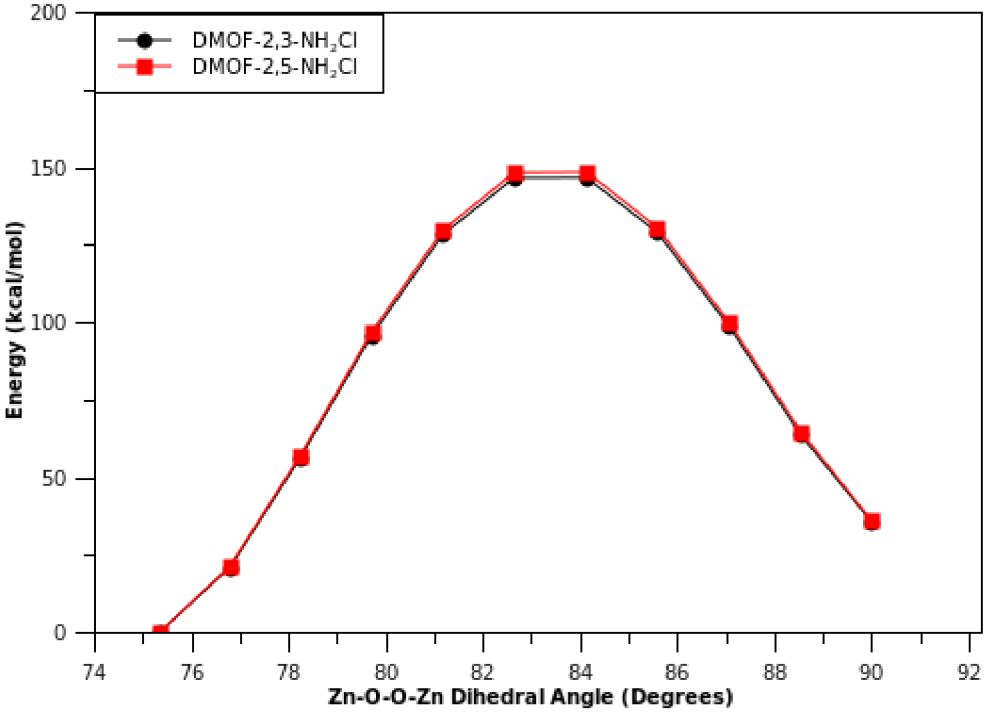

Figure 4.25 – Energy profile of pore closing for configurations 4.17f (and 4.17f).

The simulations of the pore closing of the cross simulations have yielded very interesting preliminary results concerning the energetics of pore closing during ortho- and para-DMOF breathing behavior. However, at this stage, there still is not enough information to definitively answer the question as to why there is a difference in breathing behavior between the two substituted DMOF frameworks. All prior work in the project pointed towards minimal differences in breathing behavior between the two isomeric frameworks during breathing behavior, independent of whether the effects examined were mediated by a nonframework guest molecule, the electronic structure of the framework, or the rotations of the substituted BDC ligands. In fact, the initial studies of the long-range effects of the different possible ligand orientation distributions showed no difference in internal energies of the different configurations. Had the pore closing calculations not shown any significant difference between the ortho- and para-DMOF frameworks, there might have been enough evidence to say that there is no difference between the two isomers, and that some experimental conditions were causing the observed difference. However, the differences in the energy profiles obtained when studying the pore closing only four of many possible ligand orientation distributions, which ranged from insignificant (0.019 kcal/mol and 1.848 kcal/mol) to intermediate (14.641 kcal.mol) to high (30.852 kcal/mol), indicates that the distribution of ligand orientation in the framework is indeed a property that requires more study.

While time constraints did not allow the progression of this project beyond this stage, much future work exists that can work toward determining definitively the cause behind the difference in ortho- and para-DMOF framework N_2 gas adsorption at 77 K. Of greatest importance is the obtaining of higher accuracy in the pore closing energy

profiles. While the mechanism of pore closing as currently studied is a reasonable approximation of the process, the intermediate stages between the cubic and rhombohedral configurations do not necessarily reflect the actual intermediate configurations, since a linear interpolation was used. To add in higher-order accuracy, calculating the optimized geometry of each intermediate step, using the current configuration as a starting guess, and then generating those energy profiles, would yield more accurate energy profiles that could confirm the veracity of the pore closing study done. This work was actually already begun, but is incomplete as of the time of this writing, due to difficulties in converging the self-consistent wavefunction during the calculations. After improving the accuracy, it would be necessary as well to obtain the pore closing mechanisms of the remaining possible combinations of ortho- and para-BDC ligand orientation distributions, to generate the possible energies that exist. Once the energy profiles exist, MD simulations of the configurations with the greatest differences between the ortho- and para- system could be run to see whether or not a difference in the pore volume and shape is observed with different amounts of MD loading. Furthermore, GCMC simulations of N_2 adsorption could be carried out on those systems and compared to GCMC simulations of frameworks with randomly-distributed BDC ligand orientations. It should be noted, though, that hybrid GCMC/MD simulations might not be a good idea due to the difficulty the MD step would have in sampling the PES, particularly in the NP to LP direction. These calculations and simulations could examine the effects of the ligand orientation distribution, and thus lead to additional understanding in the behavior and properties of MOFs.

In conclusion, the frameworks DMOF-2,3-NH_2Cl and DMOF-2,5-NH_2Cl were studied to determine the cause of the dramatic difference in N_2 gas adsorption observed at 77 K despite the extremely high similarity of the two frameworks. While initial MD simulations of the framework and DFT calculations of various framework fragments seemed to indicate little to no difference between the two systems, DFT calculations utilized to study pore closing of cross-shaped representative clusters with different distributions of the 2,3-NH_2Cl-BDC and 2,5-NH_2Cl-BDC ligands show differences in the energy profiles of closing. While the results of this study are merely preliminary, they are particularly compelling as it has always been taken for granted that ligand orientation distribution in MOFs is random. However, if this is not the case, this would change our understanding of MOFs, as such a high amount of self-assembled order could be extremely useful in different applications, and learning to direct the ordering would open new pathways for synthesizing reusable catalysts or proton-conduction membranes. Furthermore, the results underscore the importance of understanding the synthesis, nucleation, and crystal growth mechanisms of metal-organic frameworks, which are currently topics that are still largely unsolved. These results point in a logical direction to follow that would lead to an improved understanding of MOF behavior and properties that could potentially lead to new methods properties to exploit in emerging technologies such as proton-conducting membranes, chemical sensors, molecular switches, and carbon separation membranes.

5. Proton Conduction in HKUST-1

The framework HKUST-1 was originally synthesized in 1999 by Chui and co-workers at the Hong Kong University of Science and Technology. HKUST-1 has the unit cell $[Cu_3(TMA)_2(H_2O)_3]$, where TMA is benzene-1,3,5-tricarboxylate. Structurally, Cu dimers are tetracoordinated to TMA molecules to form the paddlewheel motif. The Cu coordination sphere is completed with an axial H_2O molecule, forming square pyramidal coordination polyhedral for each Cu centers. This forms intersecting 3D pores of 9×9 Å in the [100] direction and hexagonal shaped windows of size 18.6 Å in the [111] direction. The structure of HKUST-1 is shown in Figures 5.1 – 5.2. TGA and gas sorption measurements show thermal stability up to 240 °C and a BET surface area of 692.2 m^2/g, respectively. Additionally, after synthesis, the pores contained up to 10 additional water molecules per unit cell. The free and coordinated H_2O molecules could be removed by heating without loss of porosity in the framework.[159]

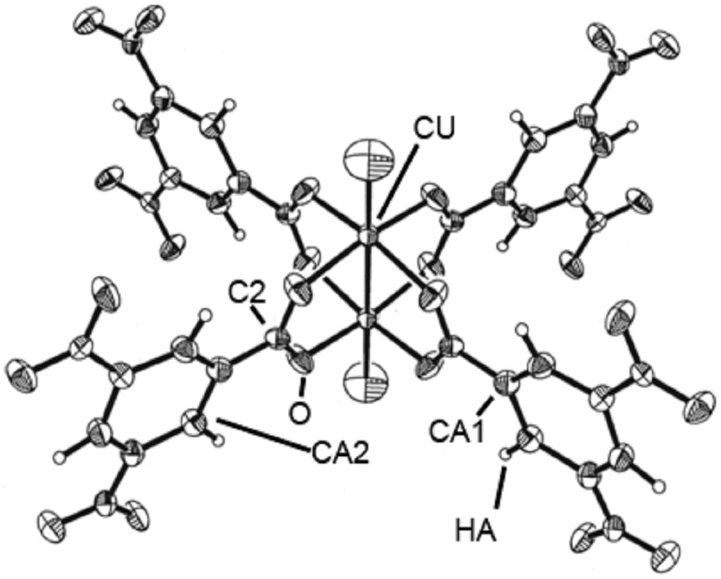

Figure 5.1 – Copper paddlewheel structure of HKUST-1 with complexed TMA molecules. HKUST-1 atom types for the Schmid force field are denoted. This figure is adapted Ref. 159.

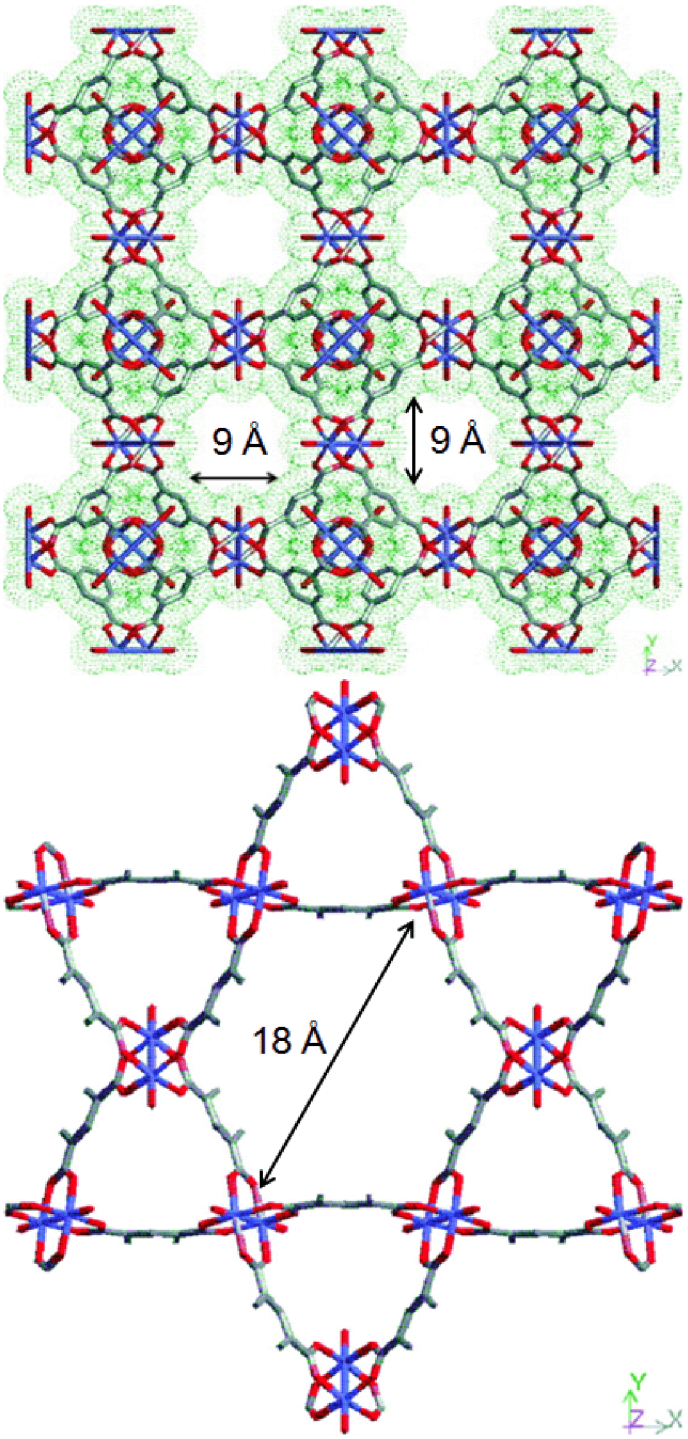

Figure 5.2 – 2D projections of HKUST-1. Top: HKUST-1 in the [100] direction. Bottom: HKUST-1 in the [111] direction. These two figures are adapted from Ref. 159. Blue = Cu, red = O, green (top) or gray (bottom) = C.

Recently, Jeong, et. al. exploited the increase in acidity of the molecules complexed to the open-metal site of HKUST-1 to promote proton conduction through the MOF channels. In order to accomplish this, HKUST-1 was first synthesized and then activated by heating to remove the H_2O molecules. Subsequently, the framework was submerged in a bath of solvent to be complexed to the open metal site. Water, ethanol, and acetonitrile were used to give a range of molecules with different proton acidity. These systems were referred to as HK-H_2O, HK-EtOH, and HK-MeCN, respectively. The systems were exposed to methanol vapor, and then the conductivity measured at room temperature. Both HK-MeCN and HK-EtOH had a proton conduction of approximately 0.2 μS/cm, and HK-H_2O 15 μS/cm. While the low HK-MeCN proton conductivity was expected due to the lack of acidic proton on acetonitrile, the HK-EtOH proton conductivity was surprisingly low compared to that of HK-H_2O, considering it has an acidic proton available for donation. However, the cause of this phenomenon appears to be the relative acidity of the complexed molecule relative to that of the charge-carrying solvent. The pKa of water is greater than the pKa of methanol, while the reverse is true for ethanol. To test this explanation, the proton conductivity of HK-MeOH was measured; a value of 0.43 μS/cm, slightly more than twice that of HK-EtOH, was obtained.[53]

The experiments of Jeong and co-workers are interesting as they represent a novel method for promoting proton conduction in easily-synthesized MOFs. However, while the proton conductivity measurements successfully describe the procedure from a macroscopic perspective, gaining a molecular level understanding of this proton conduction could lead to principles for designing frameworks with appropriate charge-

carrying solvents that take maximum advantage of the open metal sites and successfully promote proton conduction.

Prior simulations of proton conduction in bulk liquids such as water[160] and imidazole[161] have been carried out using the multi-state empirical valence bond (MS-EVB) method. The MS-EVB method[160] is an MD-based method that provides long-timescale deterministic trajectories that yield insight into the proton conduction. First, the proton-conduction system with one excess proton is partitioned into multiple diabatic EVB states that correspond to possible states containing both solvent molecules and the transporting proton. The ground state of the proton is described as a linear combination of these EVB states. During each MD step, the EVB states that contribute the most to the ground state energy of the system are located. These states are utilized to generate a ground state wavefunction an EVB Hamiltonian. The ground state is then determined variationally, and used to propagate the dynamics using the Hellmann-Feynman force each step.[161]

While HKUST-1 is not stable in water[60], Chui, et. al found up to 10 free water molecules per unit cell in the framework upon synthesis.[159] Though this system is undoubtedly not a strong contender as a possible proton conduction membrane for fuel cells, simulation of proton conduction in HKUST-1 with up to 10 water molecules per unit cell could test the explanation of the low MeOH in HK-EtOH proton conductivity in an independent fashion from Jeong's proton conductivity measurement of the proton conductivity of MeOH in HK-MeOH – if the explanation is correct, then the proton conductivity of the H_2O in HK-H_2O should be low, and the proton conductivity of EtOH in HK-H_2O lower still. Furthermore, by studying the distribution of water in the

HKUST-1 pores, a molecular-level understanding of the distribution of solvent molecules inside the framework could be gained. An MS-EVB parameterization has already been carried out in this group using the anharmonic single point charge flexible water model (aSPC/Fw), allowing for the setup of the HKUST-1 simulations. To set up this system, coordinating water molecules and one coordinated hydroxide would be added to the framework. The proton from the hydroxide would be placed in the pore as the excess proton for the EVB process.

The FIQCEN crystal structure[159] of HKUST-1 with coordinated water molecules was obtained from the Cambridge Structural Database (CSD).[162] A search of the literature for prior parameterization of an HKUST-1 force field led to the MM3-type force field of Tafipolsky, Amirjalayer, and Schmid for describing the framework with open metal sites.[163] The Schmid force field utilized the MM3 bond stretching, angle bending, torsion, inversion, and stretch-bend cross-terms, as well as a stretch-stretch cross-term and an "improved Fourier angle-bending" term from the SHAPES[97] square planar transition metal complex force field for modeling the dual minima of the Copper-Oxygen interactions at the metal clusters. It was developed using MM3 parameters as a starting guess for a genetic algorithm optimization,[164-165] and its usage in MD simulations of the paddlewheel successfully captured the normal mode frequencies while NPT simulations of the full system in the temperature range of 200 – 500 K successfully qualitatively reproduced the experimentally-observed negative thermal expansion (NTE) behavior of HKUST-1. Furthermore, its usage in computing the IR spectrum matched with experiments.[163]

Due to the success in predicting the HKUST-1 IR spectrum and NTE behavior, the Schmid force field was adapted for use with the DL_POLY 2[147] and DL_EVB[166] codes. However, some minor differences exist in the adaptation, as the Schmid force field was built using the Tinker molecular mechanics package[167], and not DL_POLY. Quartic and Morse bond stretching potentials and torsion interactions were modeled identically to Schmid's implementation. The stretch-stretch and stretch-bend cross-terms were modeled together as the COMPASS all-terms interaction available in DL_POLY. Valence angle bending was modeled with quartic instead of sextic potentials, as DL_POLY does not natively have support for sextic potentials, and the fifth- and sixth-order angle coefficients were small. Due to differences in implementation between DL_POLY and Tinker, the Tinker algorithm for out-of-plane bending energy was implemented into DL_POLY. The SHAPES interaction was also implemented into DL_POLY. As with the Schmid implementation, atomic partial charges were assigned to the atoms types instead of using MM3 bond dipoles, and interactions between 1,4-connected atoms scaled by a factor of 0.5. The HKUST-1 force field can be seen below in Tables 5.1–5.6.

Table 5.1 – HKUST-1 force field atom types, atomic charges, and vdW parameters
Though the vdW parameters are given here in terms of Lennard-Jones parameters, all vdW interactions for the framework were modeled using the Buckingham potential. The conversion of these parameters into the Buckingham parameters can be found in Chapter 2.

Atom Type	Charge	ε (kcal/mol)	σ (Å)
C	1.20	0.296	2.013
Ca1	0.00	0.056	1.746
Ca2	-0.12	0.056	1.746
O	-0.64	0.059	1.621
C2	0.68	0.056	1.728
Ha	0.12	0.020	1.443

Table 5.2 – HKUST-1 force field bond stretch parameters.
Top: Morse potentials. Bottom: Quartic potentials.

Bond	E_0 (kcal/mol)	k (Å^{-1})	r_0 (Å)
Cu–O	7.309	2.500	1.976

Bond	k_1 (kcal/mol A^{-2})	k_2 (kcal/mol A^{-3})	k_3 (kcal/mol A^{-4})	r_0 (Å)
Cu-Cu	35.97	-137.6	272.9	2.656
Ca1-Ca2	943.9	-3610.2	7160.3	1.380
Ca1-C2	639.5	-2446.3	4851.8	1.503
Ca2-Ha	741.0	-2834.3	5621.3	1.101
O-C2	139.7	-5343.8	1059.9	1.262

Table 5.3 – HKUST-1 force field angle bending parameters
Top: SHAPES improved Fourier potential. Bottom: Quartic potentials.

Angle	k (kcal/mol)	θ_0 (Degrees)
O–Cu–O	31.65	0, 90

Angle	k_1 (kcal/mol rad^{-2})	k_2 (kcal/mol rad^{-3})	k_3 (kcal/mol rad^{-4})	θ_0 (Degrees)
Cu-O-C2	37.41	-45.01	13.75	118.71
Ca1-Ca2-Ca1	109.3	-131.6	40.20	121.70
Ca1-Ca2-HA	70.50	-84.83	25.92	120.00
Ca1-C2-O	143.7	-172.9	52.85	117.52
Ca2-Ca1-C2	104.0	-125.2	38.25	115.31
Ca2-Ca1-Ca2	109.3	-131.6	40.20	121.70
O-C2-O	231.6	-278.7	85.17	126.84

Table 5.4 – HKUST-1 force field out-of-plane bending parameters

Inversion Angle	k (kcal/mol rad^{-2})	χ_0 (Degrees)
Ca1-Ca2-Ca1-Ha	28.78	0
Ca1-C2-O-O	188.9	0
Ca2-Ca1-C2-Ca2	28.78	0
O-C2-Ca1-O	188.9	0
C2-Ca1-Ca2-Ca2	28.78	0
Ha-Ca2-Ca1-Ca1	15.83	0

Table 5.5 – HKUST-1 stretch-stretch and stretch-bend cross-term parameters
Reference bond lengths and angles are taken from the bond stretch and angle bend parameters.

Angle	k_{ss} (kcal/mol Å^{-2})	k_{sb1} (kcal/mol rad^{-1})	k_{sb2} (kcal/mol rad^{-1})
Cu-O-C2	15.83	21.15	3.741
Ca1-Ca2-Ca1	76.33	17.84	17.84
Ca1-Ca2-Ha	0.000	11.51	11.51
Ca1-C2-O	43.16	71.94	57.55
Ca2-Ca1-C2	21.08	50.79	13.24
Ca2-Ca1-Ca2	76.33	17.84	17.84
O-Cu-O	15.83	0.000	0.000
O-C2-O	105.1	68.92	68.92

Table 5.6 – HKUST-1 torsion parameters
An electrostatic scaling parameter of 0.5 and vdW scaling parameter of 1.0 was used.

Dihedral	V (kcal/mol)	ω_0 (Degree)	n
Cu-O-C2-O	3.3100	180.0	2
Ca1-Ca2-Ca1-C2	2.9915	180.0	2
Ca1-Ca2-Ca1-Ca2	2.9915	180.0	2
Ca2-Ca1-C2-O	0.8750	180.0	2
Ca2-Ca1-Ca2-Ha	2.6925	180.0	2
C2-Ca1-Ca2-Ha	2.9915	180.0	2

To test the DL_POLY implementation of the Schmid force field, the activated (water-free) framework was allowed to equilibrate first in the NVT ensemble for 100 ps, and then in the NPT ensemble for another 100 ps, before the dynamics were studied through a 400 ps MD run in the NPT ensemble, at temperatures of 200 – 500 K. For all MD simulations, to match the conditions of Schmid and co-workers, the equations of motion were propagated using the velocity-Verlet algorithm, with a timestep of $\Delta t = 0.1$

fs, using the Berendsen thermostat and barostat, with relaxation times of 0.1 and 2.0 ps, respectively. The short range interaction radius cutoff was 11.0 Å; electrostatic interactions were treated using the particle mesh Ewald (PME) method.[104] The simulations were carried out using the DL_POLY 2.[147] A plot of the lattice constant of HKUST-1 against temperature can be seen in Figure 5.3. The coefficient of thermal expansion was found by linear regression to be $-1.41\times10^{-5}\ \mathrm{K}^{-1}$, which is of the same order of magnitude as from the experimental work of Wu $\left(-1.07\times10^{-5}\ \mathrm{K}^{-1}\right)$[168] and the simulations of Schmid $\left(-1.06\times10^{-5}\ \mathrm{K}^{-1}\right)$.[163]

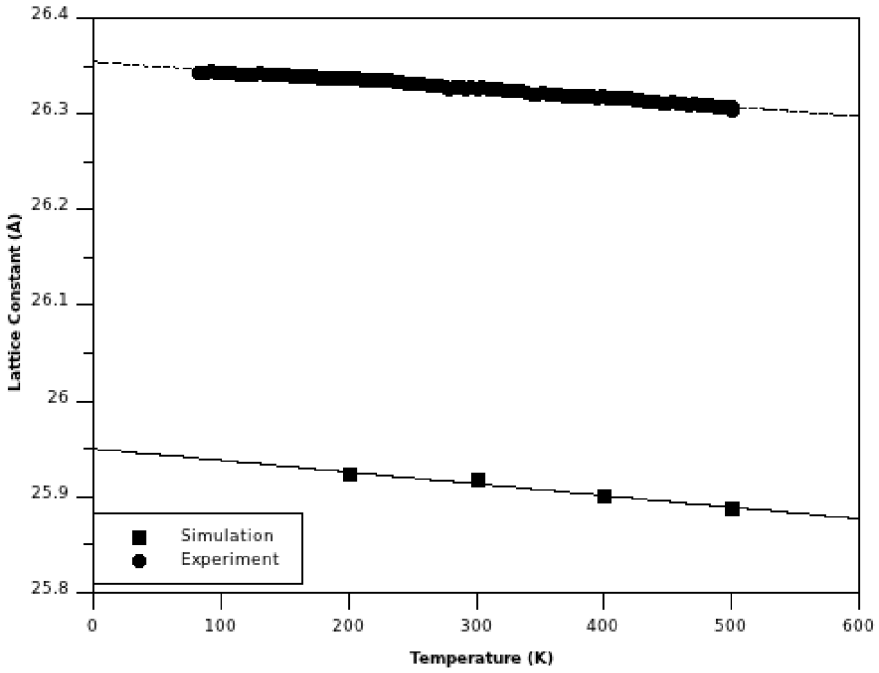

Figure 5.3 – Negative Thermal Expansion (NTE) behavior of HKUST-1. Experimental data from the synchrotron powder X-ray diffraction measurements of Wu, et. al.[168]

The water model chosen to represent the water molecules during the molecular dynamics simulations was the aSPC/FW water model due to its success in describing the

solvation structure around an excess proton when applied to studies of proton transport, and also correctly predicts water at ambient temperatures, reproducing structural, thermodynamical, and dynamical properties.[112] The aSPC/FW water molecule force field parameters can be seen in Tables 5.7 and 5.8.

Table 5.7 – aSPC/FW atom types, charges, and vdW parameters
The mixed vdW interactions between water molecules and the framework were modeled using the Lennard-Jones potential, not the Buckingham potential.

Atom Type	Charge	ε (kcal/mol)	σ (Å)
Ow	-0.8350	0.1554	3.165
Hw	0.4175	0.0000	0.000

Table 5.8 – aSPC/FW bond stretching and angle bending parameters
Top: Bond stretching interactions. Bottom: Angle bending interactions

Bond	k_1 (kcal/mol A^{-2})	k_2 (kcal/mol A^{-3})	k_3 (kcal/mol A^{-4})	r_0 (Å)
Ow-Hw	1214	-4166	7410	0.9950

Angle	k (kcal/mol rad^{-2})	θ_0 (degree)
Hw-Ow-Hw	75.90	112.5

A literature search revealed no prior work that had modeled HKUST-1 with complexed water molecules. To parameterize the Cu-O bond interaction, a Cu paddlewheel unit was set up, consisting of the Cu dimer coordinated to 4 carboxylates. Each carboxylate was capped with a hydrogen atom. A single water molecule was placed collinear to the copper atoms, with the hydrogen atoms facing away from the paddlewheel, as found by Chui, et. al.[159] Configurations with Cu-O distances of 1.4 – 6.0 Å were generated, and their single-point DFT energies calculated. To match the quantum calculations of Schmid and co-workers[163], all DFT calculations utilized the B3LYP[87] functional. The aug-cc-VDZ[77] basis set was used for all atoms except Cu, for which the ECP of the aug-cc-pVDZ-PP[155] was used. The resultant profile (Figure 5.4), showed a

minimum at approximately 2.21 Å, which is close to the reported Cu-O distance of 2.165 Å as determined by Chui, et. al.

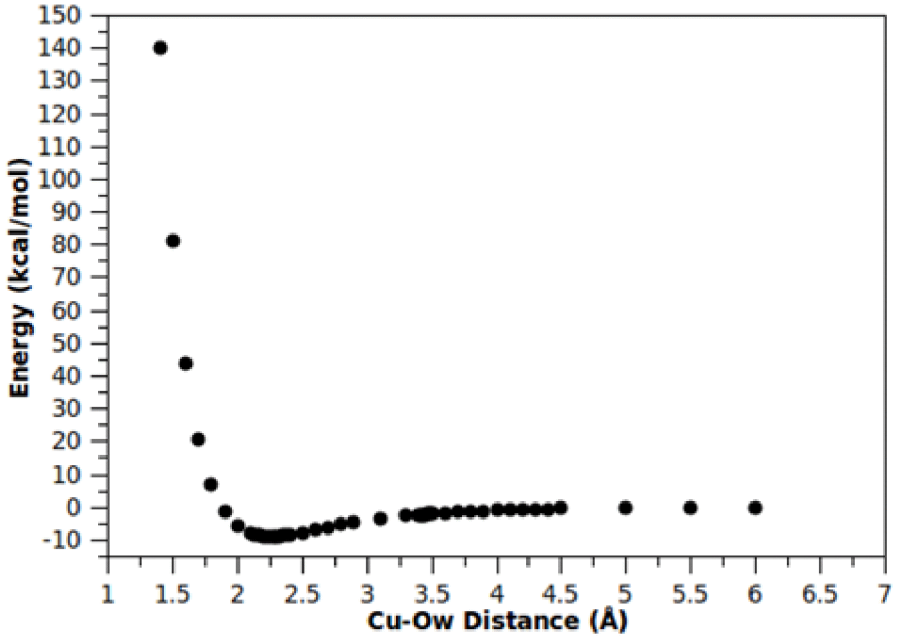

Figure 5.4 – *Ab initio* energy profile of the Cu-Of bond stretching interaction

Due to the nearly 9 kcal/mol well depth of the Cu-O interaction, a nonbonded representation of the coordinated water molecule would most likely lead to extremely unstable simulations; instead, parameterization of the water-framework interaction with bonded force field components is required. Since the complexed water molecules are no longer equivalent to free water within the framework, they have been assigned new atom types, Of and Hf, with identical parameters as free water molecule atom types Ow and Hw, but with the addition of the explicit framework-water interaction. This interaction was partitioned into four components: the Cu-Of bond, the Cu-Of-Hf angle, the O-Cu-Of angle, and the O-Cu-Of-Hf dihedral. To parameterize the angular interactions, the water molecule was placed at the equilibrium distance from the Cu, 2.21 Å, and DFT

calculations used to determine the energies of configurations with Cu-Of-Hf angles from 10° – 120° and with O-Cu-Of angles from 55° – 135°. The *ab initio* energy profiles for the Cu-Of-Hf and O-Cu-Of angle bending interactions can be seen in Figures 5.5 and 5.6, respectively.

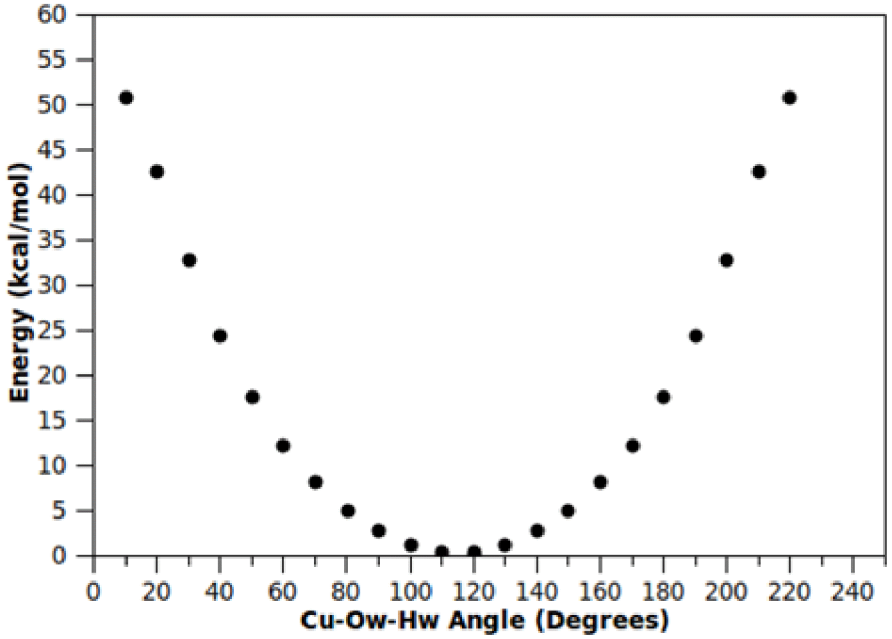

Figure 5.5 – *Ab initio* energy profile of the Cu-Of-Hf angle bending interaction.

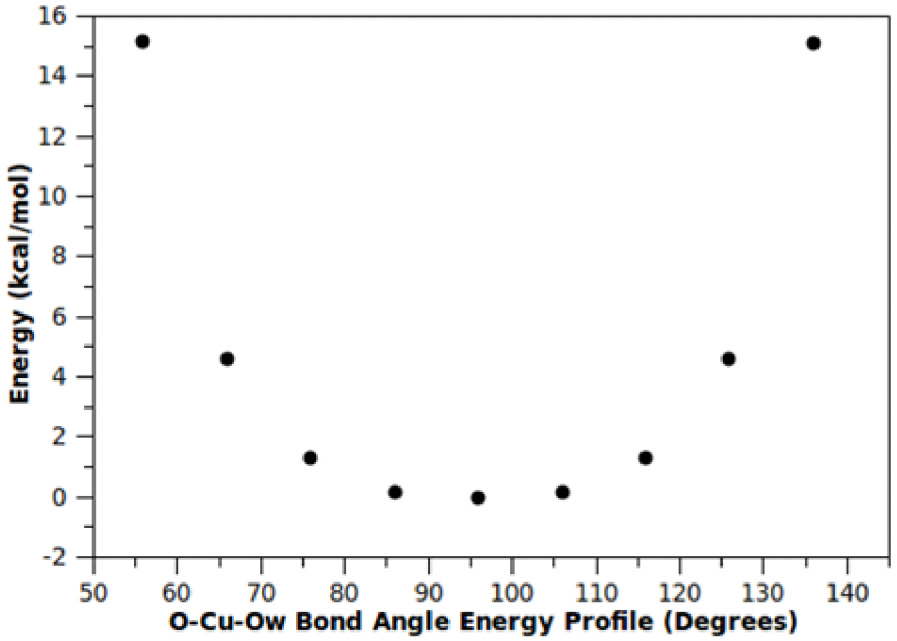

Figure 5.6 – *Ab initio* energy profile of the O-Cu-Of angle bending interaction.

The framework-water interaction energy profile is the difference between the *ab initio* energy profile and an energy profile calculated using the force field. Force field energies were calculated from 0 ps MD simulations in the NVE ensemble in DL_POLY 2.

To parameterize the Cu-O bond, the hydrogen atoms were modeled as Ca1 atoms from the full HKUST-1 system to balance charge, and a dummy Cu-O bond with strength of 0 kcal/mol was placed to remove the effects of nonbonded interactions. The water parameters were taken from the aSPC/FW water model. The difference between the *ab initio* and force field scans was fit to a Morse potential. The parameters for this Morse potential can be found in Table 5.10. The equilibrium distance of 2.1090 Å is close to the 2.165 Å Cu-O distance characterized by Chui, et. al.[159]

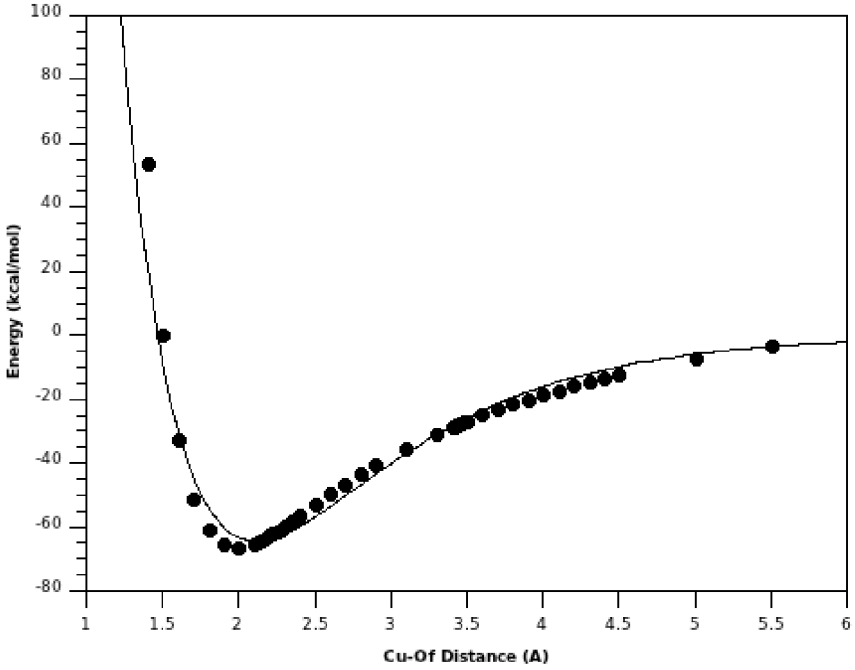

Figure 5.7 – Fitted Cu-Of Bond Stretching Potential

The Cu-Of-Hf angle was parameterized next in a similar fashion, with the newly-parameterized Cu-Of bond and a 0 kcal/mol dummy Cu-Of-Hf angle included during the scan. The difference between the *ab initio* and force field scans was fit to a harmonic potential. The parameters can be found in Table 5.10.

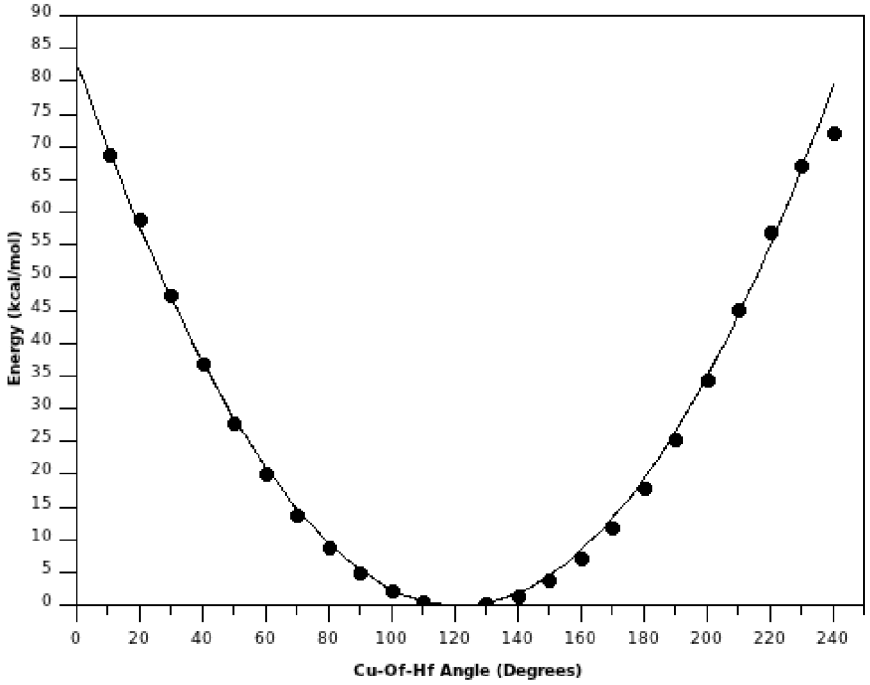

Figure 5.8 – Fitted Cu-Of-Hf Angle Bending Potential

The O-Cu-Of angle was also parameterized in this fashion, with recently-parameterized Cu-Of bond and Cu-Of-Hf angle interactions included in the scan. The parameters can be found in Table 5.10.

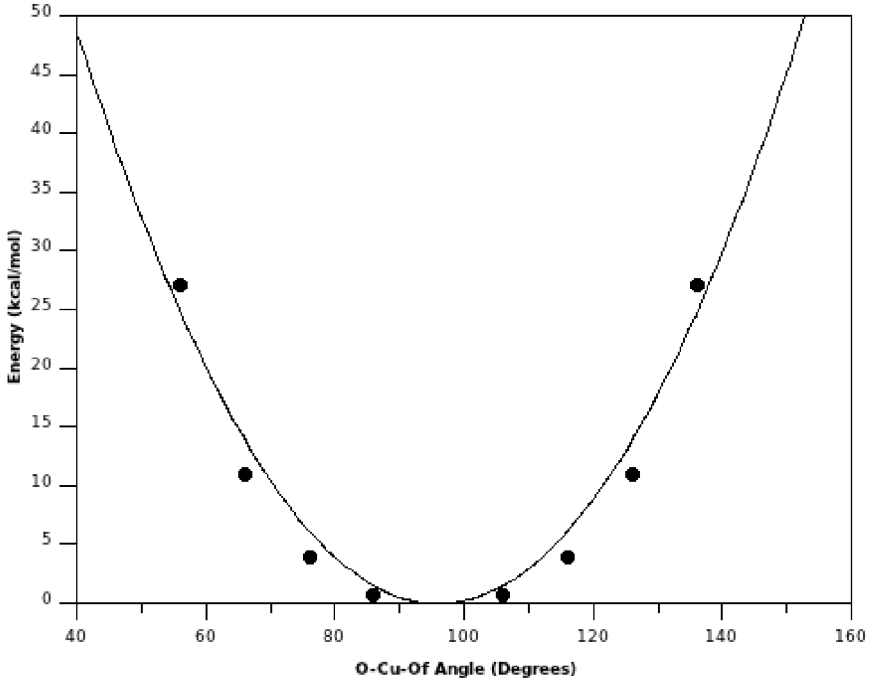

Figure 5.9 – Fitted O-Cu-Of Angle Bending Potential

0 kcal/mol dummy O-Cu-Of-Hf dihedrals were also included in the force field, as the bond stretch and angle bending terms already took into account the remaining water-framework interactions. After the parameterization of these three bonded interactions, a new water-coordinated HKUST-1 system was set up, with the water molecules and bonded interactions added. The water-framework force field parameters are summarized in Table 5.9 and 5.10.

Table 5.9 – New atom types and their corresponding aSPC/FW atom types
The complexed water molecules have the same force field parameters as the free water molecules.

New atom type	Corresponding old atom type
Of	Ow
Hf	Hw

Table 5.10 – Framework-water additional interactions for complexed water ligands
The dummy dihedral with V=0 kcal/mol was added to the force field to prevent double counting the interactions between the Hw and O atoms.

Bond	E_0 (kcal/mol)	k (Å^{-1})	r_0 (Å)
Cu–Of	64.0245	1.0726	2.1090

Angle	k (kcal/mol rad^{-2})	θ_0 (degree)
Cu-Of-Hf	37.0041	121.08
O-Cu-Of	102.1058	95.92

Dihedral	V (kcal/mol)	ω_0 (Degree)	n
O-Cu-Of-Hf	0.000	180.0	2

The water-filled framework was allowed to equilibrate first in the NVT ensemble for 20 ps. Afterwards, the dynamics were studied through a 1 ns MD run in the NPT ensemble, at a temperature of 300 K. The equations of motion were propagated using the velocity-Verlet algorithm, with a timestep of $\Delta t = 0.1$ fs, using the Berendsen thermostat and barostat, with relaxation times of 0.1 and 2.0 ps, respectively. The short range interaction radius cutoff was 11.0 Å; electrostatic interactions were treated using the particle mesh Ewald (PME) method. The simulations were carried out using the DL_POLY 2 and DL_EVB software.

Figures 5.10 – 5.21 show the radial distribution functions (RDFs) that describe the correlations between the oxygen atoms of the coordinated and free water molecules in the unactivated HKUST-1 framework, with 1, 2, 4, 6, 8, and 10 free water molecules per unit cell. Specifically, the Of-Ow (Figures 5.10 – 5.15) and Ow-Ow (Figures 5.16 – 5.21) correlation are examined. The simulations predict formation of hydrogen bonds between he coordinated and free water molecules for all loadings of free water, as evidenced by the sharp peak at ~2.8 Å in the Of-Ow RDFs. This is promising with regards to the veracity of the simulation, as the lack of a hydrogen bond between the complexed and

free water molecules would mean proton conduction through the Grotthuss mechanism as described by Jeong, et. al[53] would not be possible, and their experimental results obviously preclude this conclusion. The Ow-Ow RDFs likewise show hydrogen bonding amongst the free water molecules within the framework in their first peak at ~2.75 Å. While the RDFs systems with low loading (1-4 free H_2O per unit cell) show significant localization, with secondary and tertiary peaks at 8 and 11 Å corresponding to the free water molecules hydrogen bonded to the next-closest complexed water molecules, the systems with higher loading (6-10 free H_2O per unit cell) show a relatively continuous distribution of water molecules past the initial 2.8 Å peaks in both the Of-Ow and Ow-Ow RDFs, a distribution that is amenable to proton transport via the Grotthuss proton-hopping mechanism.

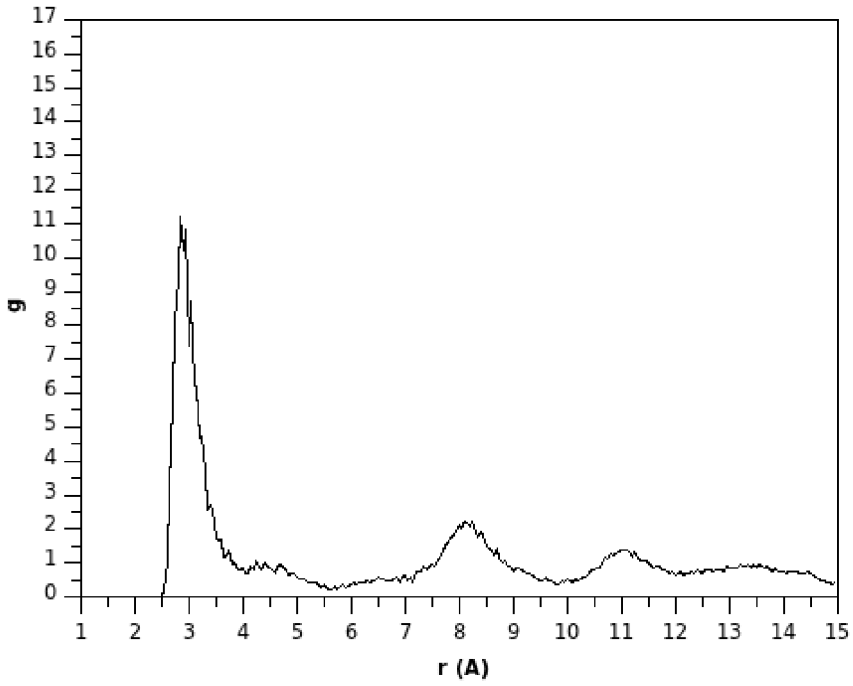

Figure 5.10 – Of-Ow radial distribution function for $N_{H_2O} = 1$

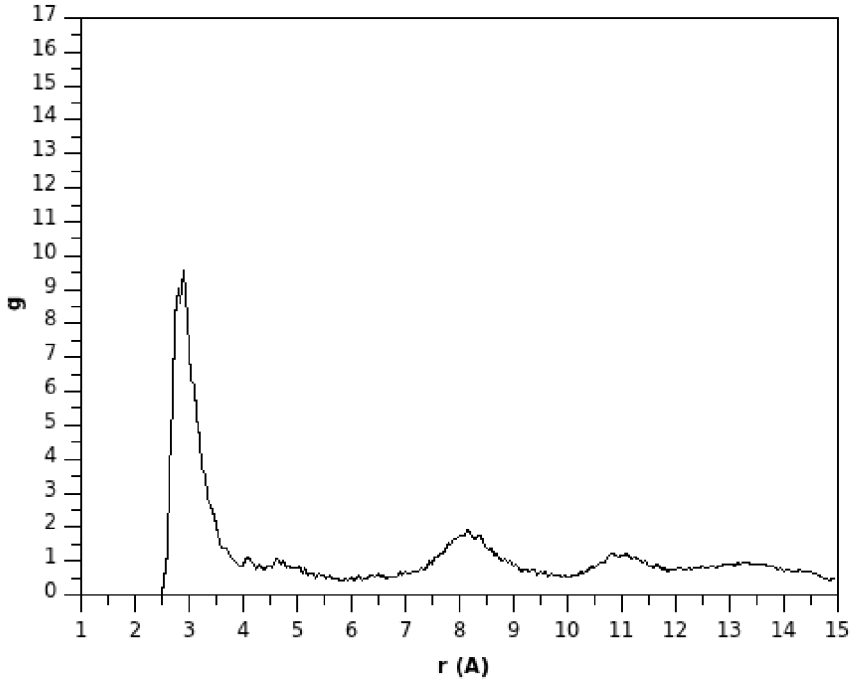

Figure 5.11 – Of-Ow radial distribution function for $N_{H_2O} = 2$

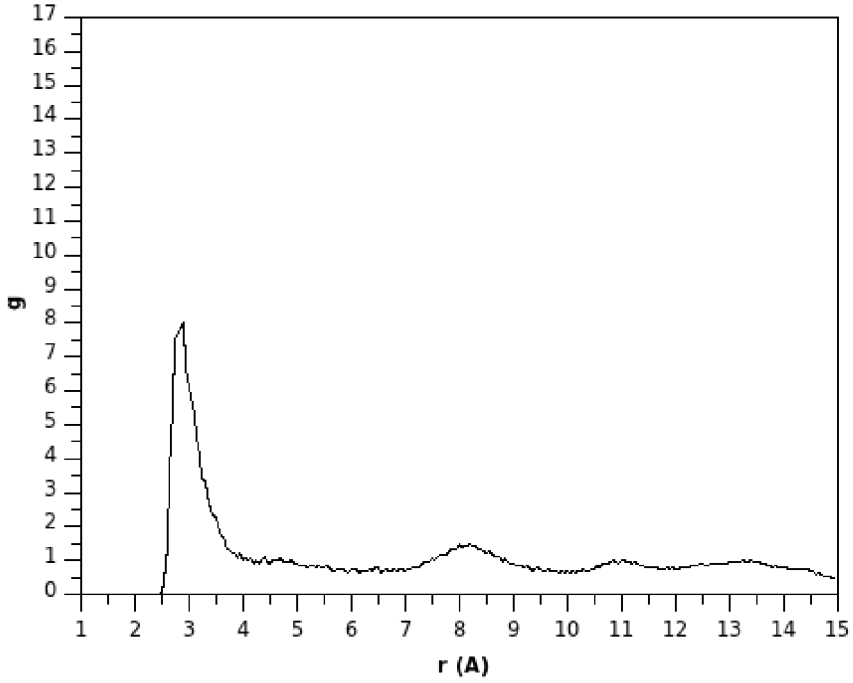

Figure 5.12 – Of-Ow radial distribution function for $N_{H_2O} = 4$

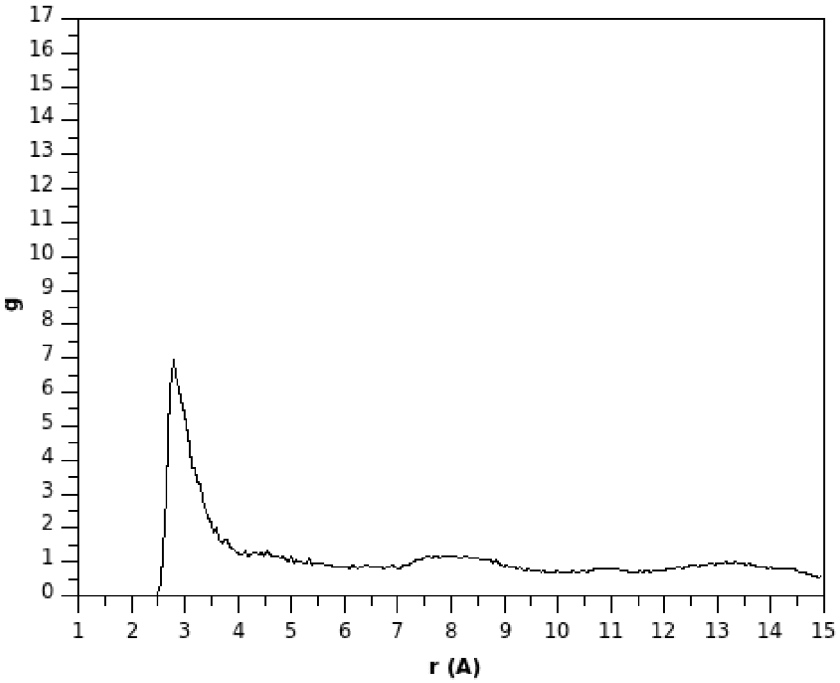

Figure 5.13 – Of-Ow radial distribution function for $N_{H_2O} = 6$

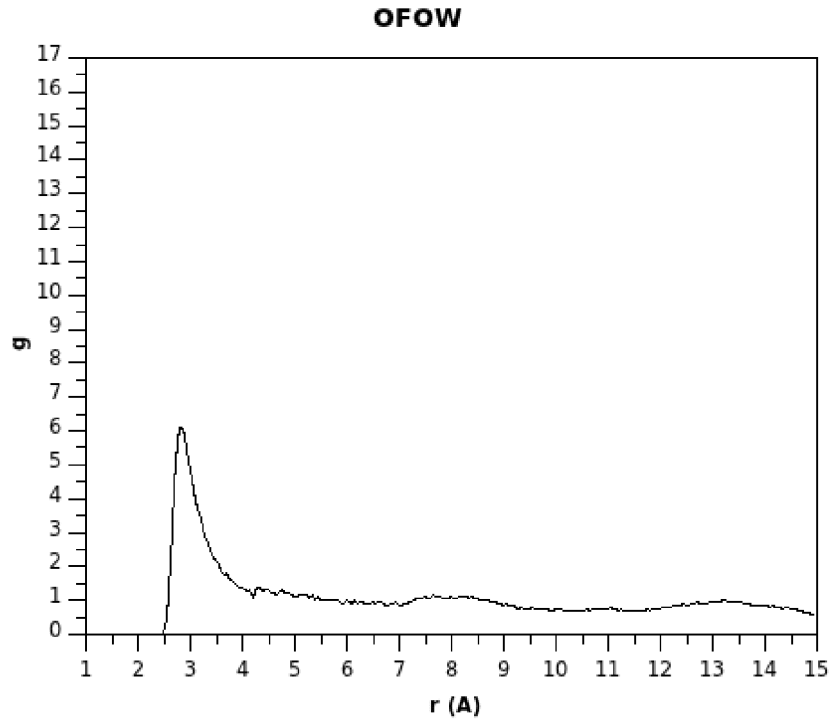

Figure 5.14 – Of-Ow radial distribution function for $N_{H_2O} = 8$

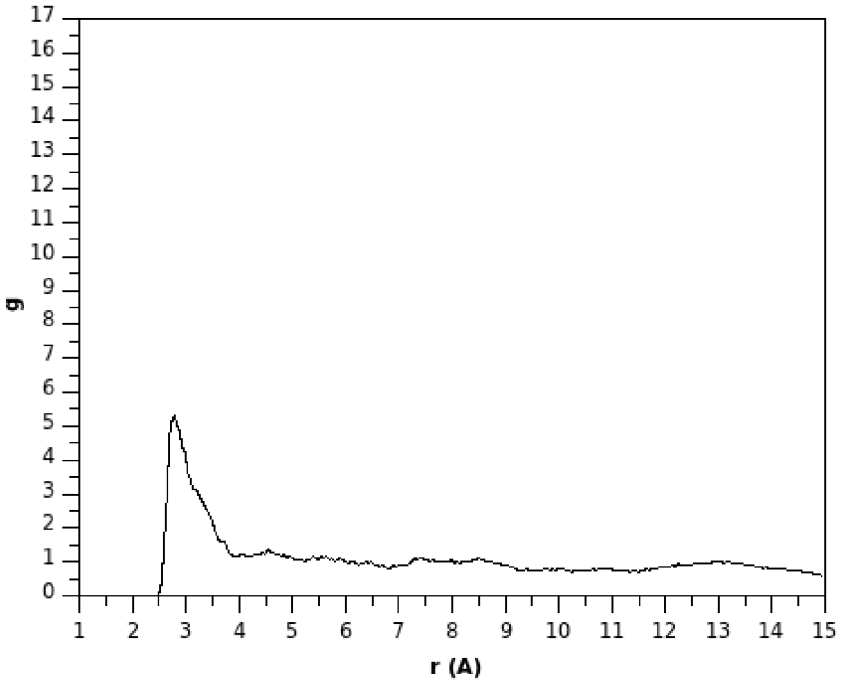

Figure 5.15 – Of-Ow radial distribution function for $N_{H_2O} = 10$

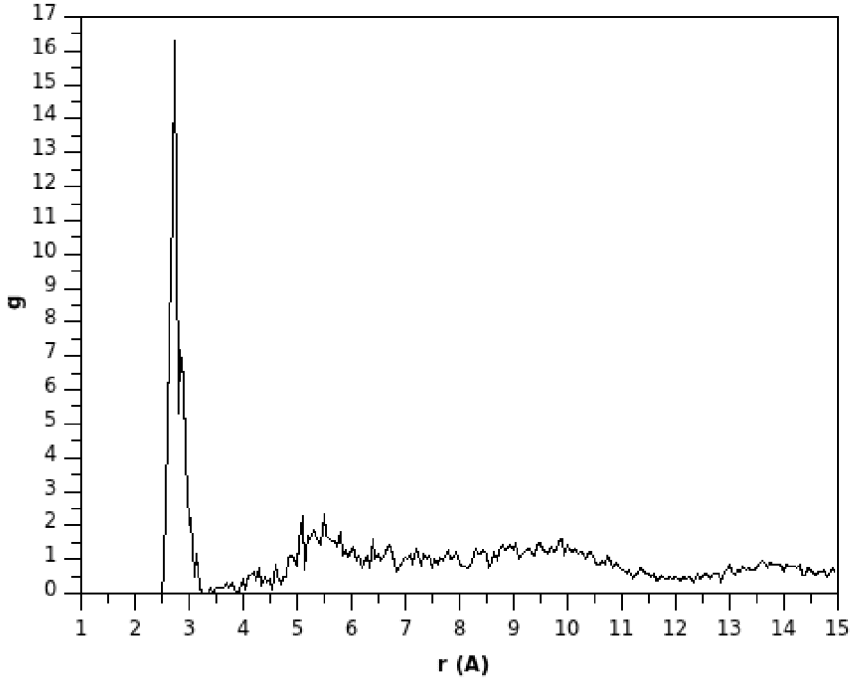

Figure 5.16 – Ow-Ow radial distribution function for $N_{H_2O} = 1$

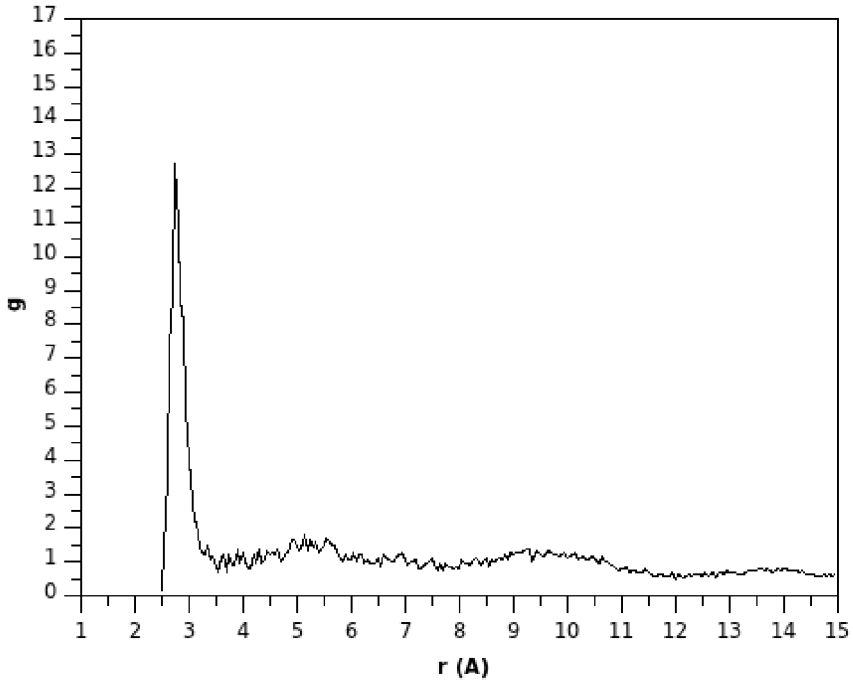

Figure 5.17 – Ow-Ow radial distribution function for $N_{H_2O} = 2$

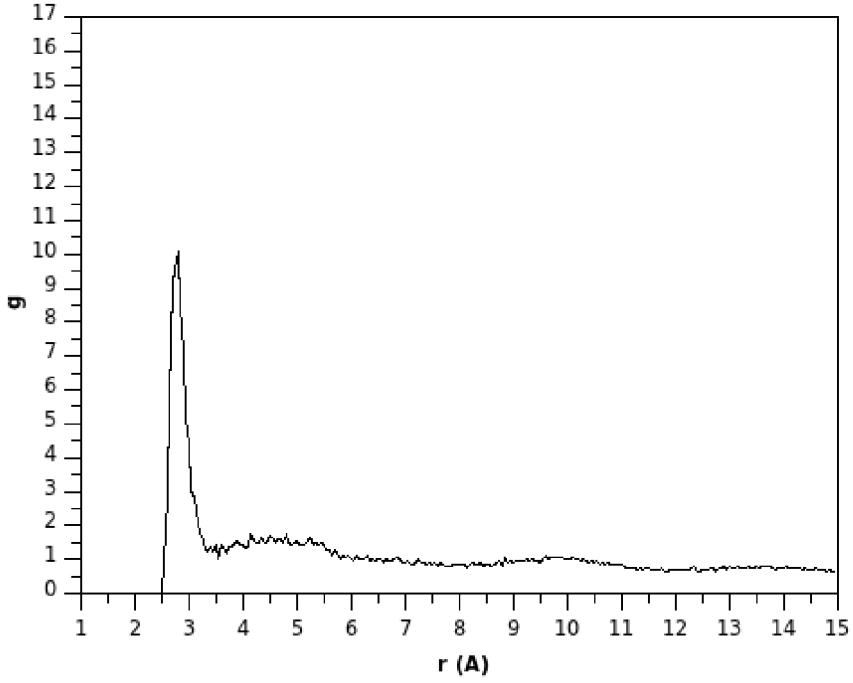

Figure 5.18 – Ow-Ow radial distribution function for $N_{H_2O} = 4$

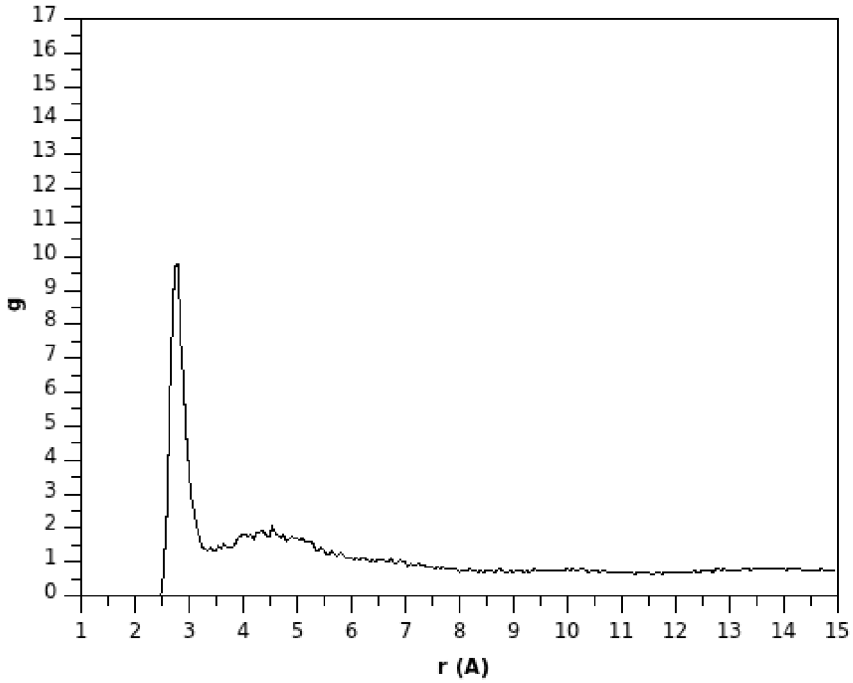

Figure 5.19 – Ow-Ow radial distribution function for $N_{H_2O} = 6$

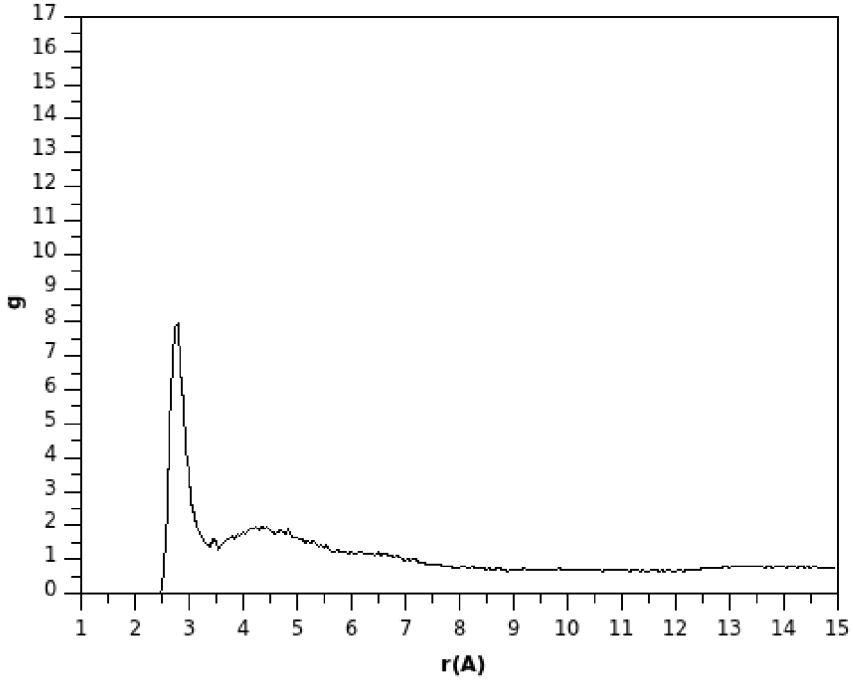

Figure 5.20 – Ow-Ow radial distribution function for $N_{H_2O} = 8$

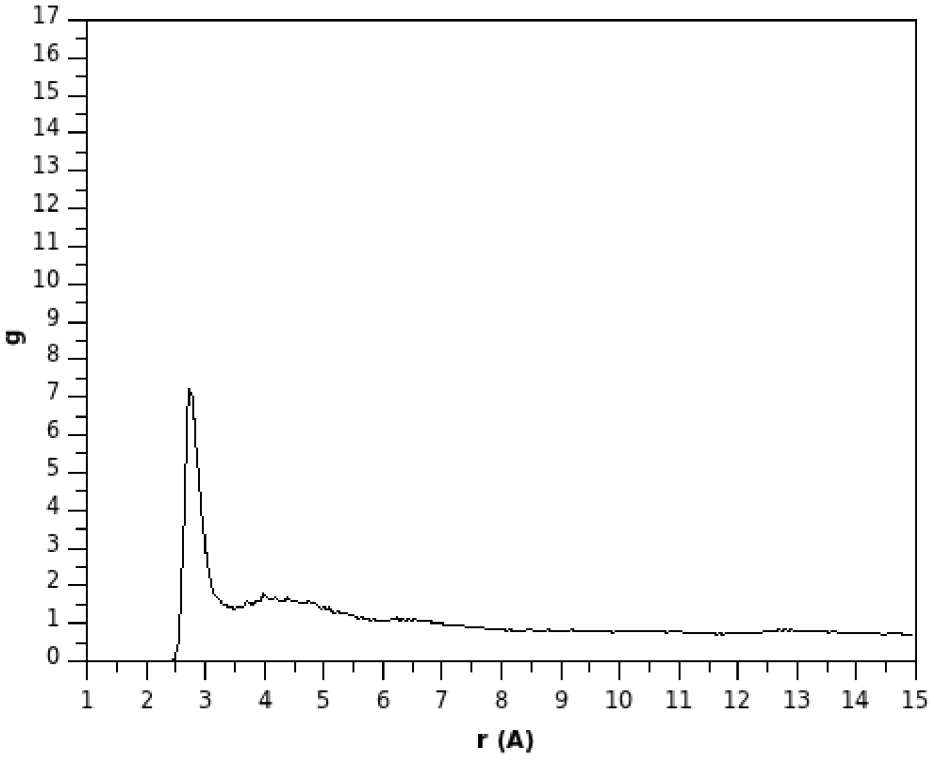

Figure 5.21 – Ow-Ow radial distribution function for $N_{H_2O} = 10$

The simulations of water in HK-H_2O are promising and show an environment that is conducive to proton transport via the Grotthuss mechanism. However, to study the charge transport properties of the HKUST-1 framework, actually simulating an excess proton through MS-EVB simulations is the next step. While time constraints did not allow the progression of this project past this early stage, there is significantly more work to be done for this project in the future, work which will lead to interesting insights concerning charge transport through MOF channels and their suitability for use in PEMFCs.

The next step is to utilize MS-EVB simulations of an excess proton from one of the coordinated H_2O molecules diffusing through the channel would show how

conductive the framework is in the ambient environment. This process has already been carried out for the aSPC/FW water model in this group and needs merely to be implemented.

Afterwards, one of the complexed water molecules would be changed to a hydroxide group, and the hydroxide-framework interaction could then be parameterized similarly by the method used to parameterize the complexed water-framework interaction. Then, proton conduction in the HK-H_2O could be simulated. The HK-H_2O would be set up, with one complexed water molecule replaced by a hydroxide. The dissociated proton would be placed into the pore with the water molecules, and the MS-EVB methodology utilized to study the proton conduction by examining the structure and dynamics of the water and proton in the pores.

Subsequently, the same methodology could be repeated to simulate the proton conduction in the HK-EtOH, HK-MEOH, and HK-MeCN systems. This study would investigate the effects of the molecule complexed to the open metal site over a range of acidities on the distribution of water in the framework pores and on the ability of the material to conduct protons. Even further in the future, MS-EVB models of other proton-conducting molecules such as methanol, ethanol, and imidazole could be developed, and the same studies applied to HKUST frameworks filled with those charge carrying solvents. These studies of different complexed molecules with different charge-carrying solvents in HKUST-1 would allow not only for a molecular level explanation of the results of Jeong and co-workers' results, but also an improved understanding of the facilitation of proton conduction in MOFs containing open metal sites through the coordination of ligands with acidic protons to those open metal sites. Such an

understanding would be key to developing a MOF/charge carrier system that could replace Nafion® in fuel cells.

6. Conclusions

In this thesis we presented the results of the application of different computational modeling approaches to the study of three different MOFs, with some of them currently under ongoing study. Different methodologies, from *ab initio* Density Functional Theory methods to Molecular Mechanics have been explored for the computational modeling of MOFs.

The study of electronic polarization effects on water adsorption in MIL-53(Cr) quantitatively shows the importance of polarization in molecular dynamics simulations of MOFs. In particular, many body water-framework and water-water interactions cannot be accurately described by non-polarizable force fields, while polarizable force fields are able to recover part of these interactions. Similarly, potential energy scans of framework interactions with a single water molecule using non-polarizable and polarizable force fields are insufficient in the parameterization of these many-body effects. Consequently, future modeling of MOFs involving interactions with polarizable molecules such as water will require the usage of polarizable force fields for accurate description of the host guest interaction.

The study of the regioisomeric frameworks DMOF-2,3-NH_2Cl and DMOF-2,5-NH_2Cl leads to several conclusions concerning the breathing behavior of MOFs. The MD simulations of the solvent-loaded frameworks show that different solvents do not lead to differences in breathing behavior of regioisomeric frameworks, indicating that breathing is an inherent property of the framework. Furthermore, studies of the pore-closing mechanism indicate that for MOFs with asymmetric ligands, different distributions of the orientations of the ligands lead to non-negligible differences in the

large pore to narrow pore energy barrier for the regioisomers. This means that a natural, long-range order can arise in the structure of a MOF during synthesis. These conclusions underscore the importance in understanding the nucleation and crystal growth of MOFs during synthesis, and that breathing behavior might be tunable during the synthetic process in a more subtle fashion than replacement of one organic linker with another.

The study of the control of proton conduction in HKUST-1 demonstrates that it is feasible to simulate ligands bound to open-metal sites and to get reasonable results. Even though a bonded force field representation of the ligands complexed to the Cu open metal sites does not exactly model the nature of the Cu-water interaction in HKUST-1, our current force field is able to generate a hydrogen bond network capable, as the radial function distribution functions show, of proton conduction via the Grotthuss mechanism.

Though the frameworks modeled in this work are composed largely of "iconic" frameworks that are very commonly studied, the results are applicable to more than just these three frameworks. In fact, the conclusions reached in these studies can be extended to any framework. Ultimately, the work here forms a foundation that other future computational studies of MOF materials can build on.

Appendix A: Additional RDFs of H_2O in MIL-53(Cr)

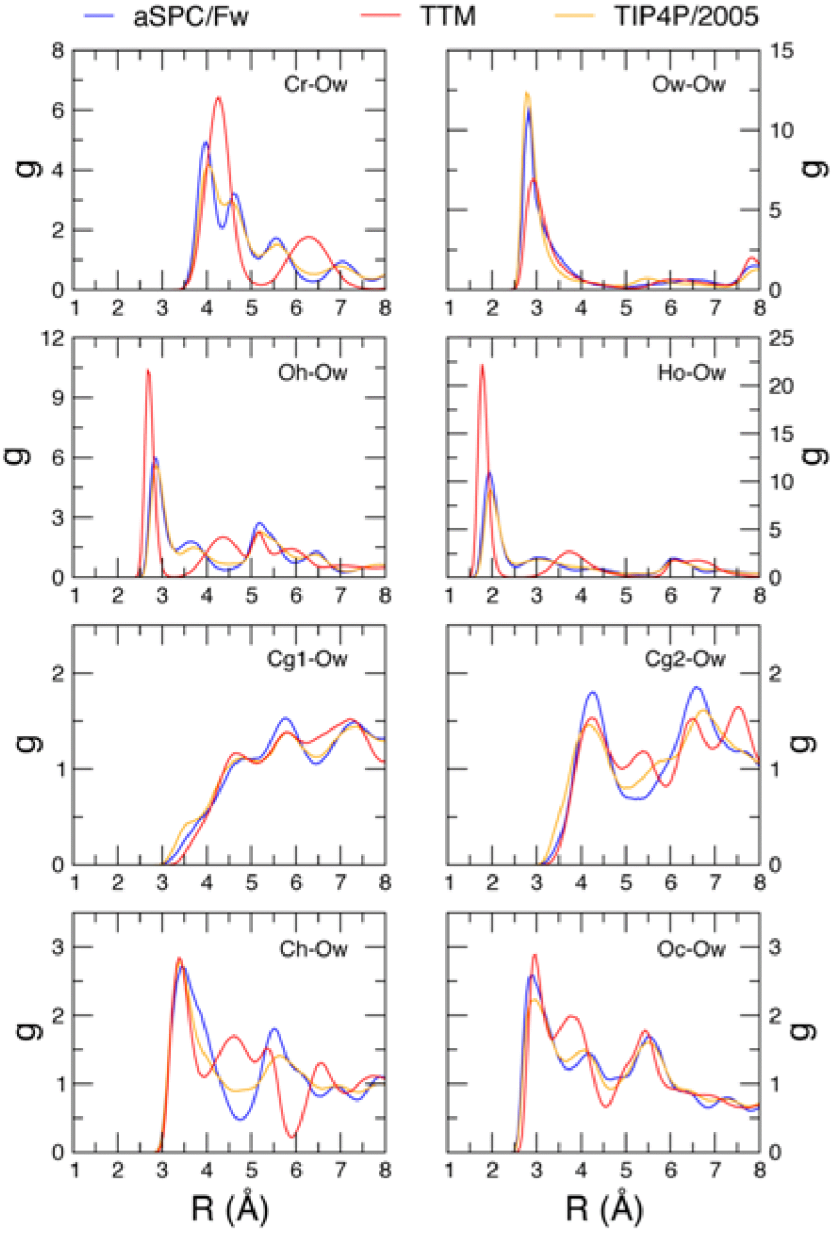

Figure A.1 – Radial distribution functions involving the Ow atom of the H_2O molecules calculated using the non-polarizable Aspc/Fw (blue) and TIP4P/2005 (orange) force fields, and the polarizable TTM (red) force fields for $N_{H_2O} = 3$. The atom labels are described in Figure 3.1b.

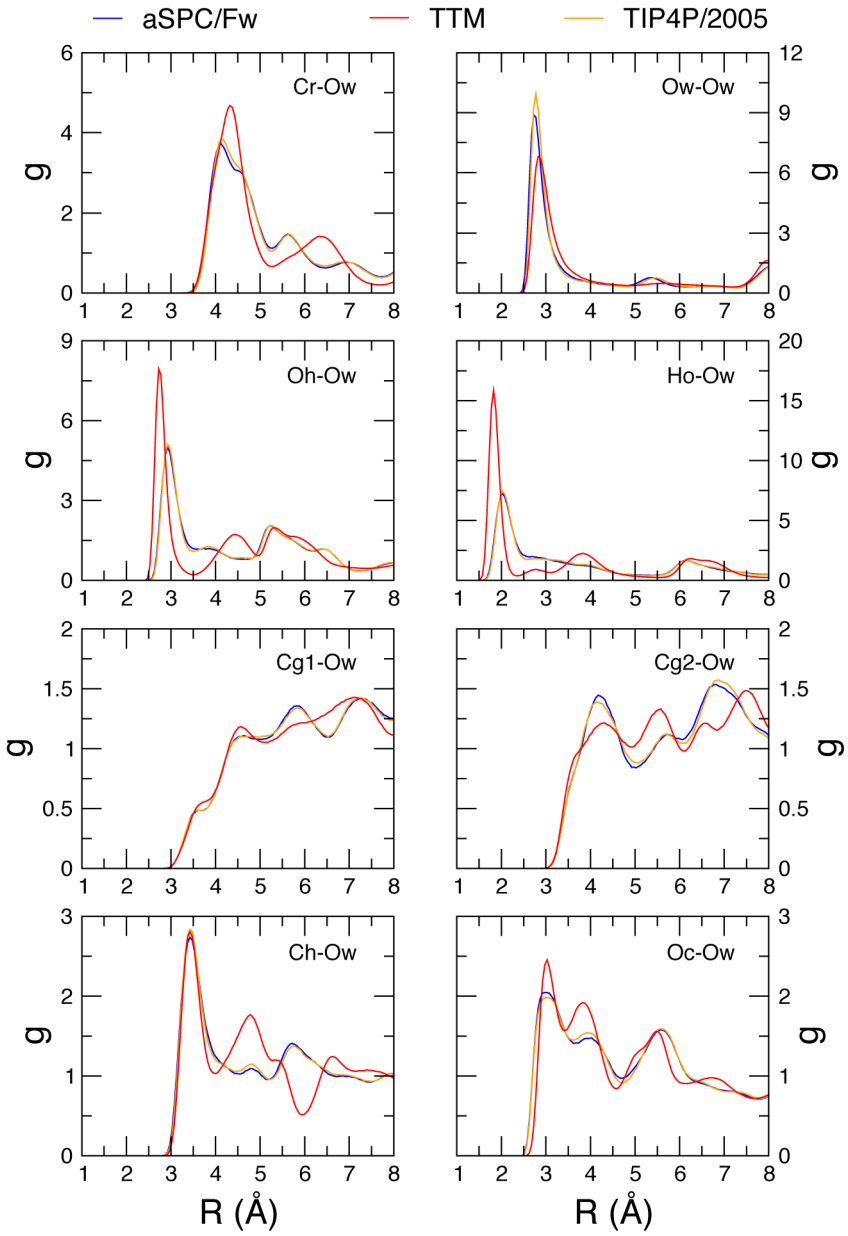

Figure A.2 – Radial distribution functions involving the Ow atom of the H_2O molecules calculated using the non-polarizable Aspc/Fw (blue) and TIP4P/2005 (orange) force fields, and the polarizable TTM (red) force fields for $N_{H_2O} = 5$. The atom labels are described in Figure 3.1b.

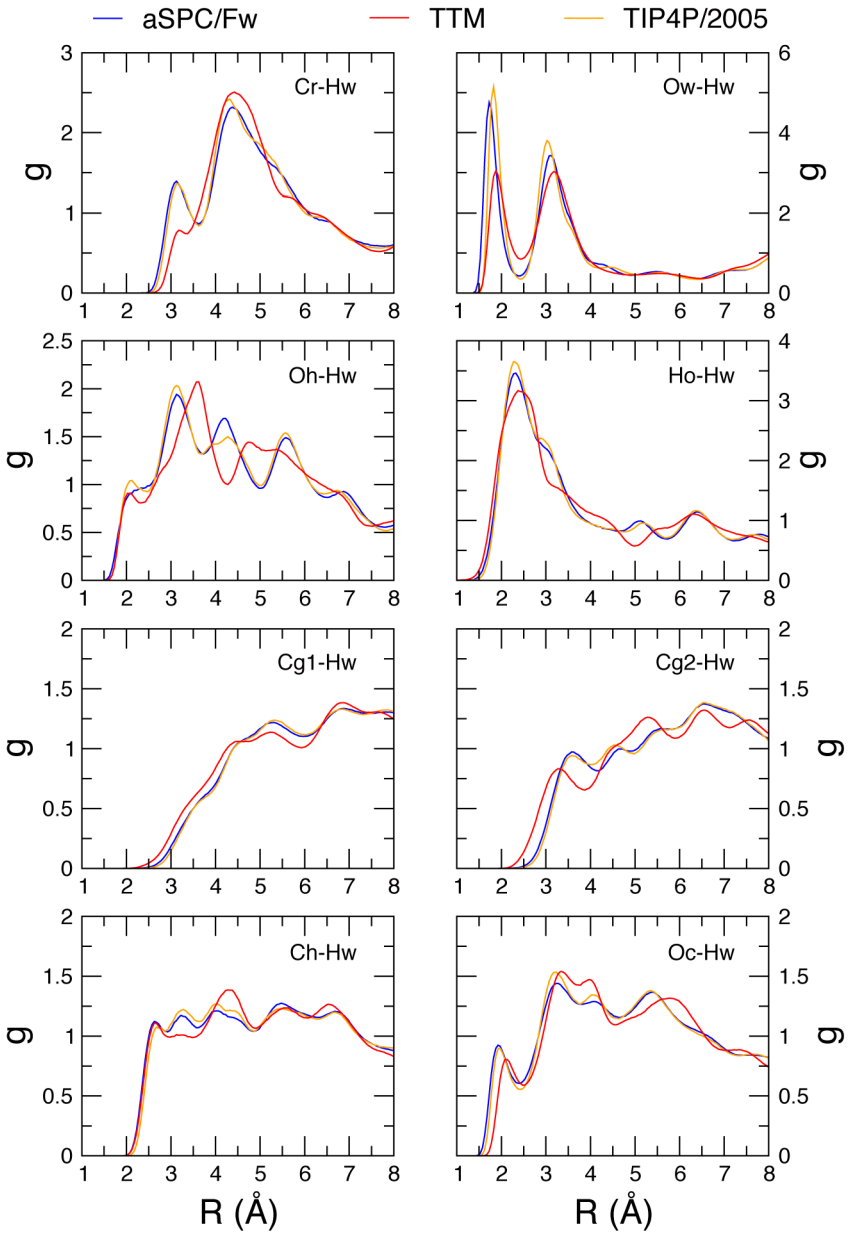

Figure A.3 – Radial distribution functions involving the Ow atom of the H_2O molecules calculated using the non-polarizable Aspc/Fw (blue) and TIP4P/2005 (orange) force fields, and the polarizable TTM (red) force fields for $N_{H_2O} = 7$. The atom labels are described in Figure 3.1b.

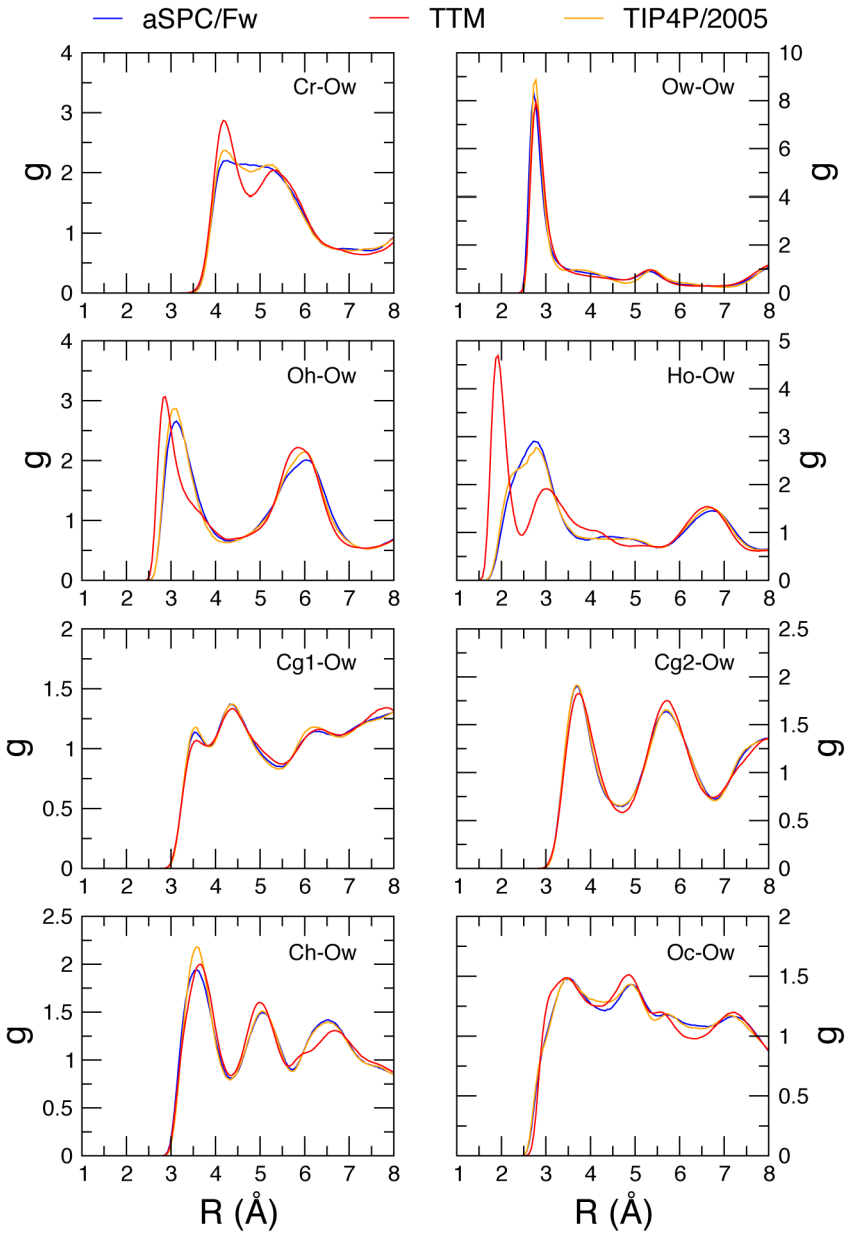

Figure A.4 – Radial distribution functions involving the Ow atom of the H_2O molecules calculated using the non-polarizable Aspc/Fw (blue) and TIP4P/2005 (orange) force fields, and the polarizable TTM (red) force fields for $N_{H_2O} = 10$. The atom labels are described in Figure 3.1b.

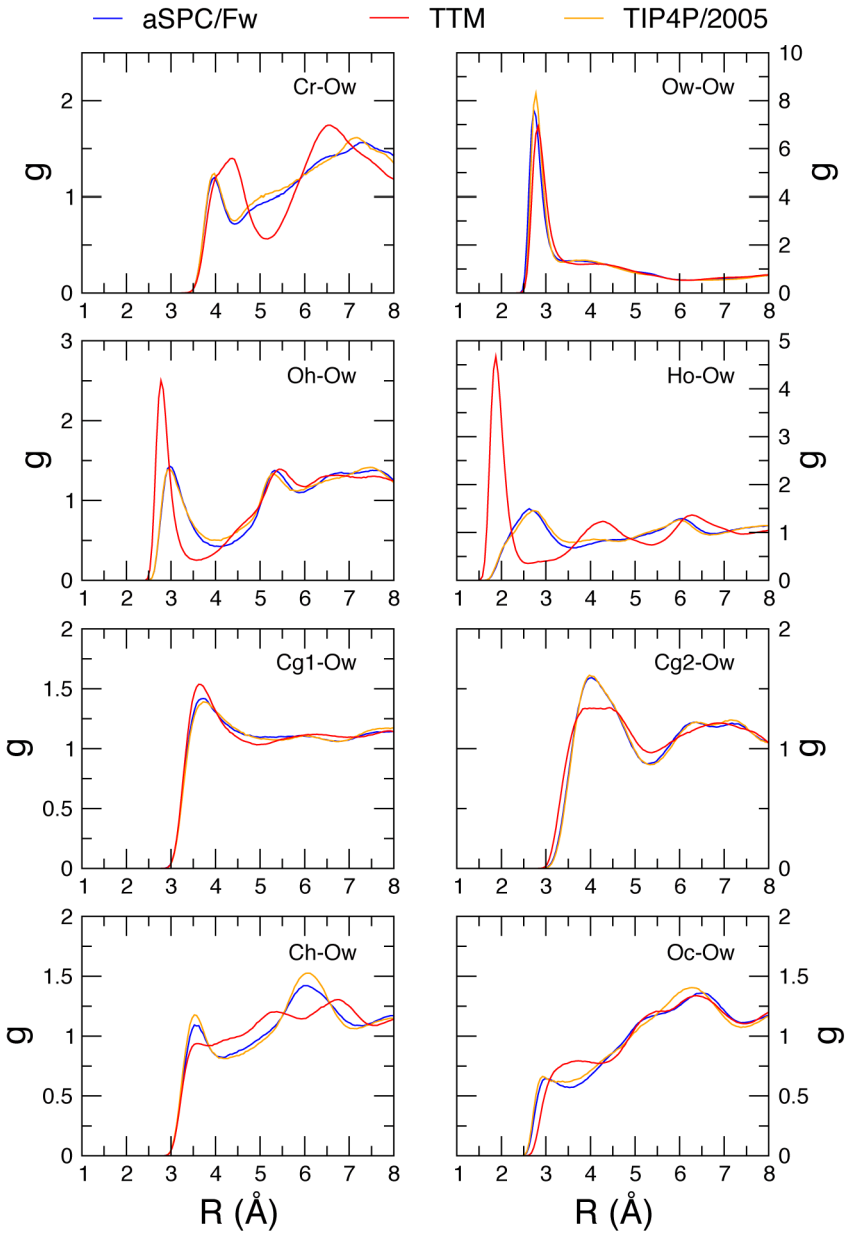

Figure A.5 – Radial distribution functions involving the Ow atom of the H_2O molecules calculated using the non-polarizable Aspc/Fw (blue) and TIP4P/2005 (orange) force fields, and the polarizable TTM (red) force fields for $N_{H_2O} = 14$. The atom labels are described in Figure 3.1b.

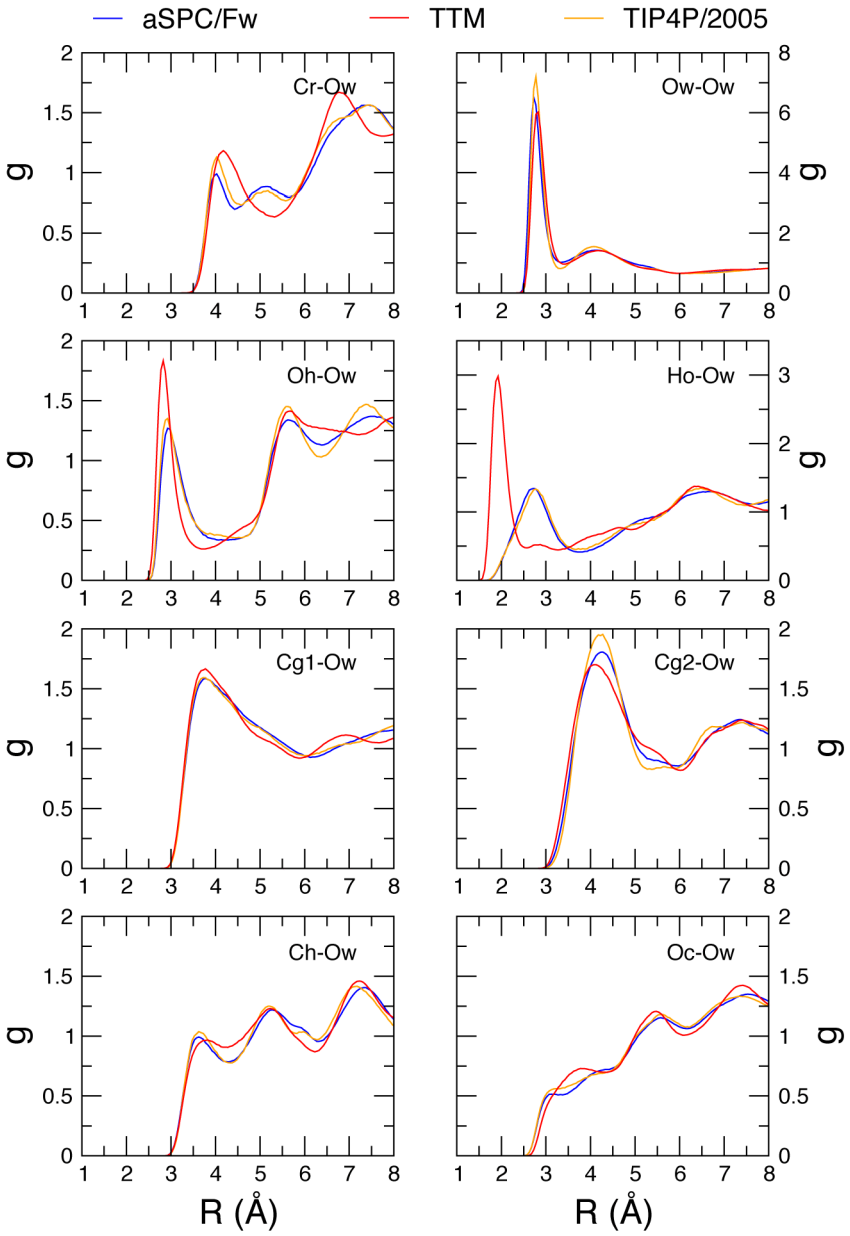

Figure A.6 – Radial distribution functions involving the Ow atom of the H_2O molecules calculated using the non-polarizable Aspc/Fw (blue) and TIP4P/2005 (orange) force fields, and the polarizable TTM (red) force fields for $N_{H_2O} = 20$. The atom labels are described in Figure 3.1b.

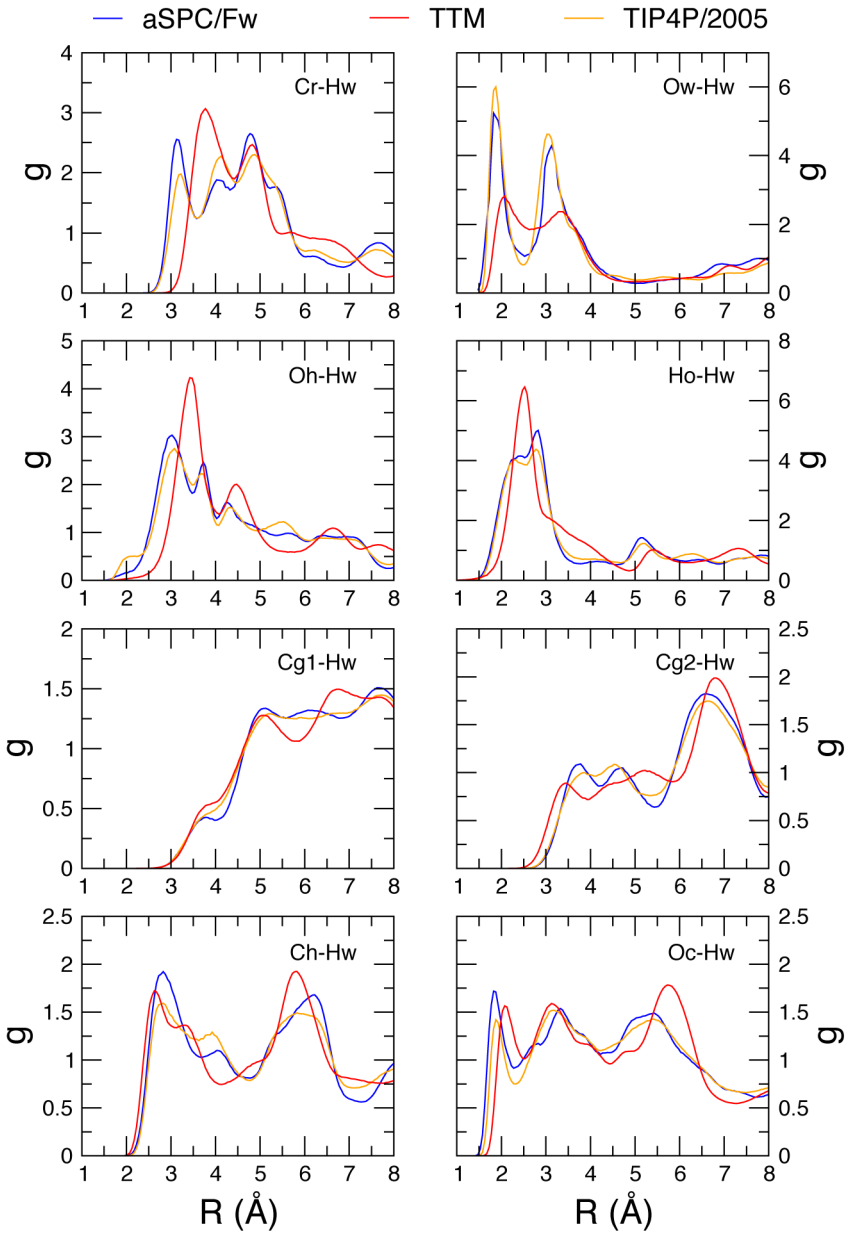

Figure A.7 – Radial distribution functions involving the Hw atom of the H_2O molecules calculated using the non-polarizable Aspc/Fw (blue) and TIP4P/2005 (orange) force fields, and the polarizable TTM (red) force fields for $N_{H_2O} = 3$. The atom labels are described in Figure 3.1b.

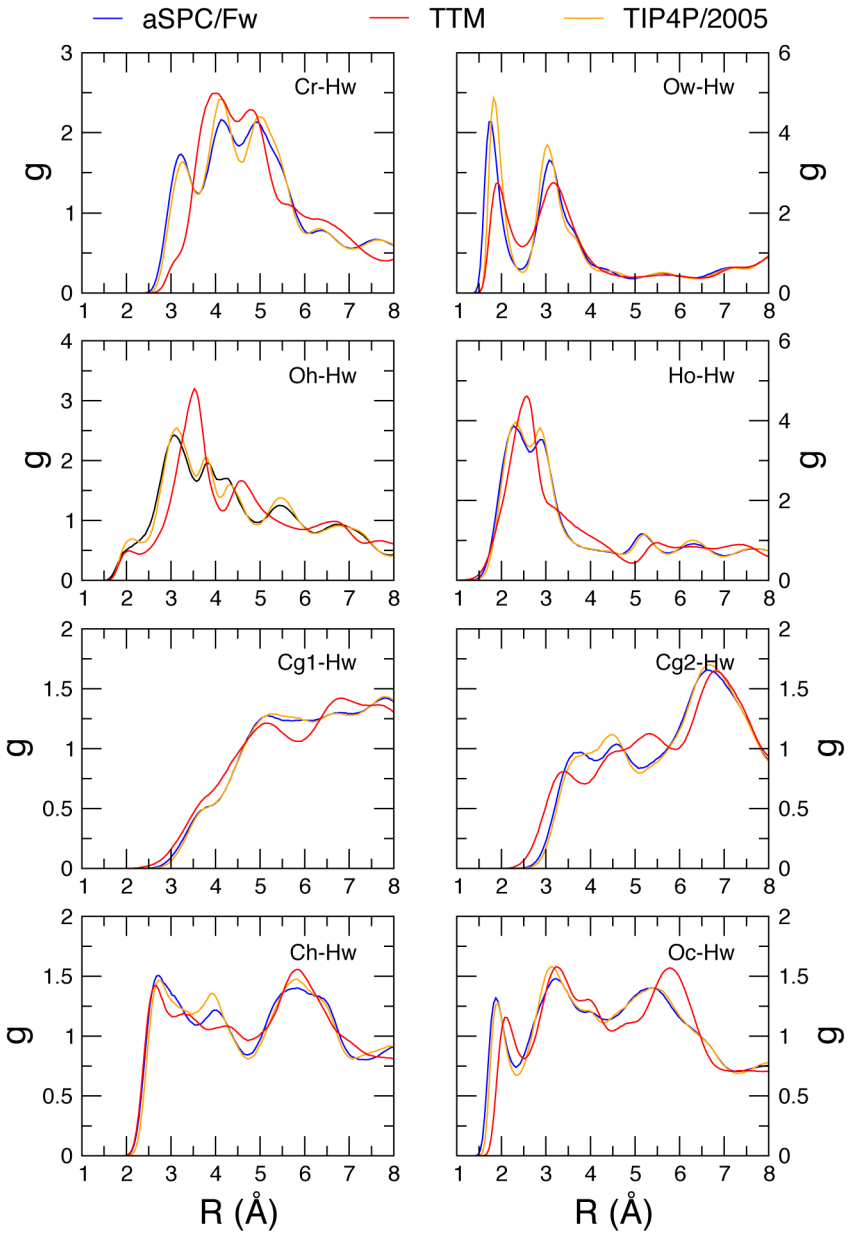

Figure A.8 – Radial distribution functions involving the Hw atom of the H_2O molecules calculated using the non-polarizable Aspc/Fw (blue) and TIP4P/2005 (orange) force fields, and the polarizable TTM (red) force fields for $N_{H_2O} = 5$. The atom labels are described in Figure 3.1b.

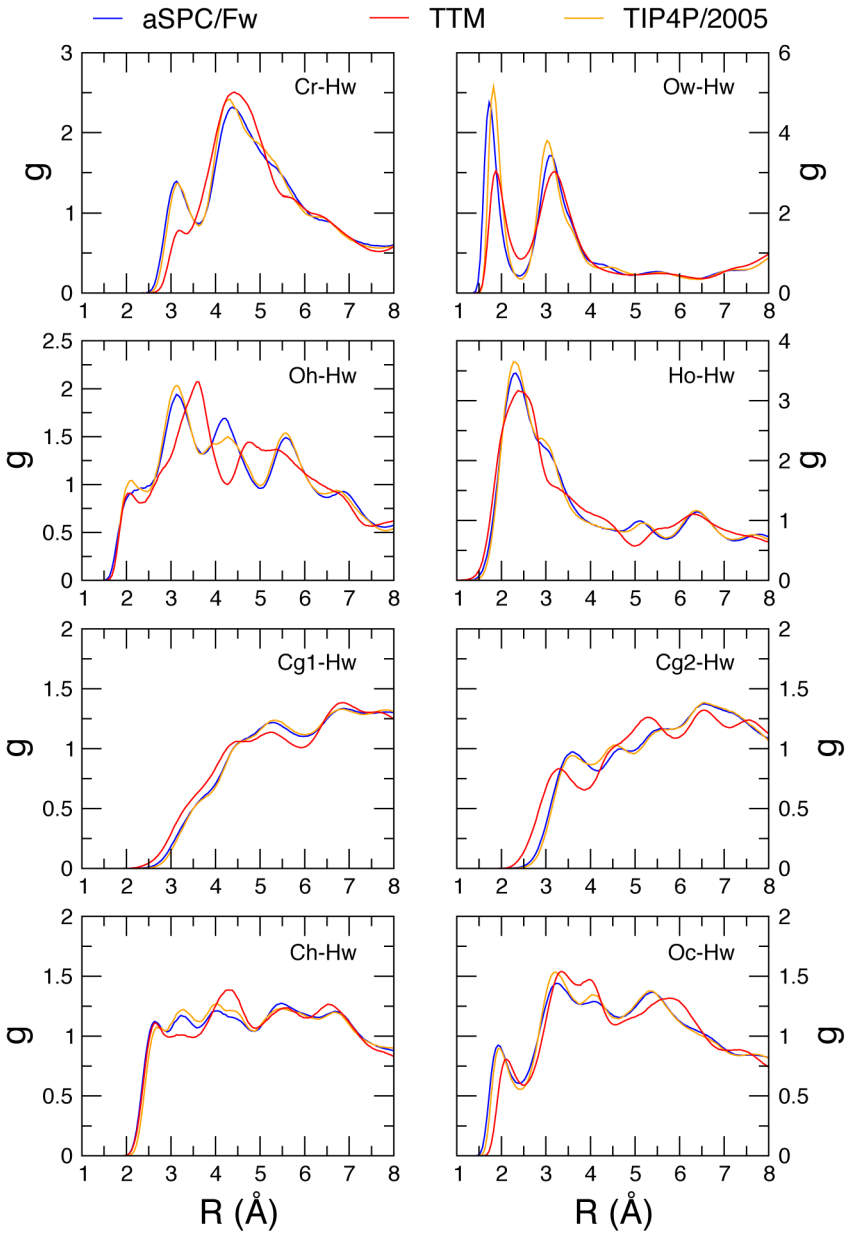

Figure A.9 – Radial distribution functions involving the Hw atom of the H_2O molecules calculated using the non-polarizable Aspc/Fw (blue) and TIP4P/2005 (orange) force fields, and the polarizable TTM (red) force fields for $N_{H_2O} = 7$. The atom labels are described in Figure 3.1b.

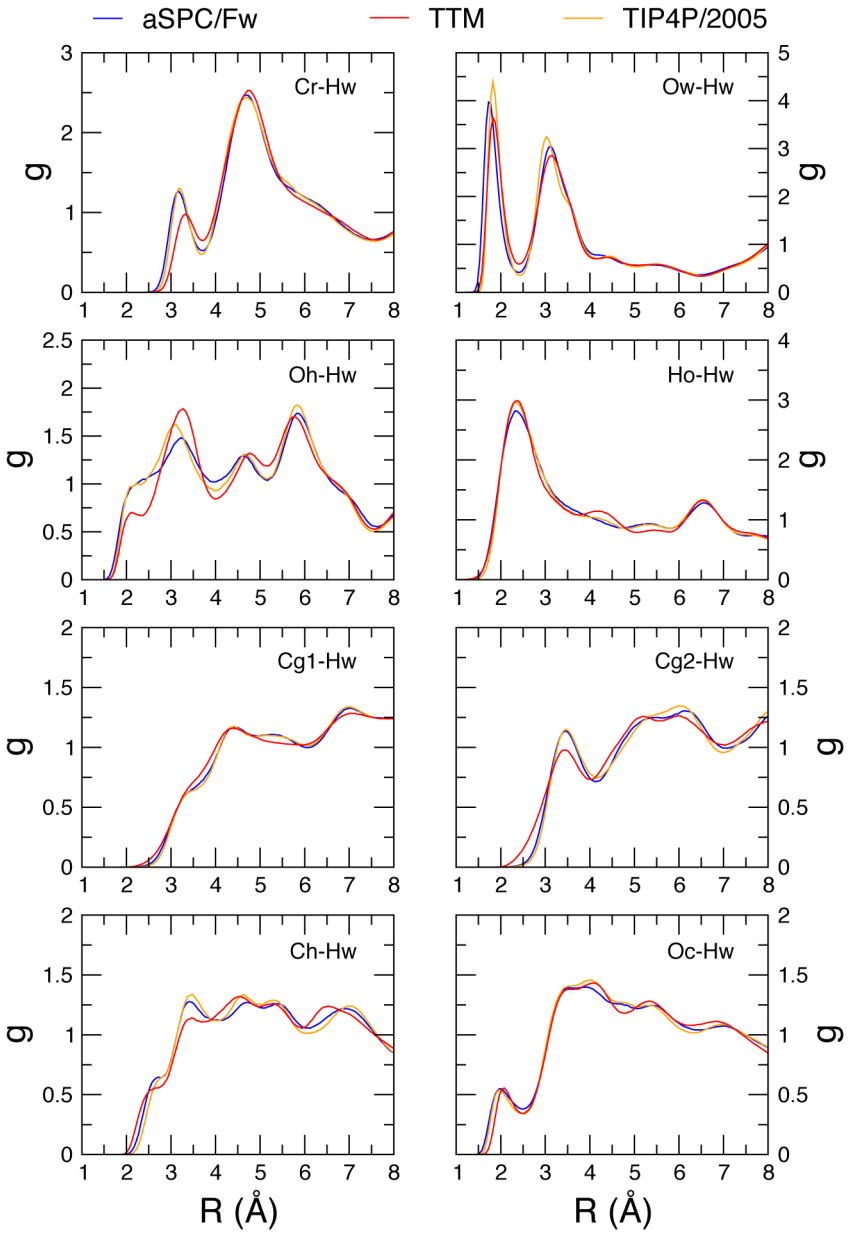

Figure A.10 – Radial distribution functions involving the Hw atom of the H_2O molecules calculated using the non-polarizable Aspc/Fw (blue) and TIP4P/2005 (orange) force fields, and the polarizable TTM (red) force fields for $N_{H_2O} = 10$. The atom labels are described in Figure 3.1b.

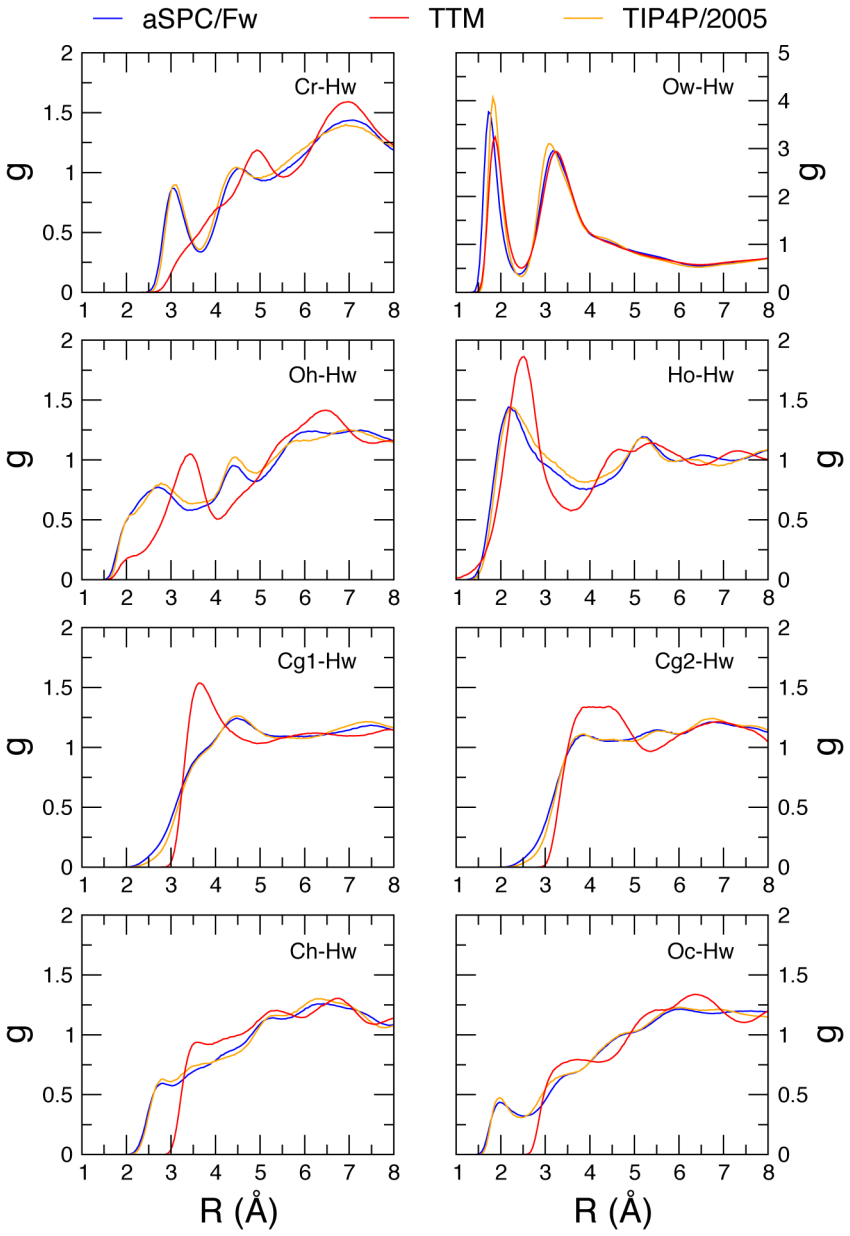

Figure A.11 – Radial distribution functions involving the Hw atom of the H_2O molecules calculated using the non-polarizable Aspc/Fw (blue) and TIP4P/2005 (orange) force fields, and the polarizable TTM (red) force fields for $N_{H_2O} = 14$. The atom labels are described in Figure 3.1b.

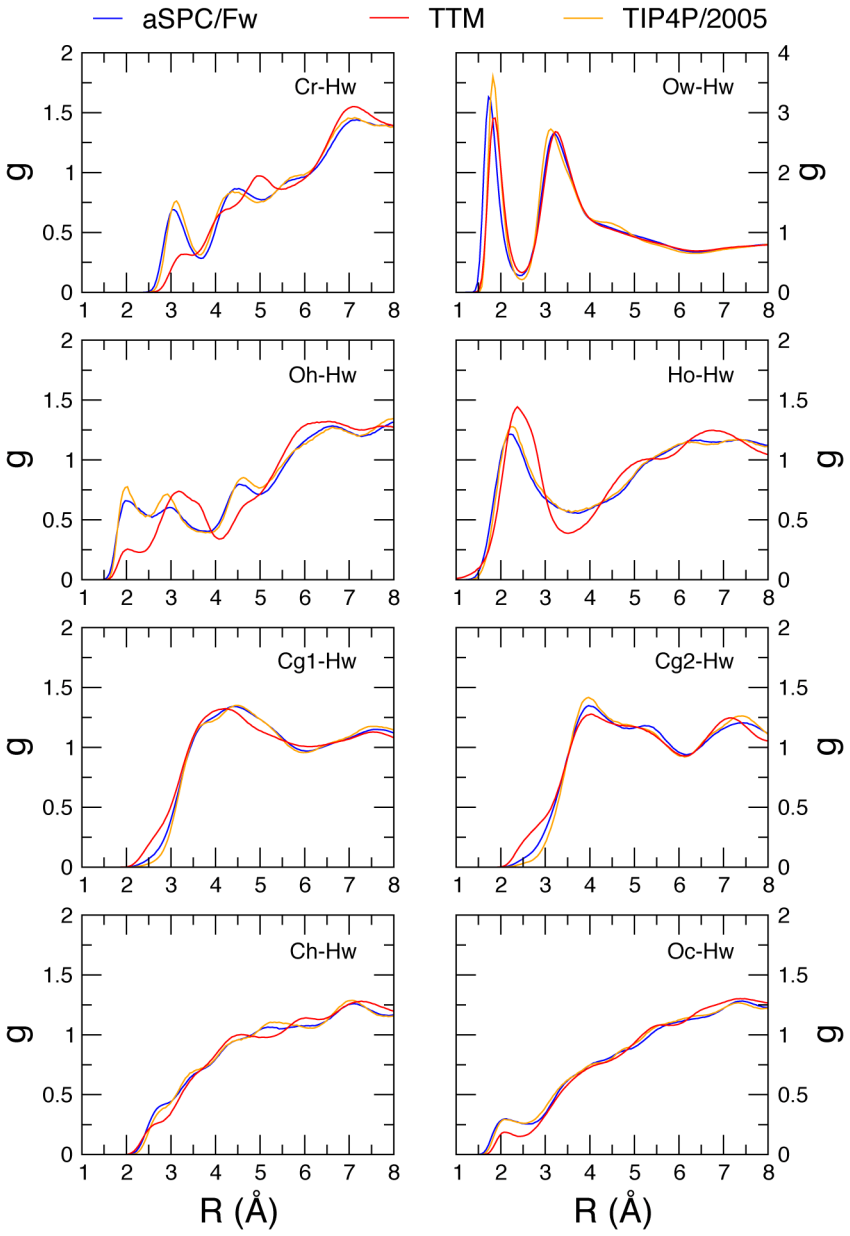

Figure A.12 – Radial distribution functions involving the Hw atom of the H_2O molecules calculated using the non-polarizable Aspc/Fw (blue) and TIP4P/2005 (orange) force fields, and the polarizable TTM (red) force fields for $N_{H_2O} = 20$. The atom labels are described in Figure 3.1b.

Appendix B: DMOF-2,3-NH_2Cl and DMOF-2,5-NH_2Cl Supplemental Data

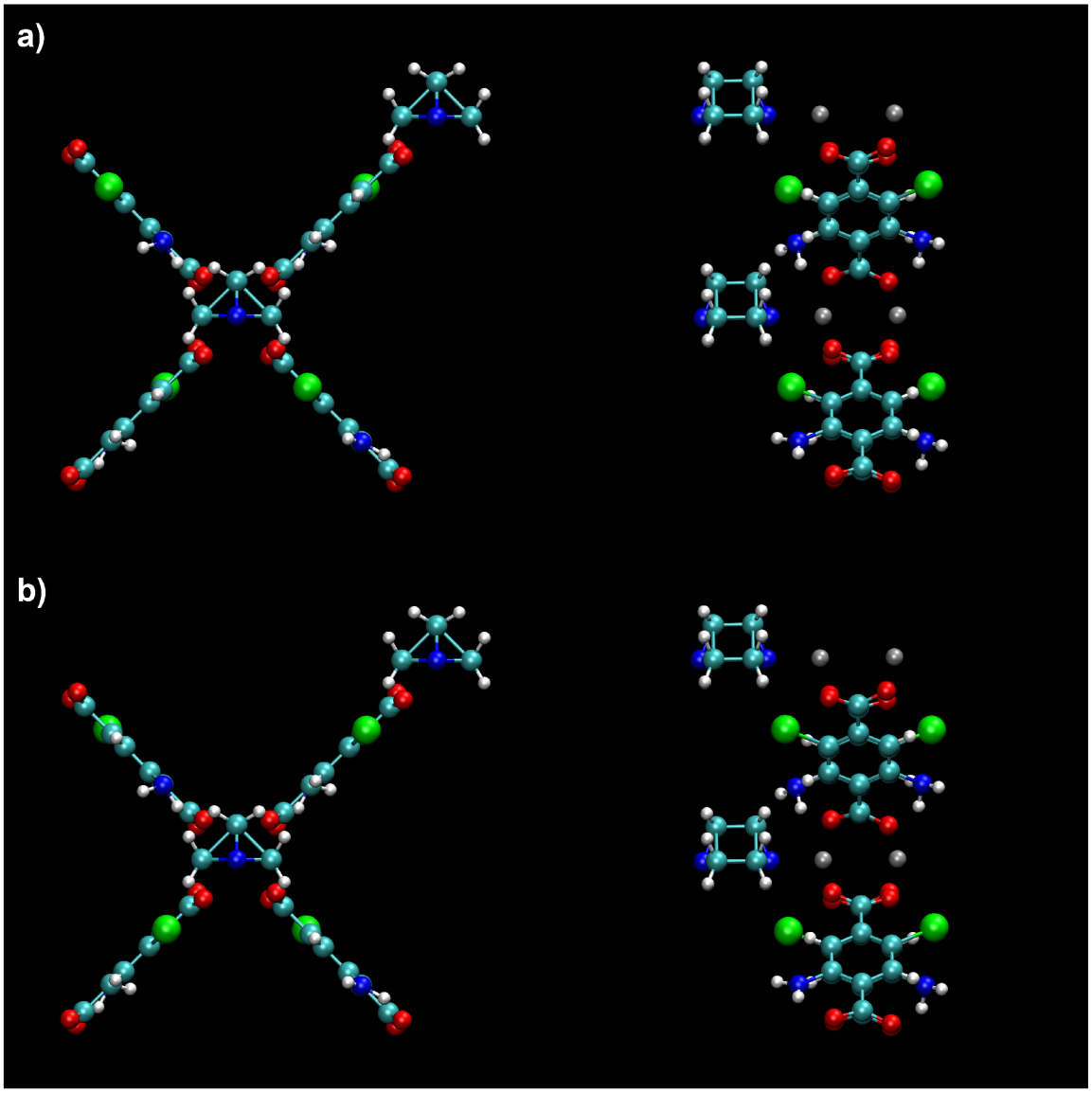

Figure B.1 – Cluster of 2 unit cells in the *x* and *y* directions (left and right, respectively) for the (a) ortho-DMOF and (b) para-DMOF systems. This 2 cell cluster was replicated 2 $\times 2 \times 1$ times in the *x*, *y*, and *z* directions, respectively, to generate the 16 unit cell system used in the MD simulations.

File B.1 – PDB file of the ortho-DMOF 2 unit cell cluster

```
CRYST1  15.4556  15.4556   9.6084  90.00  90.00  90.00    P4/mmm
HETATM    1 ZN   ZNC     1      16.393  27.322  39.876                  Zn
TER
HETATM    2 ZN   ZNC     2      16.393  27.322  36.992                  Zn
TER
HETATM    3  O2  LG1     3       7.457  27.145  37.325                   O
HETATM    4  C5  LG1     3       8.035  27.322  38.434                   C
HETATM    5  O1  LG1     3       7.457  27.499  39.543                   O
HETATM    6  C4  LG1     3       9.536  27.322  38.434                   C
HETATM    7  C6  LG1     3      10.237  27.322  39.605                   C
HETATM    8  H1  LG1     3       9.773  27.322  40.423                   H
HETATM    9  C7  LG1     3      11.621  27.322  39.605                   C
HETATM   10  H4  LG1     3      12.085  27.322  40.423                   H
HETATM   11  C1  LG1     3      12.322  27.322  38.434                   C
HETATM   12  C8  LG1     3      13.823  27.322  38.434                   C
HETATM   13  O3  LG1     3      14.401  27.145  39.543                   O
HETATM   14  O4  LG1     3      14.401  27.499  37.325                   O
HETATM   15  C2  LG1     3      11.621  27.322  37.263                   C
HETATM   16 Cl   LG1     3      12.493  27.322  35.725                  Cl
HETATM   17  C3  LG1     3      10.237  27.322  37.263                   C
HETATM   18  N1  LG1     3       9.512  27.322  35.984                   N
HETATM   19  H2  LG1     3       8.561  27.054  36.140                   H
HETATM   20  H3  LG1     3       9.943  26.673  35.357                   H
TER
HETATM   21  O2  LG2     4      16.570  18.386  39.543                   O
HETATM   22  C5  LG2     4      16.393  18.964  38.434                   C
HETATM   23  O1  LG2     4      16.216  18.386  37.325                   O
HETATM   24  C4  LG2     4      16.393  20.465  38.434                   C
HETATM   25  C6  LG2     4      16.393  21.166  37.263                   C
HETATM   26  H1  LG2     4      16.393  20.702  36.445                   H
HETATM   27  C7  LG2     4      16.393  22.550  37.263                   C
HETATM   28  H4  LG2     4      16.393  23.014  36.445                   H
HETATM   29  C1  LG2     4      16.393  23.251  38.434                   C
HETATM   30  C8  LG2     4      16.393  24.752  38.434                   C
HETATM   31  O3  LG2     4      16.216  25.330  37.325                   O
HETATM   32  O4  LG2     4      16.570  25.330  39.543                   O
HETATM   33  C2  LG2     4      16.393  22.550  39.605                   C
HETATM   34 Cl   LG2     4      16.393  23.422  41.143                  Cl
HETATM   35  C3  LG2     4      16.393  21.166  39.605                   C
HETATM   36  N1  LG2     4      16.393  20.441  40.884                   N
HETATM   37  H2  LG2     4      16.674  19.482  40.915                   H
HETATM   38  H3  LG2     4      16.112  20.907  41.723                   H
TER
HETATM   39  C2  DAB     5      17.343  28.272  42.470                   C
HETATM   40  H6  DAB     5      18.321  28.017  42.119                   H
HETATM   41  H7  DAB     5      17.088  29.250  42.119                   H
HETATM   42  C1  DAB     5      17.343  28.272  44.006                   C
HETATM   43  H1  DAB     5      17.088  29.250  44.357                   H
HETATM   44 2H1  DAB     5      18.321  28.017  44.357                   H
HETATM   45  N1  DAB     5      16.393  27.322  44.527                   N
HETATM   46  C4  DAB     5      15.444  28.272  44.006                   C
HETATM   47  H2  DAB     5      14.465  28.018  44.356                   H
HETATM   48  H3  DAB     5      15.699  29.250  44.356                   H
HETATM   49  C3  DAB     5      15.444  28.272  42.470                   C
```

```
HETATM   50  H4  DAB     5      14.466  28.018  42.119                H
HETATM   51  H5  DAB     5      15.699  29.250  42.119                H
HETATM   52  N2  DAB     5      16.393  27.322  41.950                N
HETATM   53  C6  DAB     5      17.343  26.373  42.470                C
HETATM   54  H10 DAB     5      18.321  26.628  42.119                H
HETATM   55 1H1  DAB     5      17.089  25.395  42.119                H
HETATM   56  C5  DAB     5      17.343  26.373  44.006                C
HETATM   57  H8  DAB     5      18.321  26.628  44.356                H
HETATM   58  H9  DAB     5      17.089  25.394  44.356                H
TER
HETATM   59 ZN   ZNC     6      27.322  27.322  39.876               Zn
TER
HETATM   60 ZN   ZNC     7      27.322  27.322  36.992               Zn
TER
HETATM   61  O2  LG3     8      18.386  27.145  37.325                O
HETATM   62  C5  LG3     8      18.964  27.322  38.434                C
HETATM   63  O1  LG3     8      18.386  27.499  39.543                O
HETATM   64  C4  LG3     8      20.465  27.322  38.434                C
HETATM   65  C6  LG3     8      21.166  27.322  39.605                C
HETATM   66  H1  LG3     8      20.702  27.322  40.423                H
HETATM   67  C7  LG3     8      22.550  27.322  39.605                C
HETATM   68  H4  LG3     8      23.014  27.322  40.423                H
HETATM   69  C1  LG3     8      23.251  27.322  38.434                C
HETATM   70  C8  LG3     8      24.752  27.322  38.434                C
HETATM   71  O3  LG3     8      25.330  27.145  39.543                O
HETATM   72  O4  LG3     8      25.330  27.499  37.325                O
HETATM   73  C2  LG3     8      22.550  27.322  37.263                C
HETATM   74 Cl   LG3     8      23.422  27.322  35.725               Cl
HETATM   75  C3  LG3     8      21.166  27.322  37.263                C
HETATM   76  N1  LG3     8      20.441  27.322  35.984                N
HETATM   77  H2  LG3     8      19.491  27.053  36.140                H
HETATM   78  H3  LG3     8      20.872  26.674  35.356                H
TER
HETATM   79  C2  DAB     9      28.272  28.272  42.470                C
HETATM   80  H6  DAB     9      29.250  28.017  42.119                H
HETATM   81  H7  DAB     9      28.017  29.250  42.119                H
HETATM   82  C1  DAB     9      28.272  28.272  44.006                C
HETATM   83  H1  DAB     9      28.017  29.250  44.357                H
HETATM   84 2H1  DAB     9      29.250  28.017  44.357                H
HETATM   85  N1  DAB     9      27.322  27.322  44.527                N
HETATM   86  C4  DAB     9      26.373  28.272  44.006                C
HETATM   87  H2  DAB     9      25.394  28.018  44.356                H
HETATM   88  H3  DAB     9      26.628  29.250  44.356                H
HETATM   89  C3  DAB     9      26.373  28.272  42.470                C
HETATM   90  H4  DAB     9      25.395  28.018  42.119                H
HETATM   91  H5  DAB     9      26.628  29.250  42.119                H
HETATM   92  N2  DAB     9      27.322  27.322  41.950                N
HETATM   93  C6  DAB     9      28.272  26.373  42.470                C
HETATM   94  H10 DAB     9      29.250  26.628  42.119                H
HETATM   95 1H1  DAB     9      28.018  25.395  42.119                H
HETATM   96  C5  DAB     9      28.272  26.373  44.006                C
HETATM   97  H8  DAB     9      29.250  26.628  44.356                H
HETATM   98  H9  DAB     9      28.018  25.394  44.356                H
TER
HETATM   99  O2  LG4    10      16.570  29.314  39.543                O
```

```
HETATM  100  C5  LG4     10      16.393  29.892  38.434                C
HETATM  101  O1  LG4     10      16.216  29.314  37.325                O
HETATM  102  C4  LG4     10      16.393  31.393  38.434                C
HETATM  103  C6  LG4     10      16.393  32.094  37.263                C
HETATM  104  H1  LG4     10      16.393  31.630  36.445                H
HETATM  105  C7  LG4     10      16.393  33.478  37.263                C
HETATM  106  H4  LG4     10      16.393  33.942  36.445                H
HETATM  107  C1  LG4     10      16.393  34.179  38.434                C
HETATM  108  C8  LG4     10      16.393  35.680  38.434                C
HETATM  109  O3  LG4     10      16.216  36.258  37.325                O
HETATM  110  O4  LG4     10      16.570  36.258  39.543                O
HETATM  111  C2  LG4     10      16.393  33.478  39.605                C
HETATM  112 Cl   LG4     10      16.393  34.350  41.143               Cl
HETATM  113  C3  LG4     10      16.393  32.094  39.605                C
HETATM  114  N1  LG4     10      16.393  31.369  40.884                N
HETATM  115  H2  LG4     10      16.211  30.400  40.718                H
HETATM  116  H3  LG4     10      15.683  31.744  41.480                H
END
```

File B.2 – PDB file of the para-DMOF 2 unit cell cluster

```
CRYST1  15.4556  15.4556   9.6084  90.00  90.00  90.00     P4/mmm
HETATM    1 ZN   ZNC     1      16.393  27.322  39.876               Zn
TER
HETATM    2 ZN   ZNC     2      16.393  27.322  36.992               Zn
TER
HETATM    3  O2  LG1     3       7.457  27.145  37.325                O
HETATM    4  C5  LG1     3       8.035  27.322  38.434                C
HETATM    5  O1  LG1     3       7.457  27.499  39.543                O
HETATM    6  C4  LG1     3       9.536  27.322  38.434                C
HETATM    7  C6  LG1     3      10.237  27.322  39.605                C
HETATM    8  H2  LG1     3       9.773  27.322  40.423                H
HETATM    9  C7  LG1     3      11.621  27.322  39.605                C
HETATM   10  C1  LG1     3      12.322  27.322  38.434                C
HETATM   11  C8  LG1     3      13.823  27.322  38.434                C
HETATM   12  O3  LG1     3      14.401  27.145  39.543                O
HETATM   13  O4  LG1     3      14.401  27.499  37.325                O
HETATM   14  C2  LG1     3      11.621  27.322  37.263                C
HETATM   15  H1  LG1     3      12.085  27.322  36.445                H
HETATM   16  C3  LG1     3      10.237  27.322  37.263                C
HETATM   17  N1  LG1     3       9.512  27.322  35.984                N
HETATM   18  H3  LG1     3       8.561  27.054  36.140                H
HETATM   19  H4  LG1     3       9.943  26.673  35.357                H
HETATM   20 Cl   LG1     3      12.563  27.322  41.266               Cl
TER
HETATM   21  O2  LG2     4      16.570  18.386  39.543                O
HETATM   22  C5  LG2     4      16.393  18.964  38.434                C
HETATM   23  O1  LG2     4      16.216  18.386  37.325                O
HETATM   24  C4  LG2     4      16.393  20.465  38.434                C
HETATM   25  C6  LG2     4      16.393  21.166  37.263                C
HETATM   26  H2  LG2     4      16.393  20.702  36.445                H
HETATM   27  C7  LG2     4      16.393  22.550  37.263                C
HETATM   28  C1  LG2     4      16.393  23.251  38.434                C
HETATM   29  C8  LG2     4      16.393  24.752  38.434                C
HETATM   30  O3  LG2     4      16.216  25.330  37.325                O
HETATM   31  O4  LG2     4      16.570  25.330  39.543                O
```

```
HETATM   32  C2  LG2     4      16.393  22.550  39.605                C
HETATM   33  H1  LG2     4      16.393  23.014  40.423                H
HETATM   34  C3  LG2     4      16.393  21.166  39.605                C
HETATM   35  N1  LG2     4      16.393  20.441  40.884                N
HETATM   36  H3  LG2     4      16.674  19.482  40.915                H
HETATM   37  H4  LG2     4      16.112  20.907  41.723                H
HETATM   38 Cl   LG2     4      16.393  23.492  35.602               Cl
TER
HETATM   39  C2  DAB     5      17.343  28.272  42.470                C
HETATM   40  H6  DAB     5      18.321  28.017  42.119                H
HETATM   41  H7  DAB     5      17.088  29.250  42.119                H
HETATM   42  C1  DAB     5      17.343  28.272  44.006                C
HETATM   43  H1  DAB     5      17.088  29.250  44.357                H
HETATM   44 2H1  DAB     5      18.321  28.017  44.357                H
HETATM   45  N1  DAB     5      16.393  27.322  44.527                N
HETATM   46  C4  DAB     5      15.444  28.272  44.006                C
HETATM   47  H2  DAB     5      14.465  28.018  44.356                H
HETATM   48  H3  DAB     5      15.699  29.250  44.356                H
HETATM   49  C3  DAB     5      15.444  28.272  42.470                C
HETATM   50  H4  DAB     5      14.466  28.018  42.119                H
HETATM   51  H5  DAB     5      15.699  29.250  42.119                H
HETATM   52  N2  DAB     5      16.393  27.322  41.950                N
HETATM   53  C6  DAB     5      17.343  26.373  42.470                C
HETATM   54  H10 DAB     5      18.321  26.628  42.119                H
HETATM   55 1H1  DAB     5      17.089  25.395  42.119                H
HETATM   56  C5  DAB     5      17.343  26.373  44.006                C
HETATM   57  H8  DAB     5      18.321  26.628  44.356                H
HETATM   58  H9  DAB     5      17.089  25.394  44.356                H
TER
HETATM   59 ZN   ZNC     6      27.322  27.322  39.876               Zn
TER
HETATM   60 ZN   ZNC     7      27.322  27.322  36.992               Zn
TER
HETATM   61  O2  LG3     8      18.386  27.145  37.325                O
HETATM   62  C5  LG3     8      18.964  27.322  38.434                C
HETATM   63  O1  LG3     8      18.386  27.499  39.543                O
HETATM   64  C4  LG3     8      20.465  27.322  38.434                C
HETATM   65  C6  LG3     8      21.166  27.322  39.605                C
HETATM   66  H2  LG3     8      20.702  27.322  40.423                H
HETATM   67  C7  LG3     8      22.550  27.322  39.605                C
HETATM   68  C1  LG3     8      23.251  27.322  38.434                C
HETATM   69  C8  LG3     8      24.752  27.322  38.434                C
HETATM   70  O3  LG3     8      25.330  27.145  39.543                O
HETATM   71  O4  LG3     8      25.330  27.499  37.325                O
HETATM   72  C2  LG3     8      22.550  27.322  37.263                C
HETATM   73  H1  LG3     8      23.014  27.322  36.445                H
HETATM   74  C3  LG3     8      21.166  27.322  37.263                C
HETATM   75  N1  LG3     8      20.441  27.322  35.984                N
HETATM   76  H3  LG3     8      19.491  27.053  36.140                H
HETATM   77  H4  LG3     8      20.872  26.674  35.356                H
HETATM   78 Cl   LG3     8      23.492  27.322  41.266               Cl
TER
HETATM   79  C2  DAB     9      28.272  28.272  42.470                C
HETATM   80  H6  DAB     9      29.250  28.017  42.119                H
HETATM   81  H7  DAB     9      28.017  29.250  42.119                H
```

```
HETATM   82  C1  DAB     9      28.272  28.272  44.006                C
HETATM   83  H1  DAB     9      28.017  29.250  44.357                H
HETATM   84 2H1  DAB     9      29.250  28.017  44.357                H
HETATM   85  N1  DAB     9      27.322  27.322  44.527                N
HETATM   86  C4  DAB     9      26.373  28.272  44.006                C
HETATM   87  H2  DAB     9      25.394  28.018  44.356                H
HETATM   88  H3  DAB     9      26.628  29.250  44.356                H
HETATM   89  C3  DAB     9      26.373  28.272  42.470                C
HETATM   90  H4  DAB     9      25.395  28.018  42.119                H
HETATM   91  H5  DAB     9      26.628  29.250  42.119                H
HETATM   92  N2  DAB     9      27.322  27.322  41.950                N
HETATM   93  C6  DAB     9      28.272  26.373  42.470                C
HETATM   94  H10 DAB     9      29.250  26.628  42.119                H
HETATM   95 1H1  DAB     9      28.018  25.395  42.119                H
HETATM   96  C5  DAB     9      28.272  26.373  44.006                C
HETATM   97  H8  DAB     9      29.250  26.628  44.356                H
HETATM   98  H9  DAB     9      28.018  25.394  44.356                H
TER
HETATM   99  O2  LG4    10      16.570  29.314  39.543                O
HETATM  100  C5  LG4    10      16.393  29.892  38.434                C
HETATM  101  O1  LG4    10      16.216  29.314  37.325                O
HETATM  102  C4  LG4    10      16.393  31.393  38.434                C
HETATM  103  C6  LG4    10      16.393  32.094  37.263                C
HETATM  104  H2  LG4    10      16.393  31.630  36.445                H
HETATM  105  C7  LG4    10      16.393  33.478  37.263                C
HETATM  106  C1  LG4    10      16.393  34.179  38.434                C
HETATM  107  C8  LG4    10      16.393  35.680  38.434                C
HETATM  108  O3  LG4    10      16.216  36.258  37.325                O
HETATM  109  O4  LG4    10      16.570  36.258  39.543                O
HETATM  110  C2  LG4    10      16.393  33.478  39.605                C
HETATM  111  H1  LG4    10      16.393  33.942  40.423                H
HETATM  112  C3  LG4    10      16.393  32.094  39.605                C
HETATM  113  N1  LG4    10      16.393  31.369  40.884                N
HETATM  114  H3  LG4    10      16.211  30.400  40.718                H
HETATM  115  H4  LG4    10      15.683  31.744  41.480                H
HETATM  116 Cl   LG4    10      16.393  34.420  35.602               Cl
END
```

Table B.1 – Atomic partial charges for the ortho-DMOF 2 unit cell cluster
Atom types are defined in Figure 4.5.

Atom Type	Atomic Partial Charge
Zn	1.2299
Zn	1.2299
Nh	-0.7620
Hn	0.4224
Hn	0.2982
Ca	0.3544
Ca	-0.1346
Cl	-0.0677
Ca	0.1449
C2	0.6686
O	-0.7414
O	-0.6920
Ca	-0.2726
Ha	0.1576
Ca	-0.0750
Ha	0.1389
Ca	-0.1593
C2	0.7847
O	-0.8016
O	-0.7593
Nh	-0.7620
Hn	0.4224
Hn	0.2982
Ca	0.3544
Ca	-0.1346
Cl	-0.0677
Ca	0.1449
C2	0.6686
O	-0.7414
O	-0.6920
Ca	-0.2726
Ha	0.1576
Ca	-0.0750
Ha	0.1389
Ca	-0.1593
C2	0.7847
O	-0.8016
O	-0.7593
C3	-0.0003
H2	0.0195
H2	0.0195
C3	-0.0003

Table B.1 continued

Atom Type	Atomic Partial Charge
H2	0.0195
H2	0.0195
N	0.1500
C3	-0.0003
H2	0.0195
H2	0.0195
C3	-0.0003
H2	0.0195
H2	0.0195
N	0.1500
C3	-0.0003
H2	0.0195
H2	0.0195
C3	-0.0003
H2	0.0195
H2	0.0195
Zn	1.2299
Zn	1.2299
Nh	-0.7620
Hn	0.4224
Hn	0.2982
Ca	0.3544
Ca	-0.1346
Cl	-0.0677
Ca	0.1449
C2	0.6686
O	-0.7414
O	-0.6920
Ca	-0.2726
Ha	0.1576
Ca	-0.0750
Ha	0.1389
Ca	-0.1593
C2	0.7847
O	-0.8016
O	-0.7593
C3	-0.0003
H2	0.0195
H2	0.0195
C3	-0.0003
H2	0.0195
H2	0.0195
N	0.1500

Table B.1 continued

Atom Type	Atomic Partial Charge
C3	-0.0003
H2	0.0195
H2	0.0195
C3	-0.0003
H2	0.0195
H2	0.0195
N	0.1500
C3	-0.0003
H2	0.0195
H2	0.0195
C3	-0.0003
H2	0.0195
H2	0.0195
Nh	-0.7620
Hn	0.4224
Hn	0.2982
Ca	0.3544
Ca	-0.1346
Cl	-0.0677
Ca	0.1449
C2	0.6686
O	-0.7414
O	-0.6920
Ca	-0.2726
Ha	0.1576
Ca	-0.0750
Ha	0.1389
Ca	-0.1593
C2	0.7847
O	-0.8016
O	-0.7593

Table B.2 – Atomic partial charges for the para-DMOF 2 unit cell cluster
Atom types are defined in Figure 4.5.

Atom Type	Atomic Partial Charge
Zn	1.2202
Zn	1.2202
Nh	-0.7026
Hn	0.3480
Hn	0.3118
Ca	0.3118
Ca	-0.3437
Ha	0.2028

Table B.2 continued

Atom Type	Atomic Partial Charge
Ca	0.1240
C2	0.6974
O	-0.6921
O	-0.7757
Ca	-0.0380
Cl	-0.1212
Ca	-0.0788
Ha	0.1202
Ca	-0.1097
C2	0.7180
O	-0.7397
O	-0.7190
Nh	-0.7026
Hn	0.3480
Hn	0.3118
Ca	0.3118
Ca	-0.3437
Ha	0.2028
Ca	0.1240
C2	0.6974
O	-0.6921
O	-0.7757
Ca	-0.0380
Cl	-0.1212
Ca	-0.0788
Ha	0.1202
Ca	-0.1097
C2	0.7180
O	-0.7397
O	-0.7190
C3	-0.0003
H2	0.0195
H2	0.0195
C3	-0.0003
H2	0.0195
H2	0.0195
N	0.1500
C3	-0.0003
H2	0.0195
H2	0.0195
C3	-0.0003
H2	0.0195
H2	0.0195

Table B.2 continued

Atom Type	Atomic Partial Charge
N	0.1500
C3	-0.0003
H2	0.0195
H2	0.0195
C3	-0.0003
H2	0.0195
H2	0.0195
Zn	1.2202
Zn	1.2202
Nh	-0.7026
Hn	0.3480
Hn	0.3118
Ca	0.3118
Ca	-0.3437
Ha	0.2028
Ca	0.1240
C2	0.6974
O	-0.6921
O	-0.7757
Ca	-0.0380
Cl	-0.1212
Ca	-0.0788
Ha	0.1202
Ca	-0.1097
C2	0.7180
O	-0.7397
O	-0.7190
C3	-0.0003
H2	0.0195
H2	0.0195
C3	-0.0003
H2	0.0195
H2	0.0195
N	0.1500
C3	-0.0003
H2	0.0195
H2	0.0195
C3	-0.0003
H2	0.0195
H2	0.0195
N	0.1500
C3	-0.0003
H2	0.0195

Table B.2 continued

Atom Type	Atomic Partial Charge
H2	0.0195
C3	-0.0003
H2	0.0195
H2	0.0195
Nh	-0.7026
Hn	0.3480
Hn	0.3118
Ca	0.3118
Ca	-0.3437
Ha	0.2028
Ca	0.1240
C2	0.6974
O	-0.6921
O	-0.7757
Ca	-0.0380
Cl	-0.1212
Ca	-0.0788
Ha	0.1202
Ca	-0.1097
C2	0.7180
O	-0.7397
O	-0.7190

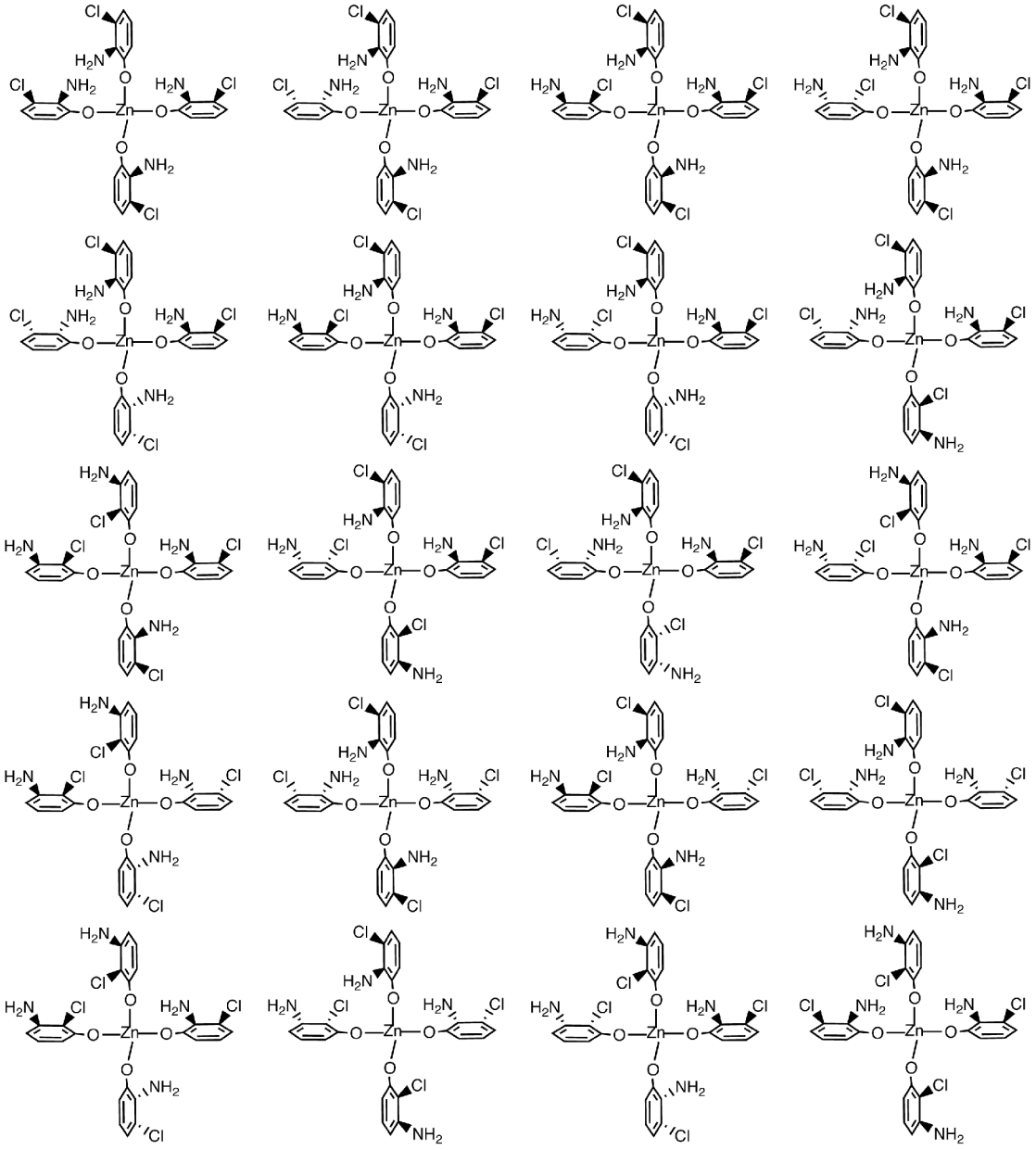

Figure B.2 – Possible BDC ligand orientation distributions for DMOF-2,3-NH_2Cl.
The structures shown correspond to the view of the Zn cluster from the *z* axis, centered on the Zn dimer – there are Zn and O atoms situated directly below the ones shown in the structures.
Dashed bonds correspond to substituents oriented downwards into the plane of the page, and wedge bonds to substituents oriented out of the plane of the page.

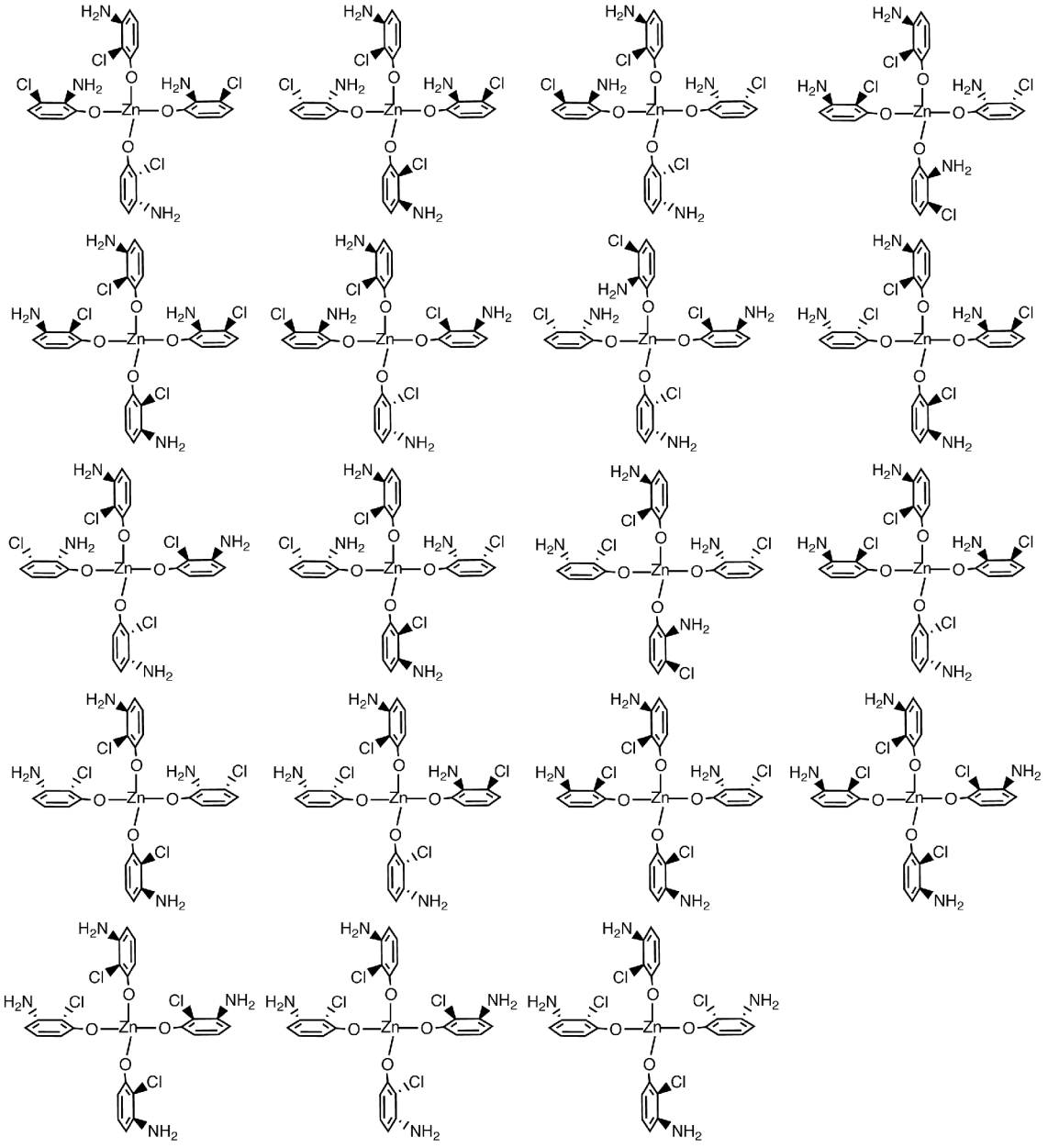

Figure B.2 continued

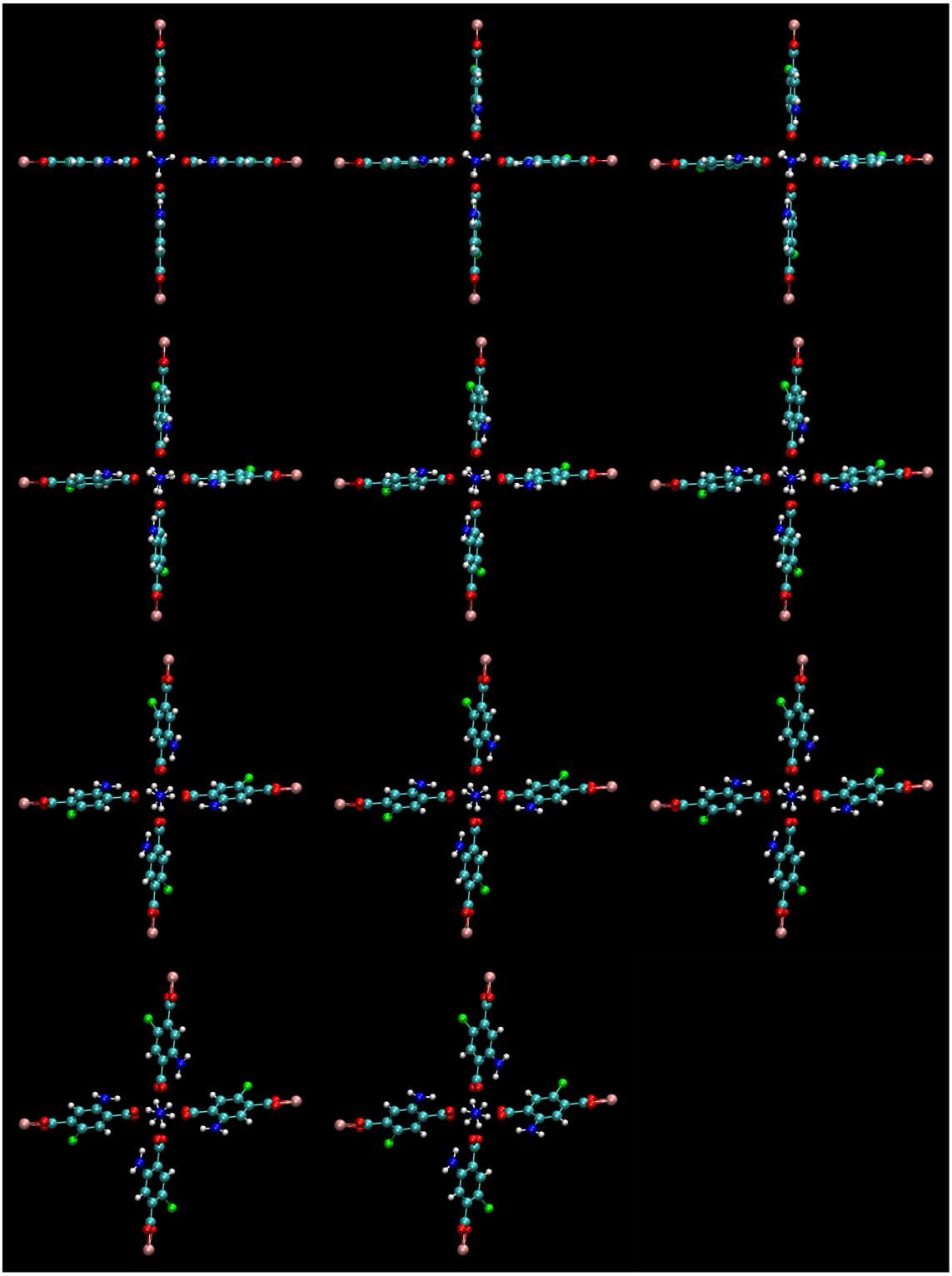

Figure B.3 – Cross configurations representing pore closing. The initial and final configurations were adapted from X-Ray data.

References

(1) Sing, K. S. W.; Everett, D. H.; Haul, R. A. W.; Moscou, L.; Pierotti, R. A.; Rouquérol, J.; Siemieniewska, T. *Pure and Applied Chemistry* **1985**, *57*, 603.

(2) Lowell, S.; Shields, J. E.; Thomas, M. A.; Thommes, M. *Characterization of Porous Solids and Powders: Surface Area, Pore Size and Density*; Kluwer Academic Publishers: Dordrecht, 2004.

(3) Langmuir, I. *Journal of the American Chemical Society* **1916**, *38*, 2221.

(4) Brunauer, S.; Emmett, P. H.; Teller, E. *Journal of the American Chemical Society* **1938**, *60*, 309.

(5) Mumpton, F. A. *Proceedings of the National Academy of Sciences* **1999**, *96*, 3463.

(6) Sinnott, S. B.; Andrews, R. *Critical Reviews in Solid State and Materials Sciences* **2001**, *26*, 145.

(7) *Metal-Organic Frameworks: Design and Application*; MacGillivray, L. R., Ed.; John Wiley & Sons: Hoboken, 2010.

(8) Su, J.; Guo, H. *The Journal of Physical Chemistry B* **2012**.

(9) Hofmann, K. A.; Küspert, F. *Zeitschrift für anorganische Chemie* **1897**, *15*, 204.

(10) Rayner, J. H.; Powell, H. M. *Journal of the Chemical Society (Resumed)* **1952**, 319.

(11) Hoskins, B. F.; Robson, R. *Journal of the American Chemical Society* **1989**, *111*, 5962.

(12) Yaghi, O. M.; Li, H.; Davis, C.; Richardson, D.; Groy, T. L. *Accounts of Chemical Research* **1998**, *31*, 474.

(13) Eddaoudi, M.; Moler, D. B.; Li, H.; Chen, B.; Reineke, T. M.; O'Keeffe, M.; Yaghi, O. M. *Accounts of Chemical Research* **2001**, *34*, 319.

(14) Yaghi, O. M.; O'Keeffe, M.; Ockwig, N. W.; Chae, H. K.; Eddaoudi, M.; Kim, J. *Nature* **2003**, *423*, 705.

(15) Batten, S. R.; Champness, N. R.; Chen, X.-M.; Garcia-Martinez, J.; Kitagawa, S.; Ohrstrom, L.; O'Keeffe, M.; Suh, M. P.; Reedijk, J. *CrystEngComm* **2012**, *14*, 3001.

(16) Donaruma, L. G.; Block, B. P.; Loening, K. L.; Plate, N.; Tsuruta, T.; Buschbeck, K. C.; Powell, W. H.; Reedijk, J. *Pure and Applied Chemistry* **1985**, *57*, 149.

(17) *Nomenclature of Inorganic Chemistry IUPAC Recommendations 2005, International Union of Pure and Applied Chemistry*; Connelly, N. G.; Damhus, T.; Hartshorn, R. M.; Hutton, A. T., Eds.; The Royal Society of Chemistry: Cambridge, 2005.

(18) Férey, G.; Mellot-Draznieks, C.; Serre, C.; Millange, F.; Dutour, J.; Surblé, S.; Margiolaki, I. *Science* **2005**, *309*, 2040.

(19) Lee, J. Y.; Olson, D. H.; Pan, L.; Emge, T. J.; Li, J. *Advanced Functional Materials* **2007**, *17*, 1255.

(20) Hoffmann, H. C.; Assfour, B.; Epperlein, F.; Klein, N.; Paasch, S.; Senkovska, I.; Kaskel, S.; Seifert, G.; Brunner, E. *Journal of the American Chemical Society* **2011**, *133*, 8681.

(21) O'Keeffe, M.; Peskov, M. A.; Ramsden, S. J.; Yaghi, O. M. *Accounts of Chemical Research* **2008**, *41*, 1782.

(22) Huang, X.-C.; Lin, Y.-Y.; Zhang, J.-P.; Chen, X.-M. *Angewandte Chemie International Edition* **2006**, *45*, 1557.

(23) Li, H.; Eddaoudi, M.; Groy, T. L.; Yaghi, O. M. *Journal of the American Chemical Society* **1998**, *120*, 8571.

(24) Li, H.; Eddaoudi, M.; O'Keeffe, M.; Yaghi, O. M. *Nature* **1999**, *402*, 276.

(25) Tranchemontagne, D. J.; Mendoza-Cortes, J. L.; O'Keeffe, M.; Yaghi, O. M. *Chemical Society Reviews* **2009**, *38*, 1257.

(26) Shoaee, M.; Agger, J. R.; Anderson, M. W.; Attfield, M. P. *CrystEngComm* **2008**, *10*, 646.

(27) Millange, F.; Medina, M. I.; Guillou, N.; Férey, G.; Golden, K. M.; Walton, R. I. *Angewandte Chemie International Edition* **2010**, *49*, 763.

(28) Tanabe, K. K.; Wang, Z.; Cohen, S. M. *Journal of the American Chemical Society* **2008**, *130*, 8508.

(29) Wang, Z.; Cohen, S. M. *Journal of the American Chemical Society* **2009**, *131*, 16675.

(30) Keskin, S.; van Heest, T. M.; Sholl, D. S. *ChemSusChem* **2010**, *3*, 879.

(31) Bae, Y.-S.; Snurr, R. Q. *Angewandte Chemie International Edition* **2011**, *50*, 11586.

(32) Yoon, J. W.; Jhung, S. H.; Hwang, Y. K.; Humphrey, S. M.; Wood, P. T.; Chang, J. S. *Advanced Materials* **2007**, *19*, 1830.

(33) Loiseau, T.; Lecroq, L.; Volkringer, C.; Marrot, J.; Férey, G.; Haouas, M.; Taulelle, F.; Bourrelly, S.; Llewellyn, P. L.; Latroche, M. *Journal of the American Chemical Society* **2006**, *128*, 10223.

(34) Yazaydın, A. O. z. r.; Benin, A. I.; Faheem, S. A.; Jakubczak, P.; Low, J. J.; Willis, R. R.; Snurr, R. Q. *Chemistry of Materials* **2009**, *21*, 1425.

(35) Valenzano, L.; Civalleri, B.; Chavan, S.; Palomino, G. T.; Areán, C. O.; Bordiga, S. *The Journal of Physical Chemistry C* **2010**, *114*, 11185.

(36) Stavitski, E.; Pidko, E. A.; Couck, S.; Remy, T.; Hensen, E. J. M.; Weckhuysen, B. M.; Denayer, J.; Gascon, J.; Kapteijn, F. *Langmuir* **2011**, *27*, 3970.

(37) Farha, O. K.; Özgür Yazaydın, A.; Eryazici, I.; Malliakas, C. D.; Hauser, B. G.; Kanatzidis, M. G.; Nguyen, S. T.; Snurr, R. Q.; Hupp, J. T. *Nature Chemistry* **2010**, *2*, 944.

(38) Babarao, R.; Jiang, J. *Journal of the American Chemical Society* **2009**, *131*, 11417.

(39) Greathouse, J. A.; Allendorf, M. D. *Journal of the American Chemical Society* **2006**, *128*, 10678.

(40) Voet, D.; Voet, J. G.; Pratt, C. W. *Fundamentals of Biochemistry: Life at the Molecular Level*; 2nd ed.; John Wiley & Sons: Hoboken, 2006.

(41) Khalid, M.; Simard, P.; Hoarau, D.; Dragomir, A.; Leroux, J.-C. *Pharmaceutical Research* **2006**, *23*, 752.

(42) Bertrand, N.; Leroux, J.-C. *Journal of Controlled Release*.

(43) Horcajada, P.; Chalati, T.; Serre, C.; Gillet, B.; Sebrie, C.; Baati, T.; Eubank, J. F.; Heurtaux, D.; Clayette, P.; Kreuz, C.; Chang, J.-S.; Hwang, Y. K.; Marsaud, V.; Bories, P.-N.; Cynober, L.; Gil, S.; Ferey, G.; Couvreur, P.; Gref, R. *Nat Mater* **2010**, *9*, 172.

(44) Horcajada, P.; Serre, C.; Vallet-Regí, M.; Sebban, M.; Taulelle, F.; Férey, G. *Angewandte Chemie International Edition* **2006**, *45*, 5974.

(45) An, J.; Geib, S. J.; Rosi, N. L. *Journal of the American Chemical Society* **2009**, *131*, 8376.

(46) Jannasch, P. *Current Opinion in Colloid & Interface Science* **2003**, *8*, 96.

(47) Mauritz, K. A.; Moore, R. B. *Chemical Reviews* **2004**, *104*, 4535.

(48) Kreuer, K.-D.; Paddison, S. J.; Spohr, E.; Schuster, M. *Chemical Reviews* **2004**, *104*, 4637.

(49) Taylor, J. M.; Mah, R. K.; Moudrakovski, I. L.; Ratcliffe, C. I.; Vaidhyanathan, R.; Shimizu, G. K. H. *Journal of the American Chemical Society* **2010**, *132*, 14055.

(50) Ohkoshi, S.-i.; Nakagawa, K.; Tomono, K.; Imoto, K.; Tsunobuchi, Y.; Tokoro, H. *Journal of the American Chemical Society* **2010**, *132*, 6620.

(51) Yamada, T.; Sadakiyo, M.; Kitagawa, H. *Journal of the American Chemical Society* **2009**, *131*, 3144.

(52) Bureekaew, S.; Horike, S.; Higuchi, M.; Mizuno, M.; Kawamura, T.; Tanaka, D.; Yanai, N.; Kitagawa, S. *Nat Mater* **2009**, *8*, 831.

(53) Jeong, N. C.; Samanta, B.; Lee, C. Y.; Farha, O. K.; Hupp, J. T. *Journal of the American Chemical Society* **2011**, *134*, 51.

(54) Kobayashi, Y.; Jacobs, B.; Allendorf, M. D.; Long, J. R. *Chemistry of Materials* **2010**, *22*, 4120.

(55) Takaishi, S.; Hosoda, M.; Kajiwara, T.; Miyasaka, H.; Yamashita, M.; Nakanishi, Y.; Kitagawa, Y.; Yamaguchi, K.; Kobayashi, A.; Kitagawa, H. *Inorganic Chemistry* **2008**, *48*, 9048.

(56) Farrusseng, D.; Aguado, S.; Pinel, C. *Angewandte Chemie International Edition* **2009**, *48*, 7502.

(57) Thanasekaran, P.; Luo, T.-T.; Wu, J.-Y.; Lu, K.-L. *Dalton Transactions* **2012**, *41*, 5437.

(58) Silva, C. G.; Corma, A.; Garcia, H. *Journal of Materials Chemistry* **2010**, *20*, 3141.

(59) Glaser, T. *Angewandte Chemie International Edition* **2003**, *42*, 5668.

(60) Low, J. J.; Benin, A. I.; Jakubczak, P.; Abrahamian, J. F.; Faheem, S. A.; Willis, R. R. *Journal of the American Chemical Society* **2009**, *131*, 15834.

(61) Salles, F.; Bourrelly, S.; Jobic, H.; Devic, T.; Guillerm, V.; Llewellyn, P.; Serre, C.; Ferey, G. r.; Maurin, G. *The Journal of Physical Chemistry C* **2011**, *115*, 10764.

(62) Serre, C.; Millange, F.; Thouvenot, C.; Noguès, M.; Marsolier, G.; Louër, D.; Férey, G. *Journal of the American Chemical Society* **2002**, *124*, 13519.

(63) Uemura, K.; Yamasaki, Y.; Komagawa, Y.; Tanaka, K.; Kita, H. *Angewandte Chemie International Edition* **2007**, *46*, 6662.

(64) Dybtsev, D. N.; Chun, H.; Kim, K. *Angewandte Chemie International Edition* **2004**, *43*, 5033.

(65) Bourrelly, S.; Llewellyn, P. L.; Serre, C.; Millange, F.; Loiseau, T.; Férey, G. *Journal of the American Chemical Society* **2005**, *127*, 13519.

(66) Henke, S.; Florian Wieland, D. C.; Meilikhov, M.; Paulus, M.; Sternemann, C.; Yusenko, K.; Fischer, R. A. *CrystEngComm* **2011**, *13*, 6399.

(67) Salles, F.; Ghoufi, A.; Maurin, G.; Bell, R. G.; Mellot-Draznieks, C.; Férey, G. *Angewandte Chemie International Edition* **2008**, *47*, 8487.

(68) Grosch, J. S.; Paesani, F. *Journal of the American Chemical Society* **2012**, *134*, 4207.

(69) Coudert, F. o.-X.; Mellot-Draznieks, C.; Fuchs, A. H.; Boutin, A. *Journal of the American Chemical Society* **2009**, *131*, 3442.

(70) Dubbeldam, D.; Krishna, R.; Snurr, R. Q. *The Journal of Physical Chemistry C* **2009**, *113*, 19317.

(71) Triguero, C.; Coudert, F.-X.; Boutin, A.; Fuchs, A. H.; Neimark, A. V. *The Journal of Physical Chemistry Letters* **2011**, *2*, 2033.

(72) Jeffroy, M.; Fuchs, A. H.; Boutin, A. *Chemical Communications* **2008**, 3275.

(73) Yanai, N.; Uemura, T.; Inoue, M.; Matsuda, R.; Fukushima, T.; Tsujimoto, M.; Isoda, S.; Kitagawa, S. *Journal of the American Chemical Society* **2012**, *134*, 4501.

(74) Jensen, F. *Introduction to Computational Chemistry*; 2nd ed.; John Wiley & Sons: West Sussex, 2007.

(75) Cramer, C. J. *Essentials of Computational Chemistry: Theories and Models*; 2nd ed.; John Wiley & Sons: West Sussex, 2004.

(76) Møller, C.; Plesset, M. S. *Physical Review* **1934**, *46*, 618.

(77) Dunning, J. T. H. *The Journal of Chemical Physics* **1989**, *90*, 1007.

(78) Hohenberg, P.; Kohn, W. *Physical Review* **1964**, *136*, B864.

(79) Kohn, W.; Sham, L. J. *Physical Review* **1965**, *140*, A1133.

(80) Vosko, S. H.; Wilk, L.; Nusair, M. *Canadian Journal of Physics* **1980**, *58*, 1200.

(81) Perdew, J. P.; Wang, Y. *Physical Review B* **1992**, *45*, 13244.

(82) Becke, A. D. *Physical Review A* **1988**, *38*, 3098.

(83) Lee, C.; Yang, W.; Parr, R. G. *Physical Review B* **1988**, *37*, 785.

(84) Perdew, J. P.; Burke, K.; Ernzerhof, M. *Physical Review Letters* **1996**, *77*, 3865.

(85) Becke, A. D.; Roussel, M. R. *Physical Review A* **1989**, *39*, 3761.

(86) Becke, A. D. *The Journal of Chemical Physics* **1996**, *104*, 1040.

(87) Becke, A. D. *The Journal of Chemical Physics* **1993**, *98*, 5648.

(88) Zhao, Y.; Truhlar, D. *Theoretical Chemistry Accounts: Theory, Computation, and Modeling (Theoretica Chimica Acta)* **2008**, *120*, 215.

(89) Breneman, C. M.; Wiberg, K. B. *Journal of Computational Chemistry* **1990**, *11*, 361.

(90) Chirlian, L. E.; Francl, M. M. *Journal of Computational Chemistry* **1987**, *8*, 894.

(91) Parrinello, M.; Rahman, A. *The Journal of Chemical Physics* **1984**, *80*, 860.

(92) Feynman, R. P.; Hibbs, A. R. *Quantum Mechanics and Path Integrals*; McGraw-Hill: New York, 1965.

(93) Voth, G. A. In *Advances in Chemical Physics*; John Wiley & Sons, Inc.: 1996, p 135.

(94) Allinger, N. L.; Yuh, Y. H.; Lii, J. H. *Journal of the American Chemical Society* **1989**, *111*, 8551.

(95) Cornell, W. D.; Cieplak, P.; Bayly, C. I.; Gould, I. R.; Merz, K. M.; Ferguson, D. M.; Spellmeyer, D. C.; Fox, T.; Caldwell, J. W.; Kollman, P. A. *Journal of the American Chemical Society* **1995**, *117*, 5179.

(96) Sun, H. *The Journal of Physical Chemistry B* **1998**, *102*, 7338.

(97) Allured, V. S.; Kelly, C. M.; Landis, C. R. *Journal of the American Chemical Society* **1991**, *113*, 1.

(98) Jorgensen, W. L.; Maxwell, D. S.; Tirado-Rives, J. *Journal of the American Chemical Society* **1996**, *118*, 11225.

(99) Rappe, A. K.; Casewit, C. J.; Colwell, K. S.; Goddard, W. A.; Skiff, W. M. *Journal of the American Chemical Society* **1992**, *114*, 10024.

(100) Leach, A. R. *Molecular Modeling: Principles and Applications*; 2nd ed.; Pearson: Essex, 2001.

(101) Allinger, N. L.; Li, F.; Yan, L. *Journal of Computational Chemistry* **1990**, *11*, 848.

(102) Thole, B. T. *Chemical Physics* **1981**, *59*, 341.

(103) Applequist, J.; Carl, J. R.; Fung, K.-K. *Journal of the American Chemical Society* **1972**, *94*, 2952.

(104) Frenkel, D.; Smit, B. *Understanding Molecular Simulation: From Algorithms to Applications*; 2nd ed.; Elsevier: San Diego, 2002.

(105) Ryckaert, J.-P.; Ciccotti, G.; Berendsen, H. J. C. *Journal of Computational Physics* **1977**, *23*, 327.

(106) Hoover, W. G. *Physical Review A* **1985**, *31*, 1695.

(107) Parrinello, M.; Rahman, A. *Journal of Applied Physics* **1981**, *52*, 7182.

(108) Jorgensen, W. L.; Chandrasekhar, J.; Madura, J. D.; Impey, R. W.; Klein, M. L. *The Journal of Chemical Physics* **1983**, *79*, 926.

(109) Berendsen, H. J. C.; Postma, J. P. M.; van Gunsteren, W. F.; Hermans, J. In *Intermolecular Forces*; Pullman, B., Ed.; Reidel: Dordrecht, 1981, p 331.

(110) Abascal, J. L. F.; Vega, C. *The Journal of Chemical Physics* **2005**, *123*, 234505.

(111) Wu, Y.; Tepper, H. L.; Voth, G. A. *The Journal of Chemical Physics* **2006**, *124*, 024503.

(112) Park, K.; Lin, W.; Paesani, F. *The Journal of Physical Chemistry B* **2011**, *116*, 343.

(113) Moilanen, D. E.; Piletic, I. R.; Fayer, M. D. *The Journal of Physical Chemistry C* **2007**, *111*, 8884.

(114) Moilanen, D. E.; Fenn, E. E.; Wong, D.; Fayer, M. D. *Journal of the American Chemical Society* **2009**, *131*, 8318.

(115) Malikova, N.; Cadène, A.; Marry, V.; Dubois, E.; Turq, P. *The Journal of Physical Chemistry B* **2006**, *110*, 3206.

(116) Ball, P. *Chemical Reviews* **2007**, *108*, 74.

(117) Ricci, M. A.; Bruni, F.; Gallo, P.; Rovere, M.; Soper, A. K. *Journal of Physics: Condensed Matter* **2000**, *12*, A345.

(118) Rasaiah, J. C.; Garde, S.; Hummer, G. *Annual Review of Physical Chemistry* **2008**, *59*, 713.

(119) Hugo, K. C. *Journal of Physics: Condensed Matter* **2001**, *13*, R95.

(120) Köfinger, J.; Dellago, C. *Physical Review Letters* **2009**, *103*, 080601.

(121) Zhang, Y.; Faraone, A.; Kamitakahara, W. A.; Liu, K.-H.; Mou, C.-Y.; Leão, J. B.; Chang, S.; Chen, S.-H. *Proceedings of the National Academy of Sciences* **2011**, *108*, 12206.

(122) Reiter, G. F.; Kolesnikov, A. I.; Paddison, S. J.; Platzman, P. M.; Moravsky, A. P.; Adams, M. A.; Mayers, J. *Physical Review B* **2012**, *85*, 045403.

(123) Paesani, F.; Molecular Simulation: 2012, in press.

(124) Furukawa, H.; Ko, N.; Go, Y. B.; Aratani, N.; Choi, S. B.; Choi, E.; Yazaydin, A. Ö.; Snurr, R. Q.; O'Keeffe, M.; Kim, J.; Yaghi, O. M. *Science* **2010**, *329*, 424.

(125) Banerjee, R.; Phan, A.; Wang, B.; Knobler, C.; Furukawa, H.; O'Keeffe, M.; Yaghi, O. M. *Science* **2008**, *319*, 939.

(126) Wang, B.; Cote, A. P.; Furukawa, H.; O/'Keeffe, M.; Yaghi, O. M. *Nature* **2008**, *453*, 207.

(127) McDonald, T. M.; Lee, W. R.; Mason, J. A.; Wiers, B. M.; Hong, C. S.; Long, J. R. *Journal of the American Chemical Society* **2012**, *134*, 7056.

(128) Park, K. S.; Ni, Z.; Côté, A. P.; Choi, J. Y.; Huang, R.; Uribe-Romo, F. J.; Chae, H. K.; O'Keeffe, M.; Yaghi, O. M. *Proceedings of the National Academy of Sciences* **2006**, *103*, 10186.

(129) Demessence, A.; D'Alessandro, D. M.; Foo, M. L.; Long, J. R. *Journal of the American Chemical Society* **2009**, *131*, 8784.

(130) Kondo, A.; Daimaru, T.; Noguchi, H.; Ohba, T.; Kaneko, K.; Kanoh, H. *Journal of Colloid and Interface Science* **2007**, *314*, 422.

(131) Küsgens, P.; Rose, M.; Senkovska, I.; Fröde, H.; Henschel, A.; Siegle, S.; Kaskel, S. *Microporous and Mesoporous Materials* **2009**, *120*, 325.

(132) Nguyen, J. G.; Cohen, S. M. *Journal of the American Chemical Society* **2010**, *132*, 4560.

(133) Wu, T.; Shen, L.; Luebbers, M.; Hu, C.; Chen, Q.; Ni, Z.; Masel, R. I. *Chemical Communications* **2010**, *46*, 6120.

(134) Ma, D.; Li, Y.; Li, Z. *Chemical Communications* **2011**, *47*, 7377.

(135) Han, S. S.; Choi, S.-H.; van Duin, A. C. T. *Chemical Communications* **2010**, *46*, 5713.

(136) Chen, Z. X.; Xiang, S. C.; Zhao, D. Y.; Chen, B. L. *Crystal Growth & Design* **2009**, *9*, 5293.

(137) Belof, J. L.; Stern, A. C.; Eddaoudi, M.; Space, B. *Journal of the American Chemical Society* **2007**, *129*, 15202.

(138) Belof, J. L.; Stern, A. C.; Space, B. *The Journal of Physical Chemistry C* **2009**, *113*, 9316.

(139) Stern, A. C.; Belof, J. L.; Eddaoudi, M.; Space, B. *The Journal of Chemical Physics* **2012**, *136*, 034705.

(140) McDaniel, J. G.; Yu, K.; Schmidt, J. R. *The Journal of Physical Chemistry C* **2011**, *116*, 1892.

(141) Warshel, A.; Kato, M.; Pisliakov, A. V. *Journal of Chemical Theory and Computation* **2007**, *3*, 2034.

(142) Millange, F.; Serre, C.; Ferey, G. *Chemical Communications* **2002**, 822.

(143) van Duijnen, P. T.; Swart, M. *The Journal of Physical Chemistry A* **1998**, *102*, 2399.

(144) Shannon, R. D. *Journal of Applied Physics* **1993**, *73*, 348.

(145) Fanourgakis, G. S.; Xantheas, S. S. *The Journal of Chemical Physics* **2008**, *128*, 074506.

(146) Todorov, I. T.; Smith, W.; Trachenko, K.; Dove, M. T. *Journal of Materials Chemistry* **2006**, *16*, 1911.

(147) Smith, W.; Forester, T. R. *Journal of Molecular Graphics* **1996**, *14*, 136.

(148) Frisch, M. J.; Trucks, G. W.; Schlegel, H. B.; Scuseria, G. E.; Robb, M. A.; Cheeseman, J. R.; Scalmani, G.; Barone, V.; Mennucci, B.; Petersson, G. A.; Nakatsuji, H.; Caricato, M.; Li, X.; Hratchian, H. P.; Izmaylov, A. F.; Bloino, J.; Zheng, G.; Sonnenberg, J. L.; Hada, M.; Ehara, M.; Toyota, K.; Fukuda, R.; Hasegawa, J.; Ishida, M.; Nakajima, T.; Honda, Y.; Kitao, O.; Nakai, H.; Vreven, T.; Montgomery, J., J. A.; Peralta, J. E.; Ogliaro, F.; Bearpark, M.; Heyd, J. J.; Brothers, E.; Kudin, K. N.; Staroverov, V. N.; Kobayashi, R.; Normand, J.; Raghavachari, K.; Rendell, A.; Burant, J. C.; Iyengar, S. S.; Tomasi, J.; Cossi, M.; Rega, N.; Millam, J. M.; Klene, M.; Knox, J. E.; Cross, J. B.; Bakken, V.; Adamo, C.; Jaramillo, J.; Gomperts, R.; Stratmann, R. E.; Yazyev, O.; Austin, A. J.; Cammi, R.; Pomelli, C.; Ochterski, J. W.; Martin, R. L.; Morokuma, K.; Zakrzewski, V. G.; Voth, G. A.; Salvador, P.; Dannenberg, J. J.; Dapprich, S.; Daniels, A. D.; Farkas, Ã.; Foresman, J. B.; Ortiz, J. V.; Cioslowski, J.; Fox, D. J.; Gaussian, Inc: Wallingford, 2009.

(149) Hay, P. J.; Wadt, W. R. *The Journal of Chemical Physics* **1985**, *82*, 270.

(150) Salles, F., Private communication.

(151) Bakker, H. J.; Skinner, J. L. *Chemical Reviews* **2009**, *110*, 1498.

(152) Paesani, F. *The Journal of Physical Chemistry A* **2011**, *115*, 6861.

(153) Paesani, F. *Physical Chemistry Chemical Physics* **2011**, *13*, 19865.

(154) Kim, M.; Boissonnault, J. A.; Dau, P. V.; Cohen, S. M. *Angewandte Chemie International Edition* **2011**, *50*, 12193.

(155) Peterson, K. A.; Puzzarini, C. *Theoretical Chemistry Accounts: Theory, Computation, and Modeling (Theoretica Chimica Acta)* **2005**, *114*, 283.

(156) Case, D. A.; Darden, T. A.; Cheatham, T. E.; Simmerling, C. L.; Wang, J.; Duke, R. E.; Luo, R.; Walker, R. C.; Zhang, W.; Merz, K. M.; Roberts, B.; Wang, B.; Hayik, S.; Roitberg, A.; Seabra, G.; Kolossváry, I.; Wong, K. F.; Paesani, F.; Vanicek, J.; Liu, J.; Wu, X.; Brozell, S. R.; Steinbrecher, T.; Gohlke, H.; Cai, Q.; Ye, X.; Wang, J.; Hsieh, M.-J.; Cui, G.; Roe, D. R.; Mathews, D. H.; Seetin, M. G.; Sagui, C.; Babin, V.; Luchko, T.; Gusarov, S.; Kovalenko, A.; Kollman, P. A.; University of California, San Francisco: 2010.

(157) Evans, M. W. *Advances in Molecular Relaxation and Interaction Processes* **1982**, *24*, 123.

(158) Lee, J. S. *Bulletin of the Korean Chemical Society* **2011**, *32*, 4199.

(159) Chui, S. S. Y.; Lo, S. M. F.; Charmant, J. P. H.; Orpen, A. G.; Williams, I. D. *Science* **1999**, *283*, 1148.

(160) Voth, G. A. *Accounts of Chemical Research* **2006**, *39*, 143.

(161) Chen, H.; Yan, T.; Voth, G. A. *The Journal of Physical Chemistry A* **2009**, *113*, 4507.

(162) Allen, F. *Acta Crystallographica Section B* **2002**, *58*, 380.

(163) Tafipolsky, M.; Amirjalayer, S.; Schmid, R. *The Journal of Physical Chemistry C* **2010**, *114*, 14402.

(164) Tafipolsky, M.; Amirjalayer, S.; Schmid, R. *Journal of Computational Chemistry* **2007**, *28*, 1169.

(165) Tafipolsky, M.; Schmid, R. *The Journal of Physical Chemistry B* **2009**, *113*, 1341.

(166) Smondyrev, A. M.; Voth, G. A. *Biophysical Journal* **2002**, *83*, 1987.

(167) Ponder, W.; Ren, P.; Pappu, R. V.; Hart, R. K.; Hodgson, M. E.; Cistola, D. P.; Kundrot, C. E.; Richards, F. M.; Washington University School of Medicine: 2004.

(168) Wu, Y.; Kobayashi, A.; Halder, G. J.; Peterson, V. K.; Chapman, K. W.; Lock, N.; Southon, P. D.; Kepert, C. J. *Angewandte Chemie International Edition* **2008**, *47*, 8929.